



A Review on Gallium Oxide Materials from Solution Processes

Jung-Lung Chiang ^{1,†}, Bharath Kumar Yadlapalli ^{2,†} , Mu-I Chen ² and Dong-Sing Wu ^{2,3,4,*}

- ¹ Ph.D. Program, Prospective Technology of Electrical Engineering and Computer Science, National Chin-Yi University of Technology, Taichung 41170, Taiwan
- ² Department of Materials Science and Engineering, National Chung Hsing University, Taichung 40227, Taiwan
- ³ Department of Applied Materials and Optoelectronic Engineering, National Chi Nan University, Nantou 54561, Taiwan
- ⁴ Innovation and Development Center of Sustainable Agriculture, National Chung Hsing University, Taichung 40227, Taiwan
- * Correspondence: dsw@ncnu.edu.tw or dsw@dragon.nchu.edu.tw; Tel.: +886-49-2910960 (ext. 2000); Fax: +886-49-2912569
- † These authors contributed equally to this work.

Abstract: Gallium oxide (Ga_2O_3) materials can be fabricated via various methods or processes. It is often mentioned that it possesses different polymorphs (α -, β -, γ -, δ - and ϵ - Ga_2O_3) and excellent physical and chemical properties. The basic properties, crystalline structure, band gap, density of states, and other properties of Ga_2O_3 will be discussed in this article. This article extensively discusses synthesis of pure Ga_2O_3 , co-doped Ga_2O_3 and Ga_2O_3 -metal oxide composite and Ga_2O_3 /metal oxide heterostructure nanomaterials via solution-based methods mainly sol-gel, hydrothermal, chemical bath methods, solvothermal, forced hydrolysis, reflux condensation, and electrochemical deposition methods. The influence of the type of precursor solution and the synthesis conditions on the morphology, size, and properties of final products is thoroughly described. Furthermore, the applications of Ga_2O_3 will be introduced and discussed from these solution processes, such as deep ultraviolet photodetector, gas sensors, pH sensors, photocatalytic and photodegradation, and other applications. In addition, research progress and future outlook are identified.



Citation: Chiang, J.-L.; Yadlapalli, B.K.; Chen, M.-I.; Wu, D.-S. A Review on Gallium Oxide Materials from Solution Processes. *Nanomaterials* **2022**, *12*, 3601. <https://doi.org/10.3390/nano12203601>

Academic Editor: Wan Sik Hwang

Received: 9 September 2022

Accepted: 9 October 2022

Published: 14 October 2022

Publisher's Note: MDPI stays neutral with regard to jurisdictional claims in published maps and institutional affiliations.



Copyright: © 2022 by the authors. Licensee MDPI, Basel, Switzerland. This article is an open access article distributed under the terms and conditions of the Creative Commons Attribution (CC BY) license (<https://creativecommons.org/licenses/by/4.0/>).

Keywords: gallium oxide; sol-gel; hydrothermal; chemical bath deposition; solvothermal; forced hydrolysis; reflux condensation; electrochemical deposition; photodetector; sensor

1. Introduction

Gallium oxide (Ga_2O_3) has been a well-known old material for decades. The element gallium and its compounds were first discovered by a French man, P. E. Lecoq de Boisbaudran [1]. Research on Ga_2O_3 began from the investigation on the phase equilibria in the system Al_2O_3 - Ga_2O_3 - H_2O by R. Roy et al. [2]. In 1952, he further demonstrated the existence of five types of Ga_2O_3 polymorphs and their stability relations [3]. By observing its optical absorption and photoconductivity, the band gap of bulk single crystals of Ga_2O_3 was known as 4.7 eV in 1965 [4]. Early research about Ga_2O_3 focused on its basic properties, such as crystal structures, band gap, density of states of electrons, and so on. This part will be described in detail in the next chapter. The crystal quality of Ga_2O_3 materials in most scientific reports published in the range of 1960s~1980s was poor or even in amorphous forms [5]. That is why Ga_2O_3 had been ignored by most semiconductor researchers and engineers, resulting in its development lagging behind SiC and GaN.

In the 1990s, various methods for growing high-quality and large-sized Ga_2O_3 bulk single crystals were developed [5]. In the same period, high quality epitaxial thin films of Ga_2O_3 had also been successfully grown as essential parts of more complex devices [6]. Apart from bulk crystals and epitaxial thin films, various forms of Ga_2O_3 nanomaterials have made considerable progress in growth methods, basic properties, and device applications due to the rapid development in science and technology [7]. Because of nanoscale

size in at least one dimension, nanomaterials have a high aspect ratio, which leads to high activity and some unique quantum-dimensional effects [8]. UV photodetectors [9,10], photocatalysis [11], flat panel display [12], UV filter [13], MOS capacitor [14], MOS structure [15] and optoelectronic devices [16,17] are some of the applications of Ga₂O₃.

In principle, the vapor deposition process, either physical vapor deposition (PVD) or chemical vapor deposition (CVD), is the mainstream for the fabrication of gallium oxide thin films and nanomaterials. Generally speaking, thin films made by vapor deposition have a higher uniformity and better quality. The thermal evaporation method, a kind of PVD, followed by CVD, are primarily used in the fabrication of β-Ga₂O₃ nanomaterials [6]. However, such processes should be carried out using vacuum equipment, which has higher maintenance costs. Additionally, excessively high temperature, complexity in process, and a limited deposition area are also problems in the vacuum process, especially the potential need for expensive catalysts in the vacuum process of Ga₂O₃ nanomaterials [8].

In order to reduce complexity and energy consumption during the manufacturing process, a number of wet chemical processes, also called wet chemistry approaches, which include hydrothermal, sol-gel, chemical bath deposition (CBD), and so on, are promising to synthesize Ga₂O₃ thin films and nanomaterials [8]. These methods can achieve large area deposition and high yield through a simple experimental process at a low temperature in an ambient atmosphere [18]. By controlling the amounts of individual precursors, it is easy to tune the final material compositions. Furthermore, these wet chemical solution processes are effective methods to prepare various kinds of nano-powders. That is why solution process has gained more acceptance in recent years [19].

Typically, Ga₂O₃ nanomaterials could be obtained by calcining gallium oxide hydroxide (GaOOH), which is a common intermediate product of wet chemistry approaches of gallium oxide and could be shaped with a variety of morphologies, including rod-like, spindle-like, and scroll-like cylindrical structures [20,21]. In comparison to Ga₂O₃, many kinds of oxides, such as ZnO, IGZO, and In₂O₃, have been widely manufactured by wet chemical solution processes [22]; the number of studies on the wet chemical growth of Ga₂O₃ is growing in recent years, as shown in Figure 1.

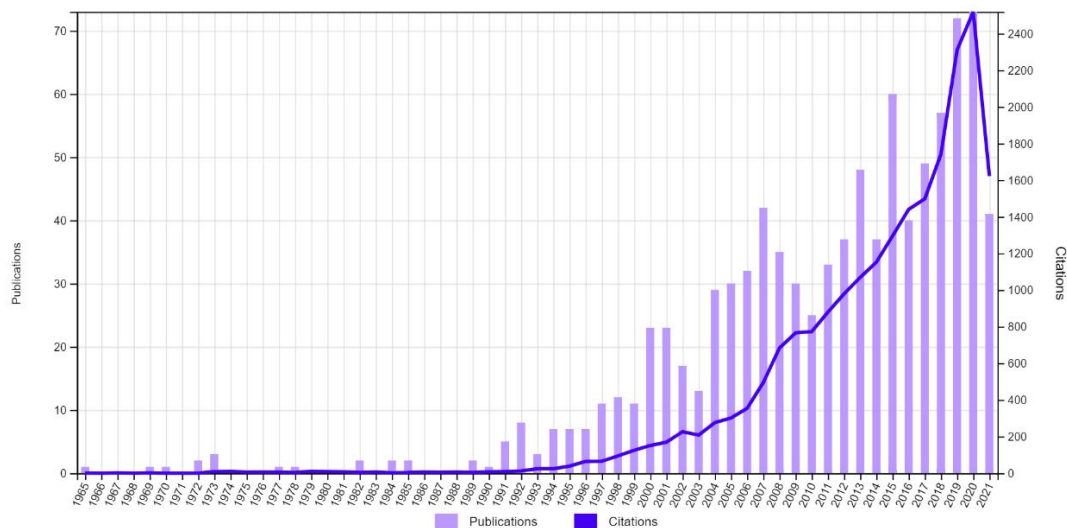


Figure 1. Number of publications and citations on gallium oxide from solution process since 1965. A total of 936 papers have been published and the number of citations is 15821 in the last 55 years (Data: Web of Science).

Therefore, this review will focus on Ga₂O₃ fabricated by wet chemical solution processes that include mainly three methods: sol-gel, hydrothermal, and chemical bath deposition. The basic elaboration of the three methods will be presented in the third chapter. The fourth chapter in the main topic of the review is: Ga₂O₃ thin films and nanomaterials

synthesized by the three main kinds and four other kinds of wet chemistry approaches. The fifth chapter demonstrates the applications of Ga₂O₃ synthesized through wet chemical solution processes, such as deep ultraviolet photodetector, gas sensors, pH sensors, photocatalytic and photodegradation, and so on.

There have been numerous reviews on the synthesis of Ga₂O₃ in recent years [8,23,24]. Despite mentioning one or two solution-based methods, a thorough discussion on the solution-based synthesis of Ga₂O₃ was still required to understand its mechanism of synthesis and changes in properties. This review serves as a comprehensive text for a solution-based Ga₂O₃ synthesis.

2. Basic Properties of Ga₂O₃

Before introducing growth methods and applications of Ga₂O₃, some fundamental properties of different Ga₂O₃ phases have to be discussed, as these are key in understanding Ga₂O₃. Several research papers about this topic have been published through experimental or theoretical investigations [25–32]. The basic properties of Ga₂O₃, such as crystalline structures, band structures, and density of states of electrons will be discussed as follows.

2.1. Crystalline Structure of Ga₂O₃

In general, there are five different polymorphs labelled as α , β , γ , δ , and ϵ for Ga₂O₃ single crystal, first reported by Roy et al. in 1952 [3]. Table 1 contains a list of their lattice parameters and space groups. Among them, only β -Ga₂O₃ can be formed as bulk crystals directly from the melt, while the other four metastable crystalline phases can only be obtained as thin films [6]. The scientific reports focused on the material properties and crystal growth of β -Ga₂O₃ much more than those on the other four types because β -Ga₂O₃ is the most stable phase and is easily fabricated [33,34].

Table 1. Crystal structures and lattice parameters of different Ga₂O₃ polymorphs.

Polymorph Type	Crystal Structure	Space Group	Lattice Parameters	Ref.
α	Hexagonal or rhombohedral	R-3c	$a = b = 4.98 \text{ \AA}$, $c = 13.43 \text{ \AA}$, $\alpha = \beta = 90^\circ$, $\gamma = 120^\circ$	[25]
β	Monoclinic	C2/m	$a = 12.23 \text{ \AA}$, $b = 3.04 \text{ \AA}$, $c = 5.80 \text{ \AA}$, $\alpha = \gamma = 90^\circ$, $\beta = 103.7^\circ$	[35]
γ	Cubic	Fd-3m	$a = b = c = 8.24 \text{ \AA}$, $\alpha = \beta = \gamma = 90^\circ$	[36]
δ	Cubic	Ia3	$a = b = c = 9.402 \text{ \AA}$, $\alpha = \beta = \gamma = 90^\circ$	[37]
ϵ	Hexagonal	P6 ₃ mc	$a = b = 2.90 \text{ \AA}$, $c = 9.26 \text{ \AA}$, $\alpha = \beta = 90^\circ$, $\gamma = 120^\circ$	[32]

For the large-scale synthesis of crystalline Ga₂O₃ by wet chemical methods, gallium oxyhydroxide (α -GaOOH) is a common precursor, from which different gallium oxide phases (α , β , γ , δ , and ϵ) could be obtained through heat treatment under certain temperatures to dehydrate α -GaOOH [38]. Furthermore, various morphologies of Ga₂O₃ nanomaterials can also be obtained indirectly from different morphologies of α -GaOOH precursors [39] because in most cases α -GaOOH nanostructures can transform isomorphously to Ga₂O₃ under heat treatment [38]. Therefore, synthesis of Ga₂O₃ nanomaterials through thermal treatment of α -GaOOH has become an easy and convenient method [39]. In this section, the crystalline structure and morphology of α -GaOOH will be demonstrated first, followed by different polymorphs of Ga₂O₃.

α -GaOOH has an orthorhombic structure (space group: *Pbmm*, lattice parameters: $a = 4.5545 \text{ \AA}$, $b = 9.8007 \text{ \AA}$, and $c = 2.9738 \text{ \AA}$, as shown in Figure 2a), along the *c*-axis of which α -GaOOH crystals prefer to grow in this direction [40] by continuously adsorbing

OH^- anions in the solution on the specific crystal plane (001) to facilitate nucleation and to grow into rod-like nanomaterials [8]. In addition, these rod-like GaOOH crystals usually have a prismatic shape with quadrilateral or rhombic cross-sections, which results from the outside embodiment of the stacked unit cells of the orthorhombic structure [41]. In principle, gallium(III) hydroxide $\text{Ga}(\text{OH})_3$ is the first precursor in the hydrolysis process before it is dehydrated to gallium oxide hydroxide at $100\text{ }^\circ\text{C}$ [42].

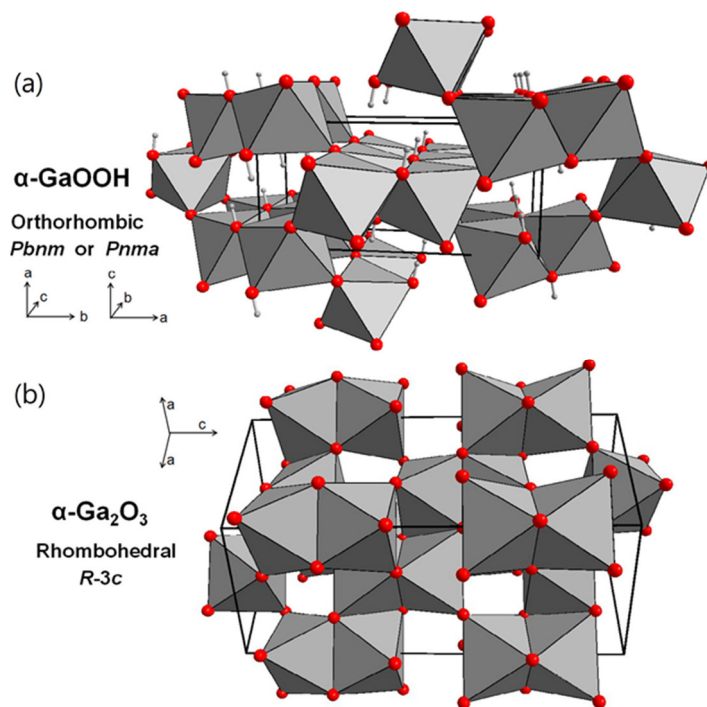


Figure 2. Crystal structures of (a) $\alpha\text{-GaOOH}$ and (b) $\alpha\text{-Ga}_2\text{O}_3$ phases represented by the cation polyhedra. The space group, crystallographic axes, and unit cell are designated. Reprinted figure with permission from [43]; copyright (2015) by Elsevier.

In principle, a crystal face with less closely packed atoms, which means the higher density of the unsaturated bonds, has more opportunity to absorb anions [44]. Based on the crystalline structure of $\alpha\text{-GaOOH}$, the (001) crystal surface has the least closely packed atoms, compared with the (010) and (100), and thus the most likely to absorb OH^- anions, leading to preferred growth at a higher rate along the [001] direction on the $\alpha\text{-GaOOH}$ amorphous particles under acidic [8] or neutral conditions [38]. Before hydrothermal treatment, spindle-shaped particles of $\alpha\text{-GaOOH}$ are the first resultant for fresh precipitate in an acidic and low-temperature environment [38,43]. The needle-like ends of the spindle-like particles imply faster growth in the [001] direction than the [010] and [100] directions [41]. However, when more OH^- anions exist in the solution, or the pH value increases, the (100) and (010) crystal surfaces have more opportunity to absorb OH^- anions such as the (001) crystal surface, resulting in isotropic growth to form ellipsoid-like particles composed of well-aligned nanoplatelets [41], nanorod arrays [45], or overlapping rhombi [43]. The major axes of these ellipsoid-shaped particles are along the [001] direction due to faster growth along this direction.

$\alpha\text{-GaOOH}$ can be easily transformed to $\alpha\text{-Ga}_2\text{O}_3$ with morphology preserved by heating $\alpha\text{-GaOOH}$ in air between $450\text{ }^\circ\text{C}$ and $550\text{ }^\circ\text{C}$ [3] because the oxygen anions of the two crystals are both based on the hexagonal close packing (hcp) with preserved stacking sequence of layers in the direction of [100] for $\alpha\text{-GaOOH}$ (Figure 2a) and [001] for $\alpha\text{-Ga}_2\text{O}_3$ (Figure 2b). Additionally, the growth direction changes from the [001] direction of $\alpha\text{-GaOOH}$ nanorods to the [010] direction of $\alpha\text{-Ga}_2\text{O}_3$ nanorods during the dihydroxylation process [43]. $\alpha\text{-Ga}_2\text{O}_3$ has a hexagonal (or rhombohedral [46]) crystal structure in the space

group of $R-3c$, which is commonly called the corundum structure. Gallium ions occupy two-thirds of the octahedral sites in the corundum crystal structure. That is why the Ga^{3+} ions are much closer together than they are in the monoclinic β phase [35], which will be mentioned in the next paragraph. There are 6 Ga_2O_3 formula units in every crystallographic cell with lattice parameters $a = b = 4.98 \text{ \AA}$, $c = 13.43 \text{ \AA}$, $\alpha = \beta = 90^\circ$, and $\gamma = 120^\circ$ [25].

When α -GaOOH nanorods are heated to 900°C , the cross sections change from the quadrilateral shape to diamond-like patterns, which is caused by the orthorhombic phase of α -GaOOH changing to the monoclinic phase of β - Ga_2O_3 [45]. Other morphologies of α -GaOOH can also be retained after this high-temperature calcination to form different morphologies of β - Ga_2O_3 nanomaterials except for the spindle-shaped α -GaOOH [43]. Furthermore, the monoclinic phase β - Ga_2O_3 has the best thermal stability up to 1800°C [7], while the other four metastable polymorphs tend to transform back to β - Ga_2O_3 at high temperatures [47], as shown in Figure 3.

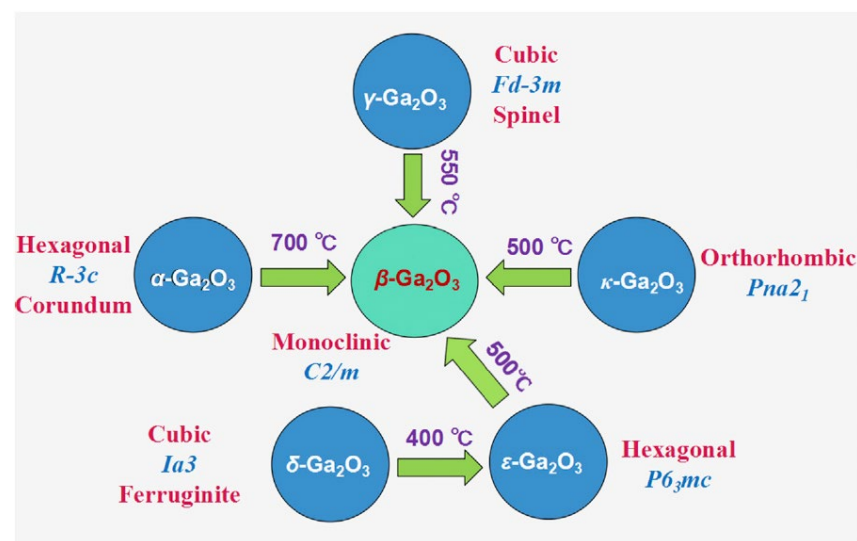


Figure 3. Interconversion relation of Ga_2O_3 polymorphs. Reprinted figure with permission from [48]; copyright (2019) by Elsevier.

β - Ga_2O_3 has a monoclinic crystal structure (space group: $C2/m$, lattice parameters: $a = 12.23 \text{ \AA}$, $b = 3.04 \text{ \AA}$, $c = 5.80 \text{ \AA}$ and a monoclinic angle: $\beta = 103.7^\circ$ [35]). There are four Ga_2O_3 formula units in every crystallographic cell, as shown in Figure 4, with two inequivalent Ga atoms and three inequivalent O atoms in one Ga_2O_3 formula unit. Tetrahedrally and octahedrally coordinated gallium atoms are designated as Ga1 and Ga2, respectively. The oxygen atoms are organized in a close-packed “distorted cubic” pattern [48]. O1 (red) stands for the oxygen atoms that share bonds with two Ga2 and one Ga1, while O3 (maroon) has two bonds with Ga1 and one bond with Ga2. O2 (pink) are primarily coupled to Ga2 by 3 bonds and connected to Ga1 with only one bond [49], as shown in Figure 4. O1 and O2 are coordinated threefold, while O3 are coordinated fourfold [6].

As α - Ga_2O_3 is obtained by calcining α -GaOOH, γ - Ga_2O_3 can be obtained by calcining $\text{Ga}(\text{OH})_3$ gel, which is the fresh precipitate before it rapidly goes through oxolation and condensation to α -GaOOH [50]. Similar to γ and η - Al_2O_3 , γ - Ga_2O_3 possesses a faulty cubic spinel-type structure (AB_2O_4 -type) [51], as shown in Figure 5a. It belongs to the space group of $Fd-3m$ with lattice parameters $a = b = c = 8.24 \text{ \AA}$ and $\alpha = \beta = \gamma = 90^\circ$ [36]. First principle calculations were made by expanding the primitive fcc unit cell along the c -axis by three times [37]. For such, the unit cell of the normal spinel structure contains 6 tetrahedrally coordinated cations, 12 octahedrally coordinated cations, and 24 oxygen ions. Among the 18 cations, 2 sites were chosen to be vacant. After considering the symmetry, 14 inequivalent configurations were found [37]. Because some of the Ga ions are located

on the tetrahedral sites in γ -Ga₂O₃, there is particular interest in this phase of Ga₂O₃ for possible applications in heterogeneous catalysis [52].

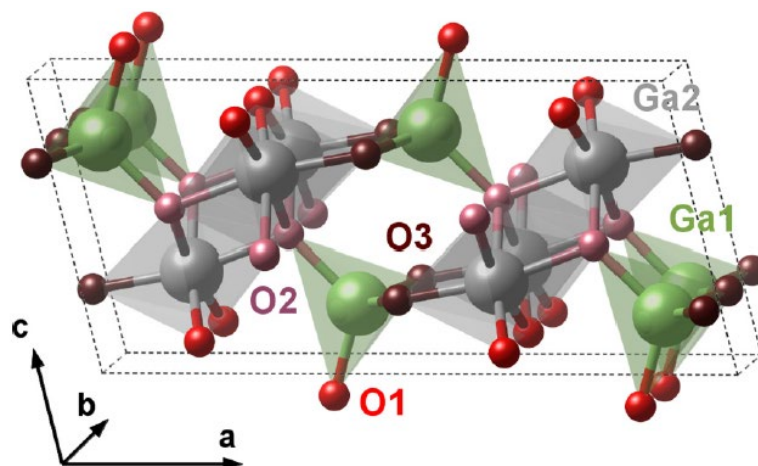


Figure 4. Unit cell of β -Ga₂O₃. Tetrahedrally coordinated Ga1 are green while octahedrally coordinated Ga2 are gray. Threefold O1 and O2 are indicated in red and pink, respectively, while fourfold O3 are indicated in maroon. Reprinted figure with permission from [49]; copyright (2016) by the American Physical Society.

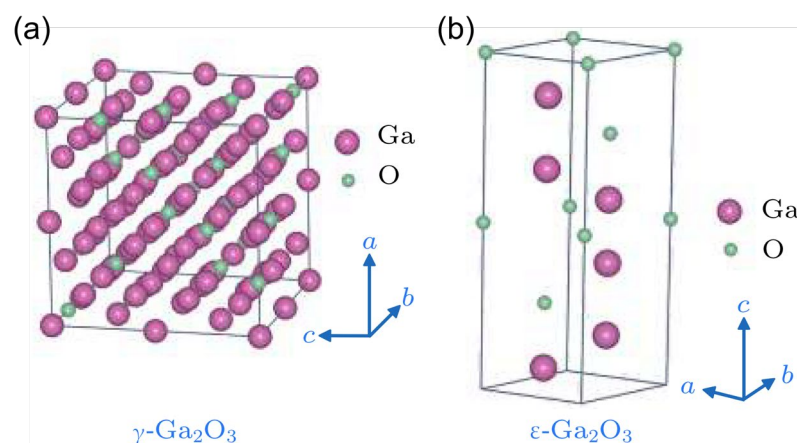


Figure 5. Crystal structures of polymorphs of (a) γ -Ga₂O₃ and (b) ϵ -Ga₂O₃. Reprinted figure with permission from [48]; copyright (2019) by Elsevier.

The last two polymorphs, named δ -Ga₂O₃ and ϵ -Ga₂O₃, were first discovered by Roy et al. [3] in 1952. The white powder of δ -Ga₂O₃ can be prepared by annealing gallium nitrate in the air at 200 °C for 18 h. Further heating the white powder at 500 °C for 6 h, the δ -Ga₂O₃ transforms to ϵ -Ga₂O₃ [53]. δ -Ga₂O₃ is a body-centered cubic crystal that belongs to the space group of $Ia\bar{3}$ with a unit edge length of $a = 9.402 \text{ \AA}$ [37]. δ -Ga₂O₃ has a bixbyite structure analogous to that of In₂O₃, Mn₂O₃, and Ti₂O₃ [32,37]. However, thin films of δ -Ga₂O₃ have not yet been obtained. As for ϵ -Ga₂O₃, it has a hexagonal crystal structure with lattice parameters $a = b = 2.90 \text{ \AA}$, $c = 9.26 \text{ \AA}$, $\alpha = \beta = 90^\circ$, and $\gamma = 120^\circ$ [32], which is similar to κ -Al₂O₃ [54–57] in the space group of $P6_3mc$, as shown in Figure 5b. This phase is next in stability among all Ga₂O₃ polymorphs to β -Ga₂O₃ [58–61]. Furthermore, density functional theory (DFT) calculation and recent experimental results indicate that ϵ -Ga₂O₃ is also an orthorhombic crystal belonging to the space group of $Pna2_1$ [37,54,62], which is an ordered subgroup of the hexagonal $P6_3mc$ [54,63].

2.2. Band Gap and Density of States of Electrons for Ga_2O_3

The fundamental electrical and optical characteristics of a material are defined by its electronic band structure. With this knowledge, we can know for what proper devices the material could be designed with desired functionalities [6]. Among all the polymorphs of Ga_2O_3 , $\beta\text{-Ga}_2\text{O}_3$ is the most representative of the polymorphs of Ga_2O_3 . Due to the difficulty in obtaining pure crystalline phases of $\beta\text{-Ga}_2\text{O}_3$, much knowledge about this topic comes from theoretical approaches [64–66]. Up to now, numerous first-principle computations employing standard density functional theory (DFT) have been used to study the basic electronic structure of $\beta\text{-Ga}_2\text{O}_3$ [27,64,67–71]. However, the standard DFT is not directly based on the excited states of electrons [68], causing an underestimated band gap. The hybrid functional [28,72–75] and GGA + U [76–78] approaches used in DFT were proven to provide more accurate results for the experimental band gaps of $\beta\text{-Ga}_2\text{O}_3$.

The full-energy band structure along with the corresponding density of states (DOS) of $\beta\text{-Ga}_2\text{O}_3$ are shown in Figure 6 as calculated by J. Furthmüller and F. Bechstedt [75]. From Figure 6, we can easily see that the densities of states (DOS) exhibit a direct reflection of the band structure. The maximum of the valence band (above -7.5 eV) is defined as zero energy level. The conduction band (above the zero-energy level) is mainly formed by Ga 4s orbitals. It can be easily seen from Figure 6 that the conduction band minimum (CBM) is located at the Γ point independent of the different polymorph of Ga_2O_3 [75]. On the contrary, the valence band is mainly formed by O 2p orbitals and is almost flat near 0 eV. Therefore, the precise location of the valence band maximum (VBM) is determined by the atomic configurations or the polymorphs of Ga_2O_3 [75].

For the DOS of the monoclinic polymorph ($\beta\text{-Ga}_2\text{O}_3$) from Figure 6, there also exists hybridization between Ga 4s and O 2p states in the lower region of the valence band. Furthermore, some Ga 4p states are located in the middle of the valence band of which some Ga 3d states are found near the top. The exact arrangement of the Ga and O atoms has a small impact on the energy distribution of the empty and occupied electronic states due to the strong ionic Ga-O bonding. That is why DOS diagrams of all different Ga_2O_3 polymorphs are very similar [75]. In addition to the valence band, there are two groups of core-level bands: bands mainly composed of O 2s orbitals in the energy region from -20.3 eV to -18.5 eV and bands mainly formed by Ga 3d orbitals in the energy region from -16 eV to -14.2 eV [73].

For $\beta\text{-Ga}_2\text{O}_3$, the valence band maximum (VBM) seems to be nearly degenerate at the Γ and M points. The energy at Γ point is 0.04 eV lower than that at M point. In this case, there is an indirect M- Γ band gap of 4.83 eV, slightly smaller than the direct band gap of 4.87 eV at Γ calculated by J. B. Varley et al. [74]. This result is close to the experimentally observed sharp absorption edge at ~ 4.9 eV [79]. Because of momentum conservation for the transition at Γ point, the transition at Γ - Γ is more probable than that at M- Γ [6]. The weakness of the indirect transition and the slight energy different between the indirect and direct band gaps make $\beta\text{-Ga}_2\text{O}_3$ a direct-band gap semiconductor [18]. However, the band gap for the rhombohedral corundum phase is obviously indirect and is roughly 0.25 eV less than the direct gap at Γ . Additionally, the cubic bixbyite structure has an indirect band gap which is approximately 0.1 eV lower than the direct gap at Γ [75].

Unlike the conduction band with the effective electron mass in the range of $0.24m_e$ – $0.34m_e$ [28,64,74] (where m_e is the free electron mass), the top of the valence band is almost flat, causing a very high effective hole mass (approximately $40 m_e$ along the Γ -Z direction [74]), or a very low effective hole mobility for $\beta\text{-Ga}_2\text{O}_3$. Therefore, it is impractical for $\beta\text{-Ga}_2\text{O}_3$ to be fabricated as a p-type semiconductor [6]. In fact, the holes cannot move freely because they tend to produce localized polarons that are confined by local lattice distortions [72,80,81].

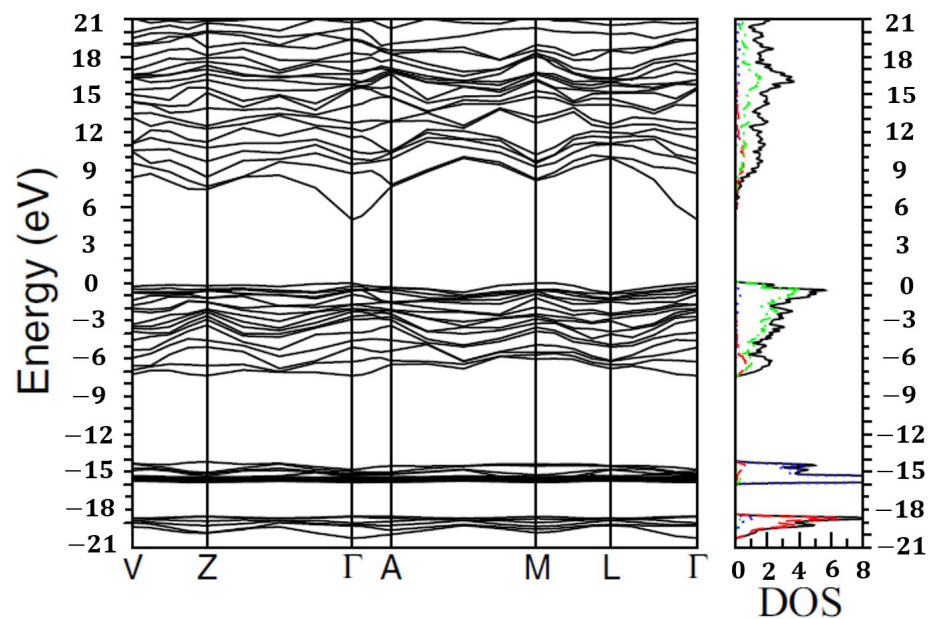


Figure 6. Quasiparticle band structures at HSE+G₀W₀ level of the β -Ga₂O₃ in the full energy range. In addition, the corresponding total (black full line), as well as the s- (red dashed line), p- (green dotted-dashed line), and d-projected (blue dotted line) density of states (DOS) is displayed. The valence band maximum (VBM) is defined as the zero energy. Figure reprinted with permission from [75]; copyright (2016) by the American Physical Society.

2.3. Other Properties

β -Ga₂O₃ has a wide band gap (4.8~4.9 eV) compared to SiC (3.3 eV) and GaN (3.4 eV) [82], which is intrinsically suitable for fabricating solar-blind deep ultraviolet (DUV) photodetectors [34,83–85]. Owing to its wide band gap, pure β -Ga₂O₃ crystals are colorless and extremely transparent up to UV-C range of the light spectrum. Typically, the absorbance spectra depict a steep cutoff absorption edge at approximately 255~260 nm with a shoulder approximately 270~275 nm [86–89]. This large absorption is due to the transition from the valence band to the conduction band [87]. However, β -Ga₂O₃ usually presents intrinsic n-type conductivity without any intentional doping because native oxygen vacancies exist in it [90]. Therefore, a slight red shift occurs in the intrinsic optical absorption edge of β -Ga₂O₃ [91], resulting in some minor absorption in the blue part of the visible spectrum [18]. That is why convention β -Ga₂O₃ crystals usually appear a light yellowish color. After intentional doping, β -Ga₂O₃ crystals become bluish because of increased free carriers absorbed in the red and NIR regions of the spectrum [92].

Due to its wide band gap, β -Ga₂O₃ has a very high critical breakdown electric field (E_{br} ~8 MV/cm) [47], making β -Ga₂O₃ a promising material for high-temperature and high-power applications [93]. In principle, β -Ga₂O₃ is intrinsically an insulator. However, n-type semiconductors of β -Ga₂O₃ can be easily achieved by doping the most commonly used donor dopants, Si and Sn elements, with shallow energy level and small activation energies of 30~80 meV in β -Ga₂O₃ [94]. Therefore, the electron concentration, which is proportional to the doping concentration, is controllable in a wide range of 10^{15} ~ 10^{19} cm⁻³ [79,89,95,96] and the resistivity is also tunable in an extremely wide range of 10^{-3} ~ 10^{12} Ω ·cm [34,47] by changing the doping amount. As said previously, the effective electron mass of β -Ga₂O₃ is in the range of $0.24 m_e$ ~ $0.34 m_e$, which is relatively low and competitive with those of other wide band gap semiconductors [28,64,74]. However, the RT electron mobility (μ) in β -Ga₂O₃ is limited below 200 cm²/V·s by the LO phonon scattering [97]. Even so, its high critical breakdown electric field can compensate for this disadvantage because the Baliga's figure of merit (BFOM), which is a fundamental parameter used to determine how well-

suited a semiconductor material is for producing power devices [98,99], is proportional to the E_{br} cubed, but is only proportional to μ to the first power.

β -Ga₂O₃ has anisotropic physical, optical, and electrical properties due to its unique configuration of Ga and O atoms [61,100–102]. To illustrate, the direction with the highest thermal conductivity, 27.0 ± 2.0 W/mK, was reported to be along the [010] direction while the lowest thermal conductivity, 10.9 ± 1.0 W/mK, was along the [100] direction at normal temperature [103]. However, even the highest thermal conductivity of β -Ga₂O₃ is still much smaller than those of other conventional semiconductors such as Si or GaN. Increasing temperature will only reduce its thermal conductivity [92,103]. For instance, the thermal conductivity decreases from 21 W/mK at 20 °C to 8 W/mK at 1200 °C [92]. The limited thermal conductivity of β -Ga₂O₃ is the most crucial potential shortcoming for high-power device fabrications because excessive heat accumulation will seriously affect the performance and reliability of devices [47].

In addition to thermal conductivity, there also exist anisotropic properties in material deformation under different temperature and pressure for β -Ga₂O₃. In order to define how the size of an object changes with a change in temperature and pressure, thermal expansion coefficient and elastic constant are introduced as basic properties of certain material, respectively. Evaluating thermal expansion coefficients of material is important to estimate the extent of the lattice mismatch between the substrate and the film under heteroepitaxy growth process [104]. However, there exists stress field in the interface of the substrate and the film because of the lattice misfit caused by thermal process. Therefore, knowing the elastic stiffness constants of a power-device material are also essential to fabricate such high-temperature devices [105–108].

Thermal expansion coefficients below RT of β -Ga₂O₃ are 1.8×10^{-6} K⁻¹ for the *a*-axis and 4.2×10^{-6} K⁻¹ for the *b* and *c* axes (with respect to RT) reported by Villora et al. [109]. The expansion along the *a*-axis is 2.4 times smaller than the one along the *b* or *c*-axis. On the other hand, thermal expansion coefficients above RT (300–700 K) of β -Ga₂O₃ are 1.54×10^{-6} K⁻¹ for the *a*-axis, 3.37×10^{-6} K⁻¹ for the *b*-axis, and 3.15×10^{-6} K⁻¹ for the *c*-axis (with respect to RT) reported by Orlandi et al. [110]. The expansion coefficients for the *b* and *c* axes are almost the same and roughly double that of an even when the temperature is raised up to 1200 K. Furthermore, the increasing behavior of the thermal expansion coefficient with increasing temperature for the *a*-axis is different to those for the *b* and *c* axes [111]. These experiment results exhibit strong anisotropic behavior on the thermal expansion coefficient along the *a* axis, indicating that the (100) plane expands homogeneously [109]. In addition, when increasing temperature up to 1200 K, all three thermal expansion coefficients increase and gradually approach their high-temperature limit. This is a general saturation phenomenon that occurs when phonon modes are fully filled [111].

The mechanical properties of β -Ga₂O₃ are described by a set of elastic stiffness constants C_{ij} defined in the relation: $\sigma_i = C_{ij}\varepsilon_j$ where σ is the stress applied to the object and ε is the strain describing the deformation amount influenced by the stress both with three tensile (*i, j* = 1–3) and three shear (*i, j* = 4–6) components, giving six components in total. Note that the elastic stiffness constants are symmetry, i.e., $C_{ij} = C_{ji}$. Hence, there are 21 independent elastic stiffness constants. For a monoclinic symmetry crystal like β -Ga₂O₃, there are only thirteen independent elastic stiffness constants ($C_{11}, C_{22}, C_{33}, C_{44}, C_{55}, C_{66}, C_{12}, C_{13}, C_{23}, C_{15}, C_{25}, C_{35}$ and C_{46}) and the other eight ones are zero. β -Ga₂O₃ has unusual elastic properties: strong longitudinal-modulus anisotropy ($C_{11} = 242.8 \pm 2.9$ GPa, $C_{22} = 343.8 \pm 3.8$ GPa, $C_{33} = 347.4 \pm 2.5$ GPa, $C_{11} \ll C_{22}, C_{33}$) and strong shear-modulus anisotropy ($C_{44} = 47.8 \pm 0.2$ GPa, $C_{55} = 88.6 \pm 0.5$ GPa, $C_{66} = 104.0 \pm 0.5$ GPa, $C_{44} \ll C_{55}, C_{66}$) [112]. These anomalous elastic properties only exist in the specific space group $C2/m$. Monoclinic materials with other space group do not have these anomalous elastic properties [112]. The strong longitudinal-modulus anisotropic property ($C_{11} \ll C_{22}, C_{33}$) indicates that β -Ga₂O₃ has relatively weak chemical bonds in the [100] direction, which means β -Ga₂O₃ is more compressible along the *x*-axis than that along the *y* and *z* axes [113]. In

principle, most of the elastic stiffness constants of β -Ga₂O₃ are enhanced with increasing pressure when the hydrostatic pressure is less than 15 GPa. When the pressure is between 15 and 20 GPa, most of the elastic stiffness constants exhibit abnormal behavior, indicating that the monoclinic phase begins to transform to the rhombohedral phase of Ga₂O₃ (α -Ga₂O₃) [113], consistent with the phase transformation paragraph in the first section of the chapter.

Due to space limitations, many other basic physical properties of β -Ga₂O₃ have not yet been mentioned. These properties will be listed in Table 2, including refractive index, dielectric constant, thermal diffusivity, specific heat, etc. The basic physical quantities of β -Ga₂O₃ mentioned in this section are also listed in it.

Table 2. Basic physical properties of β -Ga₂O₃.

Property	Value	Ref.
Band gap (eV)	4.8~4.9	[82]
breakdown electric field (MV/cm)	~8	[47]
Saturation velocity (10 ⁷ cm/s)	1.8~2.0	[7]
Melting point (°C)	1793	[48]
Specific heat (J·g ⁻¹ ·K ⁻¹)	0.56	[92]
Thermal conductivity (W·m ⁻¹ ·K ⁻¹)	10.9 ± 1.0 along [100] 27.0 ± 2.0 along [010] 15.0 along [001]	[103]
Thermal diffusivity (mm ² ·s ⁻¹)	3.7 ± 0.4 along [100] 9.6 ± 0.5 along [010] 7.1 ± 0.4 along [001]	[114]
Thermal expansion (K ⁻¹)	1.54 × 10 ⁻⁶ along [100] 3.37 × 10 ⁻⁶ along [010] 3.15 × 10 ⁻⁶ along [001] 2.23 × 10 ⁻⁵ for β angle	[110]
Cleavage plane	(100), (001)	[115]
Absorption edge (nm)	270~275	[86–89]
Emission bands at RT (eV)	UV (3.2–3.6) blue (2.8–3.0) green (2.4)	[18]
Refractive index (in the visible spectrum)	1.98~2.1	[6]
High-frequency dielectric constant	3.57	[116]
Low-frequency (or static) dielectric constant	10.2 ± 0.3	[117]

3. Crystal Growth from Solution Process

A solution contains solutes and solvents. In principle, the main mission of solvents is to dissolve the solutes. However, the solvents may also hydrolyze the solutes to form insoluble substances under certain temperatures and pressure. Typical solvent of solutions could be water, various organic liquids, or their mixtures [118] depending on different requirements of hydrolyzing rate. After the hydrolysis reaction between the solutes and solvents, the solution becomes supersaturated for the insoluble substances, and crystallization occurs in the supersaturated solution [118]. A crystal is a solid in which particles are regularly arranged. Nucleation is the initial process of forming a crystal in the solution [119], in which a few ions, atoms, or molecules are dehydrated and gathered as microscopic crystalline nuclei formed either in the solution or along other surfaces. Then these nuclei will continue to grow and finally develop into large visible crystalline entities [118]. This process is often called crystal growth.

The solution process, or liquid-phase synthesis, is the most common method for preparing nanoparticles and nanostructured materials [120], whose size and shape could be well-controlled at low temperatures within a short time from minutes to hours. Furthermore, experimental processes of this kind of method are rather simple with a relatively low cost and high yield [121]. Methods for liquid-phase synthesis from compound solutions include sol-gel method, hydrothermal method, chemical bath deposition, reflux condensation method, forced hydrolysis method, successive ionic layer adsorption and reaction (SILAR) method, electrochemical deposition method, and so on. In the chapter, the basic crystal growth mechanisms of sol-gel, hydrothermal methods, and chemical bath deposition will be described in detail. Other liquid-phase methods will also be introduced briefly.

3.1. Sol-Gel Method

A colloidal solution is a kind of solution in which the size of the solute is between 10^{-9} m and 10^{-7} m. For a real solution, the size of the solute is less than 10^{-10} m in the form of molecules or ions. The solute and solvent are in one phase. In contrast, the solutes in the colloidal solution become dispersed colloidal particles suspended throughout the solvent, often called the dispersed medium in the colloidal solution [122]. When a light beam irradiates into the colloidal solution, the light beam is scattered by the colloidal particles. Then, a bright band of the light path in the colloidal solution can be observed from the perpendicular direction of the incident light. This phenomenon is called Tyndall effect. By using an ultra-microscope, you can see that these colloidal particles are suspended in the dispersed medium with random motion, which is called Brownian motion.

“Sol” is a kind of colloidal solution in which solid colloid particles are suspended in a liquid dispersed medium. In contrast to “sol”, a “gel” is a solid with three-dimensional network structures in which non-flowing liquid is dispersed. Solid becomes solvent and liquid becomes solute in the gel. The gel can be formed in the sol if these colloidal particles tend to agglomerate as inorganic polymers with connected porous structures in which the liquid dispersed medium is trapped. Or by drying to remove the solvents, the colloidal particles in the sol will poly-condense to form a gel [123].

Sol-gel method is a kind of liquid-phase synthesis using inorganic salts or metal alkoxide as precursors dissolved in organic solvents to form a solution [124]. By adding water, these precursors are hydrolyzed and poly-condensed simultaneously to agglomerate as colloidal particles so that the solution become a sol [122]. By aging the sol, the colloidal particles may further go through condensation reactions to polymerize as a gel with a network structure in the sol. In order to facilitate these colloidal particles to poly-condense as a gel, removing the solvents by thermal drying is a common method and finally an xerogel is obtained [123]. During the formation of the xerogel, the wet gel undergoes a large volume shrinkage and is easy to crack. To retain the original network of the gel and avoid cracking, supercritical drying is an essential way to dry the wet gel and an aerogel, whose liquid phase is replaced with gas, is obtained [125].

The sol-gel method, which is a kind of bottom-up method, is commonly used in fabricating nanomaterials of metal oxides, also called ceramic nanomaterial [126–128], at lower temperature between 70 and 320 °C [129–132]. Otherwise, the other methods used to produce nanomaterials need much higher temperature in the range of 1400–3600 °C [133–136]. Because the precursors in certain proportions are mixed homogeneously at a molecular scale, it is possible for the sol-gel method to make highly homogeneous nanocomposites with very high purity (99.99% purity) [122,137–140]. In addition, the sol-gel method is suitable for producing high quality nanoparticles with a narrow particle size distribution on an industrial scale [123]. However, the sol-gel method has some disadvantages such as high cost of metal alkoxides, longer processing time, toxic organic solvents for human beings, residual carbon and hydroxyl groups after drying the wet gel [141].

3.2. Hydrothermal Method

Hydrothermal synthesis is a classical method for preparing inorganic materials. This method was first studied by British geologist Sir Roderick Murchison (1792–1871) in the mid-19th century to simulate natural mineralization under strata in the condition of high temperature and high pressure. These naturally formed minerals are precipitated from hydrothermal ore solutions deep inside the earth. It can be seen that the term “hydrothermal” surely originated from geology [142]. The word hydrothermal is derived from the Greek words “hydros” and “thermos”, which mean water and heat, respectively [143]. Chemists, on the other hand, prefer to use the term, “solvothermal”, which is similar to hydrothermal, in which the water is replaced by any non-aqueous solvents. Here we only use the term “hydrothermal” to describe any chemical reactions, whether homogeneous (nanoparticles) or heterogeneous (bulk materials), occurring in a closed system with an aqueous (hydrothermal) or non-aqueous (solvothermal) solvent under high temperature and high pressure with the goal of dissolving and recrystallizing (recovering) substances that are by and large insoluble under normal circumstances [144].

It is well known that the most prevalent and significant solvent in nature is water. When increasing the temperature to 250–300 °C with higher pressure, ionic product (K_w) has a maximum value (10–100 times of normal water), which is helpful for ion reaction [145]. The enhanced concentration of OH^- will facilitate hydrolysis of the metal salts, immediately followed by a dehydration step. Under this condition, precipitates of nano-sized particles are easy to form [146], which will be dissolved again under this high temperature and pressure. In addition, the dielectric constant decreases from 78.46 to 21 when the temperature raises from 25 °C to 300 °C [145], leading to the enhancement of the hydrolysis reaction rate based on the electrostatic theory. That is why hydrothermal synthesis is usually carried out below 300 °C [147]. However, the ionic product of water drastically decreases lower than that of normal water when the temperature and pressure reach near the critical point (374.3 °C and 22.1 MPa) because the dielectric constant and density decreases drastically [142,147], which is helpful for free radical reaction [145]. In addition, water transforms from an ionic species solvent to a nonionic species solvent under supercritical conditions [148]. Therefore, supercritical water is a particularly valuable reaction medium for organic matter and gas [145].

Due to the various properties of water under high temperature and pressure, the hydrothermal technique covers processes, such as hydrothermal transformation, hydrothermal decomposition, hydrothermal synthesis, hydrothermal dehydration, hydrothermal recycling, hydrothermal metal reduction, hydrothermal crystal growth, and so on [143]. Among them, hydrothermal crystal growth is the most frequently used process, which is done in a closed vessel under pressure called “autoclave” [149]. The principle of hydrothermal crystal growth is to transport the hydrolyzed and dissolved nutrients from the hot end to the cooler end by the convection process in order to grow seed crystals through a solubility differential within the pressure vessel induced by a temperature gradient between the dissolution zone (nutrients) and the crystallization zone (seeds) [150]. Although the technique requires a slightly longer reaction time than the vapor deposition processes or milling [144], the sealed growth vessel minimizes impurities and allows for controlling the processing conditions (temperature, pressure, oxidation potential, pH, concentration of precursors, etc.) [151] in order to ensure the production of targeted sizes and morphologies of nanoparticles with high crystallinity, purity and homogeneity [144].

3.3. Chemical Bath Deposition

In comparison to sol-gel and hydrothermal methods, chemical bath deposition (CBD) is the simplest solution process which does not need expensive organic precursors and solvents like the sol-gel process or a high temperature and pressure condition in a sealed autoclave like the hydrothermal process. Unlike the former two solution processes, CBD is dedicated to thin film deposition by a controlled chemical reaction in an aqueous phase which is in analogy to chemical vapor deposition in a gaseous phase [152]. As a branch

of the solution processes, CBD has been developed for large-area thin film deposition as it has the following advantages: (1) it does not need additional expensive equipment, the precursors are easy to obtain and cheap. (2) it can be operated under low temperatures (<100 °C) and normal pressure [153]. CBD has produced a large number of thin films of metal chalcogenides, including sulfides, selenides, and oxides [154–156]. However, this method has only been used to produce a small number of thin films of divalent metal oxides (such as NiO, ZnO, and AgO) [157–159].

As stated at the beginning of this chapter, nucleation is the first step in the formation of crystals in a supersaturated solution, where a small number of ions aggregate to form microscopic nuclei. If nuclei are formed in solution, additional particles will be deposited on the nuclei without preferential orientation and larger spherical clusters will be formed [160]. This process is called homogeneous nucleation. If the nuclei are formed on phase boundaries, such as a surface of foreign substrates immersed in the solution, the nuclei will grow preferentially along the phase boundaries [161]. This process is called heterogeneous nucleation for which the barrier energy needed is lowered. That is why heterogeneous nucleation occurs more frequently than homogeneous nucleation unless the degree of supersaturation or supercooling rises [162].

CBD is a process for depositing thin films on surfaces that have been submerged in a dilute solution that contains metal ions and a source of hydroxide, sulfide, or selenide ions [163], which will combine to form metal chalcogenides. However, these ions in the solution do not always condense directly on the substrates by heterogeneous nucleation, which is usually called an ion-by-ion process (In general, the ion-by-ion process facilitates the growth of dense, sticky, mirror-like films [164]). These ions may first form colloidal particles and then agglomerate as clusters generated in the solution by homogeneous nucleation, which is caused by rapid hydrolysis of the metal ions to form precipitates. Finally, these clusters are absorbed by the substrates to form thin films [152]. This mechanism is usually called a cluster-by-cluster process, resulting in films that are opaque, non-uniform, and weakly adhering [164]. To reduce the cluster-by-cluster process and to enhance the ion-by-ion process, a chelating agent is often employed to reduce metal ion hydrolysis and to raise some stability to the bath [153].

3.4. Other Methods

In a chemical bath deposition, it is difficult to maintain a constant high temperature (<100 °C) of the bath in which chemical reactions are ongoing. It would require regular monitoring to maintain the reaction temperature not to vary too much. In addition, too much solvent is evaporated due to heating in an open vessel, causing the concentration of reactants to rise. In order to avoid losing solvent and to maintain a constant temperature, a reflux apparatus is needed for the chemical bath deposition process. In the reflux setup, solvent vapors from the liquid reaction mixture are trapped by a condenser, changing the phase from gas back to liquid form and returning to the bath. For convenience, the boiling point of the solvent is frequently chosen as the reaction temperature unless the specific temperature is essential to the reaction in which case a specialized heating apparatus would be required [165].

Forced hydrolysis of metal salt solutions is the most straightforward method for producing uniformly sized colloidal particles of metal (hydrated) oxides [166]. However, the hydrolysis rate must be slowed before forced hydrolysis because most polyvalent metal ions hydrolyze and precipitate rapidly [167]. By doing so, these metal ions can be hydrolyzed and precipitated under controlled conditions as monodispersed colloidal particles to avoid secondary nucleation, during which additional solutes are absorbed onto the existing nuclei, causing the particles to grow [168]. The forced hydrolysis method is commonly used in an acidified metal salt solution [169] or a metal salt solution with anions other than hydroxide ions [170] to prevent the hydroxide ions from rapidly combining with the metal ions. Finally, the concentration of OH⁻ ions must be enhanced to force the

hydrolysis reaction, which can be accomplished by heating the solution [169] or adding a strong base [171].

To avoid the homogeneous precipitation of cationic and anionic precursors in the reaction solution, successive ionic layer adsorption and reaction (SILAR) is introduced to modify the CBD method [172]. In this technique, thin films are deposited by immersing the substrate alternately into different solutions in which cationic and anionic precursors are separately placed and rinsing the substrate with highly purified deionized water between every immersion to remove the loosely bounded ionic species [173] so that only the tightly adsorbed layer, which is a single ionic layer, stays on the substrate [174]. The SILAR method is based on a certain ionic species coated on the substrate immersed in another solution of an opposite ionic species, which will be successively adsorbed onto the original ionic layer to react ideally at the solid–liquid interface to form a single atomic layer of a new compound within a single reaction cycle. The process is then repeated to increase the thickness of the deposited thin film [175]. Therefore, SILAR is also known as a solution-based atomic layer deposition (SALD) [176].

In a reduction-oxidation reaction of CBD, electrons spontaneously go from lower to higher redox potential with no external DC power supply. In contrast, the electrochemical deposition method is based on electrolysis of a solution to induce a redox reaction which does not spontaneously happen. In a setup of an electrolysis reaction, an electrolyte solution is connected to a DC power supply through two electrodes, an anode and a cathode, dipped into the electrolyte solution. Each electrode is made by a conductor or semiconductor material. Electrons go from the anode through the circuit connected to the power supply to the cathode. Thus, the oxidation and the reduction reactions happen on the anode and the cathode, respectively. Finally, the reduction product, a thin and firmly adherent coating of the desired metal, oxide, or salt, can be deposited onto the cathode [177]. Meanwhile, the material of the anode is oxidized and dissolved into the electrolyte solution. In principle, metal ions in the solution are reduced and a metal coating is deposited on the cathode. However, choice of the anions and the pH of the solution may facilitate other reduction reactions on the cathode, depending on the redox potential [178].

4. Ga₂O₃ Materials and Thin Films

This chapter extensively discusses synthesis of pure Ga₂O₃, co-doped Ga₂O₃, Ga₂O₃-metal oxide composite, and Ga₂O₃/metal oxide heterostructure nanomaterials via solution-based methods mainly sol-gel, hydrothermal, chemical bath methods, and solvothermal, forced hydrolysis, reflux condensation, and electrochemical deposition methods.

4.1. Ga₂O₃ by Sol-Gel Process

The sol-gel process was widely used to synthesize thin films, nanorods, nanoparticles, and nano-powders of Ga₂O₃. The properties of synthesized Ga₂O₃ depend on its morphology and size and also on the precursor used and synthesis conditions. The synthesis conditions are pH of the precursor solution, ageing time, solution temperature, deposition time and also calcination temperature. The most common phase obtained at room temperature was α -GaOOH and by calcining this phase at different temperatures, different polymorphs of Ga₂O₃ can be obtained. Figure 7 illustrates the stepwise sol-gel synthesis of Ga₂O₃ and Table 3 lists the relevant literature.

Table 3. Sol-gel synthesis of Ga₂O₃.

Method	Substrate/Template	Precursor	Synthesis Conditions	Properties	Application	Ref.
Sol-gel dip coating	BaTiO ₃ (Thickness-0.2 mm)	Gallium acetylacetonate (Ga(C ₅ H ₇ O ₂) ₃)—(A) + manganese chloride (MnCl ₂) + methanol (CH ₃ OH)—(B). Molar ratio = $(\frac{A}{A+B}) = 0.08$, Mn content: 0.3 at.%	Room Temperature (RT) stirring for 30 min, then added HCl and H ₂ O. pH of solution: 3.4, Stirring at 50 °C for 5 h under N ₂ ambient, Dip coated films dried at RT for 5 min, Pre-heat: 10 min, 600–100 °C. Process repetition: 25 times, Calcination: 850–1070 °C for 1 h in Ar ambient	Amorphous thin film of Ga ₂ O ₃ : Mn. Thickness: 2 μm	Green-Light emitting TFEL device	[12]
Sol-gel spin coating	Sapphire transducers	Gallium isopropoxide (0.15 M) + i. Ce doping—cerium isopropoxide, or ii. W doping—tungsten ethoxide, or iii. Sb doping—antimony butoxide, or iv. Zn doping—zinc acetylacetonate hydrate. Each element doping level—3 mol%	Solutions prepared in dry N ₂ ambient, Ultra sonication of mixed solution: 1 h, Aging time: 24 h, Spin coating at 3000 rpm for 30 s, dried at RT for 24 h, Calcination: 600 °C for 1 h	Ga ₂ O ₃ thin film doped with Ce, Sb, W and Zn. Thickness: 200 nm	O ₂ gas sensor	[179]
Sol-gel		Gallium(III)-isopropoxide (2.714 g) + 2-Propanol—200 mL + Hot water—200 mL (90–100 °C) + 25% w/w aqueous TMAH solution (2 mL)	Ultra-speed centrifuge: 20,000 rpm, washed with ethanol and water then dried, Calcination: 500 °C for 4 h, 900 °C for 2 h	Amorphous α and β-Ga ₂ O ₃ at 500 °C, β-Ga ₂ O ₃ at 900 °C (sub-micrometer size)		[180]
		Gallium(III)-isopropoxide (1.796 g) + Twice distilled water—50 mL (20 °C)	Ultrasonication for 1 h, liquid phase evaporation at 70 °C for 24 h. Calcination: 500 °C for 4 h, 900 °C for 2 h	(10–20 nm) sized particles of β-Ga ₂ O ₃ at 500 °C, sub-micromere size particles of β-Ga ₂ O ₃ at 900 °C		
		GaCl ₃ aqueous solution—25 mL (0.284 M) + Twice distilled water—175 mL (20 °C) + 25% w/w TMAH aqueous solution	pH: 7.82, Ageing time: 2 h, Calcination: 500 °C for 4 h, 900 °C for 2 h	Elongated and uniform sub-micron sized particles of α-Ga ₂ O ₃ at 500 °C, big agglomerates of β-Ga ₂ O ₃ with less size than that of α-Ga ₂ O ₃		
Sol-gel spin coating	Sapphire (0001)	(Gallium isopropoxide (A) + (2-Methoxyethanol + monoethanolamine (B)))—0.4 mol/L Molar ratio (C _m ratio): $(\frac{B}{A} = 1)$	Solution stirred for 1 h at 60 °C till transparent sol appear, Spin coating at 3000 rpm then dried at 90 °C for 10 min, Pre heat at 300 °C for 20 min, 6 times process repetition Calcination: 1000 °C for 1 h	Thickness: 150–200 nm The band gap of β-Ga ₂ O ₃ thin films increased due to Al doping into Ga ₂ O ₃ at 900 °C	Solar-blind Photo-detector	[181]
Sol-gel spin coating	β-Ga ₂ O ₃ (100) substrate(Thickness: 0.4 mm)	(Gallium isopropoxide (A) + (2-Methoxyethanol + monoethanolamine (B)))—0.4 mol/L Molar ratio C _m ratio: $(\frac{B}{A} = 1)$	Solution stirred for 1 h at 60 °C till transparent Sol appear, Spin coating at 3000 rpm then dried at 90 °C for 10 min, Pre heat at 300 °C for 20 min, 6 times process repetition Calcination: 1000 °C for 1 h	β-Ga ₂ O ₃ thin film grown epitaxially on β-Ga ₂ O ₃ substrate, Thickness: 120 nm	Solar-blind Photo-diode	[182]
Sol-gel		(Gallium (III) isopropoxide (Ga (Opr) ³) ₃ (2 g) + anhydrous iso-propanol (20 mL)) + 2 drops of water-isopropanol	Pre-stirring for 2 h, aged for 2 days with continuous stirring, dried in oven at 100 °C then washed with acetone & water Calcination: 600 °C for 6 h	β-Ga ₂ O ₃ mono-crystalline nanorods, Length = 100 nm		[183]
		N-phenylsalicylaldehyde modified gallium (III) isopropoxide (2 g) + anhydrous iso-propanol (20 mL)) + 2 drops of water-isopropanol	Pre-stirring for 2 h, aged for 2 days with continuous stirring, dried in oven at 100 °C then washed with acetone & water Calcination: 600 °C for 6 h	γ-Ga ₂ O ₃ polycrystalline nanoparticles, Size = 10 nm		
Sol-gel		Solution part 1: Gallium metal + HNO ₃ —(Total pH: 1–2), Solution part 2: Tetraethyl orthosilicate + (ethanol-water mixture) + Few drops of 0.1 N HCL then stirred for 1 h	Molar ratio: Ga ₂ O ₃ to SiO ₂ —10:90, 20:80 and 30:70. Both solutions mixed (pH: 1–2) then stirred for 1 h, Heated at 70 °C for 3.5 h, died at 200 °C for 4 h. Calcination: 400 °C for 11 h, 500 °C for 5 h and 900 °C for 8 h	Ga ₂ O ₃ :SiO ₂ composite nanoparticles, β-Ga ₂ O ₃ phase formation at a low temp of 400 °C for each molar ratio		[184]

Table 3. Cont.

Method	Substrate/Template	Precursor	Synthesis Conditions	Properties	Application	Ref.
Sol-gel dip coating	Amorphous quartz or Silicon	((Gallium metal + HCl) + dry ethanol)—0.075 mol/L + few drops of acetic acid	Solution stirred until it is appearing clear, Dip coated films dried at 100 °C for 5 min, Calcination: 700 °C for 1 h	β -Ga ₂ O ₃ thin film		[185]
Sol-gel	Porous alumina Template (Pore size: 200 nm)	Gallium nitrate hydrate (0.4 M) + ethanol (5 M) + concentrated aqueous ammonia diluted in ethanol (50% vol.) (0.25 M) added drop wise	Precipitates separated centrifugally then washed with DI water then peptized in nitric acid to form stable sol, Template immersed in solution for 5 s at RT then dried in air for 30 min, Calcination: 500 °C for 12 h	Hollow nano-tubes of Ga ₂ O ₃ , Length 50 μ m, Inside diameter: 100 nm and outside diameter: 200 nm		[186]
Sol-gel dip coating	Quartz and alumina substrate transducers	Solution part 1: Titanium tetraisopropoxide (A) + HCl (B) + H ₂ O (C). C _m ratio: (A:B:C=0.4:0.2:48.8) Solution part 2: Gallium (III) nitrate hydrate + hydroxypropyl cellulose (1.5 g/100 mL) +DI water	Ti:Ga atomic ratios (at./at.%) = 100:00, 75:25, 50:50 and 25:75. Part 1 peptized at 70 °C for 2 h. Part 2 stirred for 30 min, Mixed sol stirred for 2 h at 70 °C, dip coated films dried at 150 °C for 1 h Calcination: 600, 800 and 1000 °C for 1 h	Ga ₂ O ₃ retards the anatase to rutile formation of TiO ₂ , High SSA for Ti:Ga = 50:50 annealed at 600 °C	CO and NO ₂ gas sensor	[187]
Sol-gel drop casting	(100) p-Si wafer doped with boron (Thickness: 280 μ m)	Gallium nitrate hydrate + ethanol	After drop casting on substrate, films spun at 3000 rpm for 30 s, Heated at 100 °C for 30 min to evaporate ethanol, Calcination: 800 °C for 2 h in Ar ambience	β -Ga ₂ O ₃ thin film	MOS capacitor	[14]
Sol-gel drop casting	MOCVD grown GaN on sapphire	Gallium nitrate hydrate + ethanol	After drop casting on substrate, films spun at 3000 rpm for 30 s, Heated at 100 °C for 30 min to evaporate ethanol, Calcination: 800 °C for 2 h in Ar ambience	β -Ga ₂ O ₃ thin film	MOS structure	[15]
Sol-gel spin coating	Sapphire (0001)	(Gallium nitrate hydrate (A) + (2-Methoxyethanol + monoethanolamine (B)))—0.5 mol/L Molar ratio C _m ratio: ($\frac{B}{A} = 1$)	Solution stirred for 1 h at 60 °C till transparent sol appear, aged at RT for 36 h, after spin coating film kept on hot plate for 10 min, Pre heat at 500 °C for 15 min, Process repetition: 6 times, Calcination: 500 °C to 1100 °C for 2 h	Crystalline β -Ga ₂ O ₃ thin film at 700 °C and higher, Thickness: 150–200 nm	Solar-blind ultra-violet photo-detectors	[188]
Sol-gel spin coating	Sapphire (0001)	(Gallium nitrate hydrate + ethanol)—0.6 mol/L	Solution stirred at 60 °C for 90 min and aged at RT for 36 h, spin coated substrates were heated on hot plate at 100 °C for 15 min, Pre heated at 300 °C for 25 min, Process repetition: 4 times, Calcination: 500 °C–900 °C for 2 h and later at 800 °C in O ₂ , N ₂ and N ₂ -O ₂ environments for 2 h	At 600 °C—low intensity β -Ga ₂ O ₃ . At 700–800 °C— α / β polycrystalline Ga ₂ O ₃ thin film, At 900 °C—polycrystalline β -Ga ₂ O ₃ . Thickness: 240–280 nm	Photo-detector	[189]
Citrate sol-gel		Gallium nitrate + (citric acid (C ₆ H ₈ O ₇)—1.5 mole times than cations)	Stirred in water bath at 90 °C, transparent Sol dried at 200 °C, Calcination: 500 °C for 4 h in O ₂ ambience	Ga ₂ O ₃ sub-micro powders		[190]
Sol-gel spin coating	Sapphire (0001)	(Gallium nitrate(A) + ethanol)—0.4 mol/L) + monoethanolamine (B), C _m ratio: ($\frac{B}{A} = 1$)	Spin coated at 1000 rpm for 50 s, Pre-heating of films at 100–500 °C in O ₂ ambient for 10 min, Calcination: 1000 °C in O ₂ ambient for 2 h	β -Ga ₂ O ₃ thin films		[191]

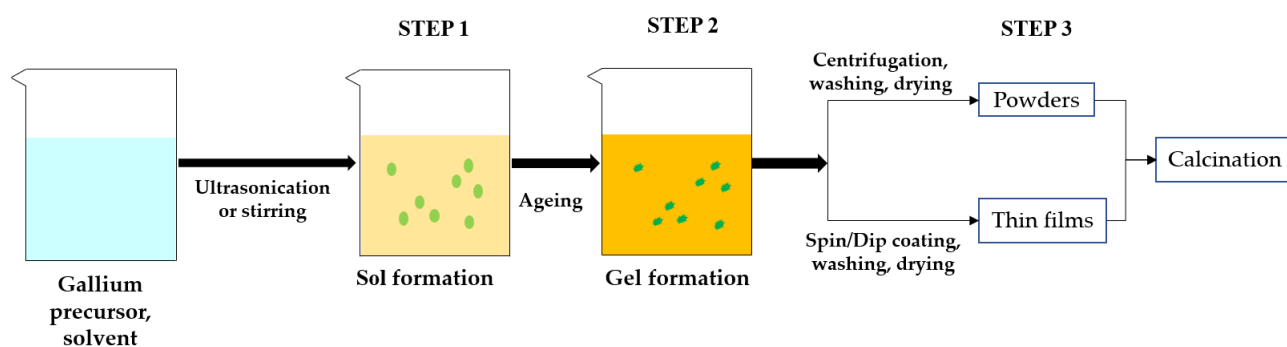
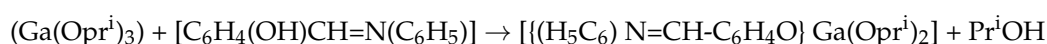


Figure 7. A schematic of sol-gel preparation of gallium oxide illustrating all steps involved.

The various precursors used to synthesize Ga_2O_3 nanomaterials were gallium acetylacetonate [12], gallium isopropoxide [179–183], Gallium(III) chloride aqueous solution [180], Ga metal [184,185] and gallium nitrate hydrate [14,15,186–191]. G. Sinha et al. [192] prepared the pure Ga_2O_3 nanocrystalline thin film on quartz substrate for the first time by the sol-gel method and analyzed the effect of annealing temperature on phase variation of the deposited film. The as-deposited GaOOH phase converted to pure $\alpha\text{-Ga}_2\text{O}_3$ at $500\text{ }^\circ\text{C}$ and pure $\beta\text{-Ga}_2\text{O}_3$ at $700\text{ }^\circ\text{C}$ and higher temperatures. The synthesized $\text{GaO}(\text{OH})$ had a band gap of 5.27 eV , pure $\alpha\text{-Ga}_2\text{O}_3$ has a band gap of 4.98 eV , and the band gap of $\beta\text{-Ga}_2\text{O}_3$ varied from 4.8 to 4.7 eV when annealed in the temperature range of $700\text{ }^\circ\text{C}$ to $1100\text{ }^\circ\text{C}$.

M. Tadatsugu et al. [12] prepared thin films of $\text{Ga}_2\text{O}_3\text{:Mn}$ for the first time via the sol-gel dip-coating method. The $\text{Ga}_2\text{O}_3\text{:Mn}$ thin films annealed for 1 h at $850\text{--}1070\text{ }^\circ\text{C}$ in Ar ambience and had an amorphous nature.

Y. Li et al. [179] synthesized sol-gel prepared Ga_2O_3 semiconducting thin film doped with Ce, Sb, W, and Zn. The spin-coated films were annealed at $600\text{ }^\circ\text{C}$ for 1 h to get Ga_2O_3 thin film. M. Ristic et al. [180] synthesized nanoparticles of $\alpha\text{-Ga}_2\text{O}_3$ and $\beta\text{-Ga}_2\text{O}_3$ using gallium(III)-isopropoxide and aqueous GaCl_3 solution as starting materials. A dominant amorphous phase and crystalline $\alpha\text{-GaOOH}$ particles were obtained by addition of hot water and then aqueous TMAH solution to 2-propanol solution of gallium (III)-isopropoxide. Aggregates of amorphous $\alpha\text{-GaOOH}$ consist of nanoparticles. At room temperature, hydrolysis of gallium (III)-isopropoxide with pure water yielded an amorphous phase only. Polymerization and condensation of gallium (III)-isopropoxide hydrolytic products can explain the formation of this amorphous phase. The addition of aqueous TMAH solution into aqueous GaCl_3 solution resulted in a single-phase of $\alpha\text{-GaOOH}$ particles (submicrometric range). The formation of $\alpha\text{-GaOOH}$ particles can be explained by a fast, solution-mediated transformation of hydrated $\text{Ga}(\text{OH})_3$. Y. Kokubun et al. [181] synthesized the $\beta\text{-Ga}_2\text{O}_3$ thin film on sapphire substrate by the sol-gel method. A major diffraction peak of (201) corresponding to $\beta\text{-Ga}_2\text{O}_3$ appeared in all the films when annealed at $400\text{ }^\circ\text{C}$ to $1200\text{ }^\circ\text{C}$ for 1 h . The optical absorption studies confirmed that the band gap of the film annealed at $800\text{ }^\circ\text{C}$ has 4.95 eV . When the annealing temperature increases above $900\text{ }^\circ\text{C}$, the lattice constants of the $\beta\text{-Ga}_2\text{O}_3$ films decreased and the band gap increased due to diffusion of Al from sapphire substrates into Ga site in $\beta\text{-Ga}_2\text{O}_3$ lattice. The diffusion of Al into Ga site has been seen in the other synthesis methods, such as sputtering [193] and CVD [194]. R. Suzuki et al. [182] grew $\beta\text{-Ga}_2\text{O}_3$ thin films epitaxially on a 0.4 mm thick (100) $\beta\text{-Ga}_2\text{O}_3$ substrate using the sol-gel method similar to the method reported in [181]. R. Gopal et al. [183] synthesized $\beta\text{-Ga}_2\text{O}_3$ mono-crystalline nanorods by the sol-gel method using hydrolyzation of the precursor solution containing gallium(III) isopropoxide ($\text{Ga}(\text{Opr}^i)_3$) dissolved in anhydrous iso-propanol. They also synthesized $\gamma\text{-Ga}_2\text{O}_3$ polycrystalline nanoparticles by hydrolysis of a new modified precursor $[(\text{H}_5\text{C}_6)\text{N}=\text{CH}-\text{C}_6\text{H}_4\text{O}]\text{Ga}(\text{Opr}^i)_2$, which was derived by a reaction between $(\text{Ga}(\text{Opr}^i)_3)$ and N-phenylsalicylaldimine $[(\text{C}_6\text{H}_4(\text{OH})\text{CH}=\text{N}(\text{C}_6\text{H}_5))]$ in refluxing benzene medium:



After the hydrolysis of the above precursor solutions, β -Ga₂O₃ and γ -Ga₂O₃ phases were created by sintering the occurred products at 600 °C for 6 h. The average crystallite sizes of β -Ga₂O₃ nanorods and γ -Ga₂O₃ nanoparticles measured from XRD patterns were 120 nm and 32 nm, respectively, which are larger than TEM measured values of 100 nm (i.e., diameter of nanorods) and 10 nm (i.e., nanoparticles) due to antistrophic strains. The SEM and TEM images β -Ga₂O₃ nanorods and γ -Ga₂O₃ particles are shown in Figure 8.

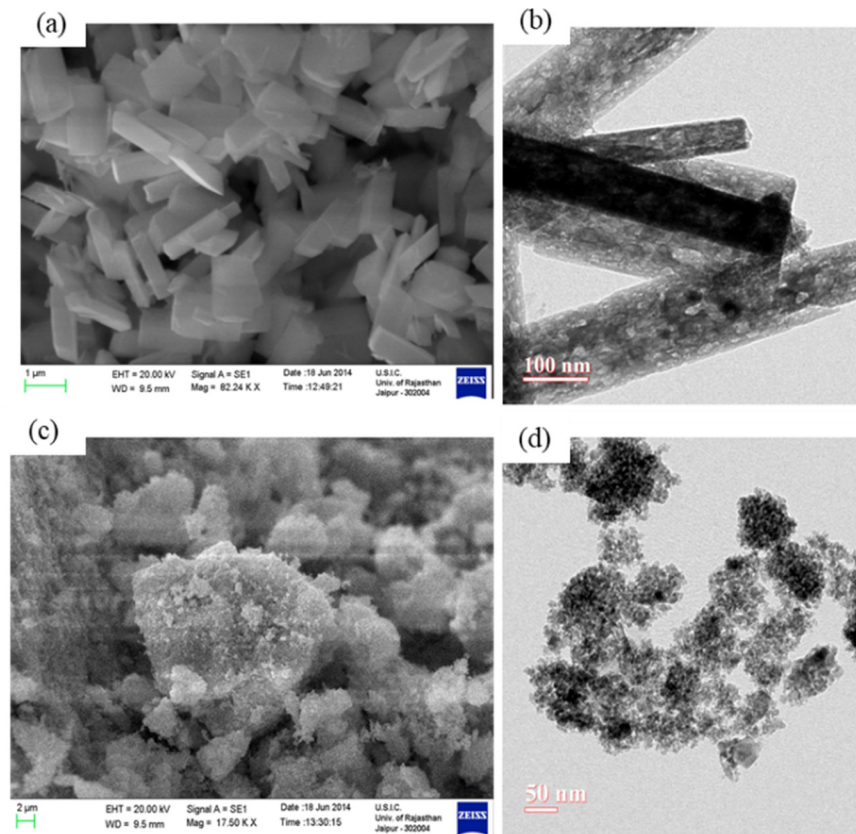


Figure 8. (a,c) SEM and (b,d) TEM images of β -Ga₂O₃ (a,b) and γ -Ga₂O₃ (c,d). Reprinted figure with permission from [183]; copyright (2018) by Elsevier.

G. Sinha et al. [184], prepared the Ga₂O₃ nanoparticles of finite size in silica matrix by the sol-gel method. The crystallite sizes of Ga₂O₃ in the Ga₂O₃:SiO₂ composites (molar ratio: 10:90, 20:80, and 30:70) were found to be 1.2, 1.81, and 1.9 nm, respectively. They observed that β -Ga₂O₃ was formed in composite at a very low temperature of 400 °C, which was in contrast to their previous study [192]. This was explained by the capping effect of silica that confines the Ga₂O₃ to a very small size [195]. The band gap (E_g) of Ga₂O₃:SiO₂ (10:90) composite was 5.51 eV, which had a significant deviation from the bulk material (4.9 eV [196]) and was considered to be the effect of nanosized β -Ga₂O₃ particles in the silica matrix. The PL studies revealed that the Ga₂O₃:SiO₂ composites had shown a strong blue emission peak at 460 nm, which was proved in the previous study by Binet and Gourier [196]. They also used sol-gel prepared pure β -Ga₂O₃ thin film as a substrate for Ga₂O₃ nanowire fabrication by the VLS method [185]. The film had shown a (202) diffraction peak with lower crystallinity when annealed at 700 °C for 1 h.

B. Cheng et al. [186] prepared the hollow nanotubes of crystalline β -Ga₂O₃ by the sol-gel method for the first time using a porous alumina template with gallium nitrate hydrate as starting materials. M.R. Mohammadi et al. [187] used the particulate sol-gel method to synthesize the mesoporous TiO₂ and Ga₂O₃ thin films on quartz and alumina substrate transducers with various Ti:Ga atomic ratios (at.%/at.%) = 100:00, 75:25, 50:50 and 25:75. A polymeric fugitive agent (PFA), such as hydroxypropyl cellulose, was added to solution

to enhance the porosity of the films in nanoscale. The average crystallite size of synthesized $\text{TiO}_2\text{-Ga}_2\text{O}_3$ powders (i.e., 2–5 nm) less than that of pure TiO_2 powders (i.e., 4–10 nm) confirms that Ga_2O_3 retards the anatase to rutile formation of TiO_2 by preventing the grain growth and crystallization. A. Kaya et al. [14] synthesized the $\beta\text{-Ga}_2\text{O}_3$ thin films on a p-type Si substrate using the sol-gel method by annealing the as-synthesized films at a temperature of 800 °C for 2 h in Ar ambience. In XRD studies, the annealed films showed major intensities for (400) and $(\bar{1}10)$ planes corresponding to $\beta\text{-Ga}_2\text{O}_3$. J. Gao et al. [15] synthesized $\beta\text{-Ga}_2\text{O}_3$ thin films coated on MOCVD grown GaN substrate by using the sol-gel method similar to their previous work [14]. H. Shen et al. [188] synthesized $\beta\text{-Ga}_2\text{O}_3$ thin films on c-plane sapphire substrate by a sol-gel spin coating technique. In XRD studies, the film annealed at 700 °C showed (201) and (603) planes corresponding to $\beta\text{-Ga}_2\text{O}_3$, and with an increase in the annealing temperature, the peak intensities were increased. All the $\beta\text{-Ga}_2\text{O}_3$ films showed 90% transmittance over 300 nm. The optical band gap (E_g) of the films measured from the transmittance spectra revealed that when the annealing temperature of the films increased from 500 °C to 700 °C, E_g was increased monotonously from 5.07 eV to 5.24 eV and exceeded to 5.67 eV at 1100 °C. This rapid increase of band gap was explained by the diffusion of Al from alumina substrate into the Ga site in $\beta\text{-Ga}_2\text{O}_3$, which was already seen in a previous study [181].

M. Yu et al. [189] synthesized the α/β polycrystalline Ga_2O_3 thin films introducing $\alpha\text{-Ga}_2\text{O}_3$ into $\beta\text{-Ga}_2\text{O}_3$ on sapphire substrate by a novel sol-gel method. When as-synthesized film annealed in air at 600; it had shown low intensities peaks corresponding to $\beta\text{-Ga}_2\text{O}_3$ phase. At annealing temperatures of 700 °C and 800 °C, the (006) orientation of $\alpha\text{-Ga}_2\text{O}_3$ co-existed with $\beta\text{-Ga}_2\text{O}_3$. At 900 °C, the (006) orientation of $\alpha\text{-Ga}_2\text{O}_3$ disappeared completely making the film fully into $\beta\text{-Ga}_2\text{O}_3$ phase. The as-synthesized film was annealed at 800 °C to study the influence of different annealing environments (namely O_2 , N_2 and $\text{N}_2\text{-O}_2$). It is revealed that the rich O_2 environment would enhance the growth of $\alpha\text{-Ga}_2\text{O}_3$ and poor O_2 would suppress it. AFM images revealed that the sample annealed in an O_2 atmosphere had a dense surface with a small RMS value of 4.17 nm, which was attributed to oxygen vacancy compensation and increased crystallinity. While the RMS value of the sample annealed in N_2 ambience was 10.4 nm due to the presence of a large number of oxygen vacancies. The band gap from the Tauc plot for the films annealed in N_2 , O_2 and $\text{N}_2\text{-O}_2$ atmospheres was 4.9 eV, 5.09 eV, and 5.04 eV, respectively. The oxygen vacancies acted as trap states at the top of the valence band, extending into the forbidden band and causing the narrow band gap. Figure 9 shows the SEM and AFM images of high quality α/β polycrystalline Ga_2O_3 thin film that occurred at an annealing temperature of 800 °C in O_2 atmosphere.

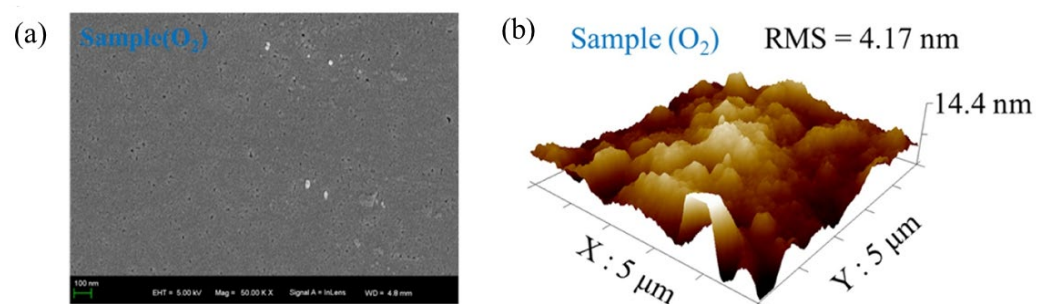


Figure 9. (a) SEM and (b) AFM images of high quality α/β polycrystalline Ga_2O_3 thin film annealed at 800 °C in O_2 atmosphere. Reprinted figure with permission from [189]; copyright (2020) by Elsevier.

S. Yu et al. [190] derived Ga_2O_3 sub-micro powders by the citrate sol-gel method. The Ga_2O_3 powders were obtained by calcination of the dried sol at 500 °C for 4 h in an O_2 atmosphere. The particle size for these powders measured with SEM was less than 1 μm . These ceramic powders were sintered via SPS at 830–980 °C for 5 min under a pressure of 90 Mpa. The $\beta\text{-Ga}_2\text{O}_3$ sample that occurred by sintering at 980 °C had a transmittance

higher than 40% in the wavelength range of 396–667 nm and its SEM image was shown in Figure 10.

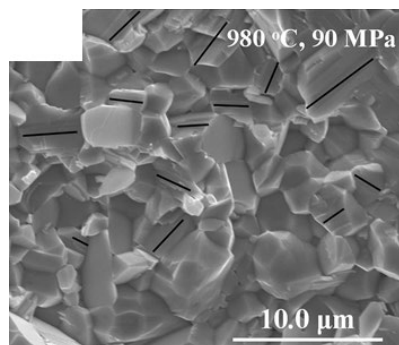


Figure 10. SEM image of β -Ga₂O₃ sample sintering obtained via SPS at 980 °C @ 90 Mpa. Reprinted figure with permission from [190]; copyright (2020) by Elsevier.

Y. Zhu et al. [191] successfully synthesized the β -Ga₂O₃ thin films on (0001) sapphire substrate by a simple and effective sol-gel spin coating method. The SEM images of β -Ga₂O₃ films synthesized with pre-heating temperatures of 100 °C and 200 °C had surface cracks, while the 300–500 °C pre-heated films were crack-free and very flat. They reported that these cracks are due to volatilization of organic solvent under low pre-heating temperatures and oxidative decomposition under high-temperature crystallization. The AFM studies revealed that β -Ga₂O₃ films preheated at <300 °C had more RMS value, which was explained by obvious porosity. The β -Ga₂O₃ film prepared with a pre-heating temperature of 400 °C had a low RMS value of 1.982 nm. The XRD studies revealed that the synthesized β -Ga₂O₃ films had peaks corresponding to {201} family of planes, which proved the epitaxial relationship of β -Ga₂O₃ [201]// [0001]Al₂O₃ and the same was reported in other studies [197,198]. The XRD study of 400 °C pre-heated and 1000 °C post annealed β -Ga₂O₃ thin film grown on the ~7° off angled sapphire substrate revealed that the film had the major peak corresponding to (400) plane of β -Ga₂O₃ which supports the out-plane epitaxial relationship of β -Ga₂O₃ [400]// [11 $\bar{2}$ 3]Al₂O₃ for the β -Ga₂O₃ films grown on ~7° off angled sapphire substrate [199,200].

4.2. Ga₂O₃ by Hydrothermal Process

The hydrothermal method was widely used to synthesize various morphologies of Ga₂O₃ materials. The properties of Ga₂O₃ materials and its morphologies typically depend on the type of Ga precursor, surfactant, and synthesis conditions, such as pH of the solution, ageing time, reaction temperature, and reaction time and also on calcination temperature. Morphologies of thin films by hydrothermal method could depend on the type of the seed layer. Figure 11 illustrates the stepwise hydrothermal synthesis of Ga₂O₃, and Table 4 lists the relevant literature.

The various precursors used to synthesize Ga₂O₃ nanomaterials were gallium acetylacetonate [201], commercial Ga₂O₃ [45], Gallium(III) chloride aqueous solution [43,201], Ga metal [202], and gallium nitrate hydrate [21,203–231].

S. Suman et al. [201] synthesized gallium oxide nanostructures via the hydrothermal method using three different precursors of gallium, such as gallium acetylacetonate (GO-Ga), gallium chloride (GO-Cl), and gallium nitrate (GO-Ni), and studied its effect on morphology. The morphology of Ga₂O₃ nanostructures prepared with gallium acetylacetonate was cuboid in shape (average size of 0.6 μ m \times 0.3 μ m \times 0.2 μ m), while the nanostructures prepared with gallium chloride and gallium nitrate were of a rice-like morphology and of average size, (L \times W) 1.5 μ m \times 0.5 μ m and 1.3 μ m \times 0.5 μ m, respectively. The β -Ga₂O₃ phase started forming at an annealing temperature of 800 °C.

Table 4. Hydrothermal synthesis of Ga₂O₃.

Method	Substrate/Template	Precursor	Synthesis Conditions	Properties	Applications	Ref.
hydrothermal method		Gallium acetylacetonate (0.1 M) + DI water	NH ₄ OH added to the transparent solution dropwise till pH-10, Solution stirred at 65 °C for 5 h continuously, Reaction at 140 °C for 10 h, dried at 70 °C for 6 h, Calcination: 600 °C, 800 °C, 850 °C, 950 °C and 1000 °C	Cuboid shape β-Ga ₂ O ₃ starting from 800–850 °C, Pore size was maximum at 950 °C		[201]
		Gallium chloride (0.1 M) + DI water		Rice like morphology β-Ga ₂ O ₃		
		Gallium nitrate (0.1 M) + DI water		Rice like morphology β-Ga ₂ O ₃		
hydrothermal method		(Commercial Ga ₂ O ₃ + HCl) + DI water—35 mL (Commercial Ga ₂ O ₃ + HCl) + DI water—35 mL + solvent of diethylene glycol (DEG) and water (1:1)	NaOH solution added till pH = 6–8 Reaction in autoclave at 180 °C for 24 h, hydrothermal crystals filtered, washed and dried at 60 °C for 6 h, Calcination: 900 °C	-At pH 6, β-Ga ₂ O ₃ regular quadrilateral nanorods (width: 200–300 nm) -At pH 8 spindle like β-Ga ₂ O ₃ nanorod arrays formed		[45]
hydrothermal method		(GaCl ₃ aqueous solution + water) + (TMAH (CH ₃) ₄ NOH) aqueous solution (25% w/w))	-pH was adjusted to 5, 7 and 9 by adding TMAH gradually, shaken for 5 min, ✓ Reaction at 60 °C (Aging time: pH-5: 5–7 days, pH-7: 1 day and pH-9: 2 days) or ✓ Reaction at 160 °C for 2 h. Calcination: 500 and 900 °C for 2 h	Uniform submicron particles of different shapes (rhombic rods, rhombic prisms, hierarchical structures) of α-Ga ₂ O ₃ at 500 °C and β-Ga ₂ O ₃ at 900 °C		[43]
hydrothermal method		Gallium metal—0.2 g + DI water—60 mL	Reaction in autoclave at 160 °C for 12 h, precipitate collected by centrifugation then dried at 70 °C, Calcination: Pre heat at 400 °C for 5 h then at 600–800 °C for 1.5 h	Rod-like morphology mixed phase of α-Ga ₂ O ₃ and β-Ga ₂ O ₃ at 700 °C	Photocatalyst	[202]
hydrothermal method		((Ga(NO ₃) ₃ + water)—0.012 mol/L) + NaOH solution (1.5 M) + 0.036 mol NaOH), kept in shaking bath (100 rpm) at 80 °C for 2 h	PEO or CTAB (0.0048 mol) added	Stirring at RT for 2 h. Reaction at 100 °C for 48 h. Dried at 80 °C	PEO-β-Ga ₂ O ₃ quadrilateral rods length—2.56 μm, CTAB-β-Ga ₂ O ₃ quadrilateral prisms length—2.56 μm CTAB sample has larger pore size than PEO sample.	[203]
		((0.003 mol Ga(NO ₃) ₃ + water (10 mL)) + (0.015 mol NaNO ₃ + water—10 mL)), kept in shaking bath (100 rpm) at 80 °C for 2 h	PEO or CTAB (0.0025 mol) added	HNO ₃ added dropwise at 80 °C to adjust pH = 9.5	Amorphous agglomerates and nanotubes of γ-Ga ₂ O ₃ (length ≤ 60 nm, <i>d_{ext}</i> = 0.8–3 nm), More number of nanotubes with PEO than CTAB	
hydrothermal method		((Ga(NO ₃) ₃ ·nH ₂ O (A) + DI water)—0.01 mol/L) + SDBS (B), C _m ratio: ($\frac{B}{A} = \frac{1}{10}$)			Brush-like particles composed with the nanowires	
		((Ga(NO ₃) ₃ ·nH ₂ O (A) + DI water)—0.01 mol/L) + SA (B), C _m ratio: ($\frac{B}{A} = \frac{1}{10}$)	Reaction in autoclave at 140 °C for 10 h, Products separated, washed with DI water then dried in atmosphere ambient, Calcination: 600 °C or 900 °C for 5 h		Cuboid-like particles	[204]
		((Ga(NO ₃) ₃ ·nH ₂ O + DI water)—0.01 mol/L)			Spindle like particles	
hydrothermal method		((Ga(NO ₃) ₃ ·xH ₂ O + DI water—8 mL) + NaOH—207 mg) + oleic acid—1.68 mL) + 1.5 mL of oleic acid + 6 mL of ethanol) + Na ₂ S·9H ₂ O—96 mg	Reaction in autoclave at 140 °C for 4, 6, 8 and 16 h. Products collected, washed then dried under vacuum at 70 °C for 8 h. Calcination: 1000 °C for 10 h	β-Ga ₂ O ₃ microspheres with hollow interior		[205]
hydrothermal method		(50 mL of Ga(NO ₃) ₃ —0.0508 mol/L + 50 mL of oxalic acid (C ₂ H ₂ O ₄) (0.155–0.666 mol/L)) using water as solvent	Rigorous stirring on a hot plate at 90 °C, Reaction in autoclave at temperatures varying from (175–225 °C) for 10 h. Calcination: 450 °C for 3 h	Calcination of GaOOH prepared at reaction temp 200 °C were resulted into α-Ga ₂ O ₃ microspheres	Photocatalyst	[206]

Table 4. Cont.

Method	Substrate/Template	Precursor	Synthesis Conditions	Properties	Applications	Ref.
hydrothermal method		(Ga(NO ₃) ₃ ·xH ₂ O—0.01 g) + water—20 mL + C ₃ H ₇ NO—5 mL + C ₈ H ₁₆ N ₂ O ([Bmin][OH])—0.05 g	Precipitates collected, washed and dried at 60 °C, Reaction in autoclave at 180 °C for 24 h. Calcination: 450 °C for 3 h	Mesomorphs α-Ga ₂ O ₃ hierarchical structures	Photo degradation	[207]
hydrothermal method		(Ga(NO ₃) ₃ —2.55 g (10 mmol) + (biuret—6.18 g (60 mmol)), Each solution prepared using 50 mL of water as solvent	Heated up to boiling, then stirred for 30 min, Reaction in autoclave at 200 °C for 10 h, dried at 120 °C for 2 h, Calcination: 450 °C for 3 h	Mesoporous α-Ga ₂ O ₃ microrods		[208]
		(Ga(NO ₃) ₃ —2.55 g (10 mmol) + (oxalic acid—7.56 g (60 mmol)), Each solution prepared using 50 mL of water as solvent	Solution heated up to boiling, then stirred for 30 min, Reaction in autoclave at 200 °C for 14 h, dried at 120 °C for 2 h, Calcination: 450 °C for 3 h	Mesoporous α-Ga ₂ O ₃ micro flowers		
hydrothermal method	Carbon spheres as templates	(Ga(NO ₃) ₃ ·xH ₂ O—1.3544 g (6 mmol) + urea—1.8 g (30 mmol) + carbon colloid solution	Reaction in autoclave at 90 °C for 48 h, Dried at RT for 24 h, Calcination: 500 °C (1 °C/min), 600–800 °C (10 °C/min) for 1 h	Uniform β-Ga ₂ O ₃ hollow nanostructures at 700 °C.		[209]
		Ga(NO ₃) ₃ ·xH ₂ O—15 mL (0.3 mol/L) + (urea—3.5 g + DI water—15 mL)	Urea solution was kept 90 °C for 1 h then added to solution, Reaction at 140 °C for 1, 3 and 10 h, solution centrifuged, precipitates collected then washed and dried, Calcination: 900 °C for 3 h	β-Ga ₂ O ₃ nanorods		[210]
Micro-wave hydrothermal method		Ga(NO ₃) ₃ —10 mL (0.166 mol/L) + (urea (2.0, 2.7, 3.4, 4.1 g) + DI water—10 mL)	Solution stirred at 60 °C for 30 min, Heated to 100 °C in 3 min @ 400 W then to 130–150 °C in 2 min @ 600W and maintained there for 1–4 min, Calcination: 300–700 °C for 2 h	Ultrafine γ-Ga ₂ O ₃ nanocrystals at 140 °C for 2 min maintaining time, Phase change to β-Ga ₂ O ₃ at 600 °C	Photo degradation	[211]
hydrothermal method		(Ga(NO ₃) ₃ ·9H ₂ O—1.6 g + urea—2.64 g + PEG—20 mL + 70 mL—DI water)	Solution stirred vigorously for 2 h at 25 ± 1 °C, Reaction in autoclave at 140 °C for 6 h, Precipitates filtered, washed with ethanol, Calcination: 800 °C for 2 h	Mesoporous β-Ga ₂ O ₃ nanorods	Photocatalyst	[212]
		(Ga(NO ₃) ₃ ·9H ₂ O (0.01 mol) + urea (0.1 mol) + PEG—200) using DI water as solvent	Stirred at RT for 1 h, Reaction in autoclave at 160 °C for 8 h, Dried at 100 °C for 24 h, Products separated by centrifugation, washed with alcohol then dried at 100 °C for 24 h, Calcination: 800 °C for 10 h	β-Ga ₂ O ₃ nanorods	Photocatalytic degradation	[213]
hydrothermal method		(Ga(NO ₃) ₃ ·nH ₂ O + DI water)—0.015 mol/L	Reaction in autoclave at 150 °C for 24 h, Solid products collected and washed and dried at RT, Calcination: 700 °C for 1 h.	Rod like morphology polycrystalline β-Ga ₂ O ₃ films		[214]
		Ga(NO ₃) ₃ ·nH ₂ O (0.1 M) + DI water—100 mL	NH ₄ OH added to adjust solution pH-9, Reaction at RT to 95 °C for 5 h, Calcination: 500, 800 and 1000 °C for 3 h	α-Ga ₂ O ₃ nanorods at 500 °C, β-Ga ₂ O ₃ nanorods at 800 and 1000 °C	Photocatalytic degradation	[21]
		Ga(NO ₃) ₃ ·xH ₂ O (0.1M) + DI water—50 mL	NH ₄ OH- (28–30% NH ₃ in solution) added to make pH-10, Stirred at 60 °C while aging for 10 min–6 h, Reaction at 140 °C for 10 h, dried at 70 °C for 6 h, Calcination: 1000 °C for 5 h	β-Ga ₂ O ₃ nanorods	FET	[215]
		Ga(NO ₃) ₃ —1.02292 g (0.05 M) + DI water—80 mL	NH ₄ OH solution added till pH-9, Reaction in autoclave at 95 °C for 5 h, Precipitates separated by centrifugation then dispersed in 5 mL DI water and dried at 75 °C, Calcination: 150 °C, 400–1000 °C in ambient air for 5 h	α-Ga ₂ O ₃ nanorods at 400–700 °C, β-Ga ₂ O ₃ nanorods at 900 °C and 1000 °C	CO ₂ gas sensing	[216]
		((Ga(NO ₃) ₃ ·xH ₂ O (0.05 M) + DI water)—160 mL)	Various amounts (1, 1.5, 2, 3 and 6 mL) of NH ₄ OH was added to get different pH = 5, 7, 9, 11 and 14, Reaction at 100 °C for 5 h, dried overnight at 75 °C, Calcination: 1000 °C for 5 h	β-Ga ₂ O ₃ nano powder	NH ₃ gas sensor	[217]
	Ga(NO ₃) ₃ ·9H ₂ O—15 mL (0.3 mol/L)	NH ₄ OH added dropwise till pH-10, Reaction at 40, 80, 120 and 160 °C for 18 h, Centrifuged, washed and dried, Calcination: 900 °C for 3 h	β-Ga ₂ O ₃ microspheres		[218]	

Table 4. Cont.

Method	Substrate/Template	Precursor	Synthesis Conditions	Properties	Applications	Ref.
	Sputter coated 50 nm thick SnO ₂ seed layer on 1 μm SiO ₂ /Si (100)	Ga(NO ₃) ₃ ·9H ₂ O—0.6 g + DI water—40 mL	Seed layer annealed at 900 °C for 2 h, Solution pH-2, Substrates incubated in solution at 150 °C for 12 h in autoclave, Calcination: 1000 °C for 4 h	β-Ga ₂ O ₃ nanorod arrays (NRAs)	CO gas detection	[219]
	Sputter coated 50 nm thick SnO ₂ seed layer on 1 μm SiO ₂ /Si (100)	Ga(NO ₃) ₃ ·9H ₂ O—0.6 g + DI water—40 mL	Seed layer annealed at 900 °C for 2 h, Solution pH-2, Reaction at 150 °C for 12 h, dried overnight at 80 °C, Calcination: 1000 °C for 4 h	β-Ga ₂ O ₃ nanorod arrays (NRAs)	NO ₂ gas sensor	[220]
	Si (100)	Nucleation (solution-1): Ga(NO ₃) ₃ ·9H ₂ O—0.2 M + ethanol—10 mL + DI water—30 mL. Crystal Growth (solution-2): Ga(NO ₃) ₃ ·9H ₂ O—0.2 M + DI water—30 mL.	SiO ₂ oxide layer eliminated by etching with HF, Nucleation: Reaction in solution-1 at 100 °C for 30 min, Growth: Reaction in solution-2 at 150 °C for 12 h, dried at 50 °C for 60 min, Calcination: 800 °C for 4 h	β-Ga ₂ O ₃ micro rod arrays (MRAs)		[221]
	Si (100)	Nucleation (solution-1): Ga(NO ₃) ₃ ·9H ₂ O—0.2 M + ethanol—10 mL + DDI water—30 mL. Crystal Growth (solution-2): Ga(NO ₃) ₃ ·9H ₂ O—0.2 M + DDI water—30 mL.	SiO ₂ oxide layer eliminated by etching with HF, Nucleation: Reaction in solution-1 at 100 °C for 60 min, Growth: Reaction in solution-2 at 150 °C for 12 h, dried at 70 °C for 2 h, Calcination: 800 °C for 4 h	β-Ga ₂ O ₃ nanoflakes	β-Ga ₂ O ₃ /p-Si hetero junction self-powered photodiode	[222]
hydrothermal method	FTO glass	(Ga(NO ₃) ₃ —0.3 g + DI water)—30 mL	Reaction at 150 °C for 12 h, Calcination: Pre-annealed at 400 °C for 4 h then annealed at 700 °C for various times or annealed from 770–830 °C for 20 min	α-Ga ₂ O ₃ NRAs and α/β-Ga ₂ O ₃ phase junction NRAs	Solid-state type photodetector, photoelectron-chemical type photodetector	[223]
	FTO glass	(Ga(NO ₃) ₃ ·9H ₂ O—0.3 g + DI water—30 mL)—0.0239 M	Reaction at 150 °C for a night, dried at 80 °C, Calcination: Pre-annealed 400 °C for 4 h then annealed at 700 °C for 20 min	α/β-Ga ₂ O ₃ phase junction NRAs	Self-powered solar-blind photodetector	[224]
	A layer of SnO ₂ on the surface of the FTO glass	(Ga(NO ₃) ₃ + DI water)—0.39 mol/L	Hydrothermal reaction at 150 °C for 12 h, dried, Calcination: 400 °C for 4 h	Hexagonal prism like α-Ga ₂ O ₃ NRA, average length—1.62 μm and average diameter 80–200 nm	Self-powered spectrum-distinguishable α-Ga ₂ O ₃ NRA/Cu ₂ O microsphere (MS) p-n junction electro-chemical photodetector	[225]
	Spin coated Ga ₂ O ₃ seed layered FTO glass	(Ga(NO ₃) ₃ ·9H ₂ O—0.3 g + DI water—30 mL)—0.0239 M	Seed layer annealed at 450 °C for 30 min, Reaction at 150 °C for 12 h, washed with DI water then dried at 80 °C, Calcination: 700 °C for 4 h	β-Ga ₂ O ₃ NRAs	Solar-blind deep UV photodetector	[226]
	Spin coated Ga ₂ O ₃ seed layer on FTO substrate	Ga(NO ₃) ₃ ·9H ₂ O—30 mL (0.03 M) + hexamine (C ₆ H ₁₂ N ₄) (0.005 M)		α-Ga ₂ O ₃ nanorod arrays (NRAs)		
	GaOOH NRAs prepared by hydrothermal method as above	Al(NO ₃) ₃ ·9H ₂ O (0.005 M, 0.01 M, 0.015 M) + C ₆ H ₁₂ N ₄ (0.005 M)	Reaction at 180 °C for 12 h, Calcination: 500 °C for 4 h	α-Ga ₂ O ₃ nanorod was completely covered by γ-Al ₂ O ₃	Ga ₂ O ₃ -Al ₂ O ₃ heterojunction PEC Self-powered UV detector	[227]

Table 4. Cont.

Method	Substrate/Template	Precursor	Synthesis Conditions	Properties	Applications	Ref.
hydrothermal method		$((\text{Ga}(\text{NO}_3)_3 \cdot x\text{H}_2\text{O} (0.1 \text{ M}) + \text{DI water} - 50 \text{ mL}) + \text{SnCl}_4 - 0, 0.026, 0.052, 0.130 \text{ and } 0.260 \text{ g})$	NH_4OH (28% in H_2O) added to solution at 60°C to till pH-10, Reaction at 140°C for 10 h, dried at 70°C for 6 h, Calcination: 1000°C in O_2 ambient for 6 h	$\beta\text{-Ga}_2\text{O}_3$ nanostructures	Photocatalyst	[228]
		$\text{Ga}_2(\text{NO}_3)_3 \cdot x\text{H}_2\text{O} (0.05 \text{ M}) + \text{DI water} - 80 \text{ mL} + \text{SnCl}_2 \cdot 2\text{H}_2\text{O} (0 \text{ mol}\%, 2 \text{ mol}\%, 4 \text{ mol}\%)$	NH_4OH added to attain pH-7, Reaction at 100°C for 5 h, dried overnight at 75°C , Calcination: 1000°C for 5 h	$\beta\text{-Ga}_2\text{O}_3$ nano powder	NH_3 gas sensor	[229]
hydrothermal method		$(\text{Al}(\text{NO}_3)_3 \cdot 9\text{H}_2\text{O} - 2.01 \text{ g} + \text{Ga}(\text{NO}_3)_3 \cdot 9\text{H}_2\text{O} - 0.11 \text{ g} + \text{DI water} - 40 \text{ mL}) + \text{methenamine (HMT)} - 3.2 \text{ g}$	Solution stirred ultrasonically for 1 h, Reaction at 180°C for 9 h, Calcination: 550°C for 3 h	$\text{Ga}_2\text{O}_3/\text{Al}_2\text{O}_3$ composite materials	NO_x gas sensing	[230]
		$\text{Ga}(\text{NO}_3)_3 \cdot x\text{H}_2\text{O} (0.1 \text{ M}) + \text{DI water} - 50 \text{ mL} + \text{Al}(\text{NO}_3)_3 \cdot 9\text{H}_2\text{O} (0.02, 0.064, 0.110 \text{ and } 0.210 \text{ g})$	NH_4OH added dropwise till pH-10.34, Reaction at 140°C for 10 h, dried at 70°C for 6 h, Calcination: 1000°C for 6 h in O_2 ambient	$\beta\text{-Ga}_2\text{O}_3$ nanostructures with spindle like morphology to microrod structure	Photocatalyst	[231]

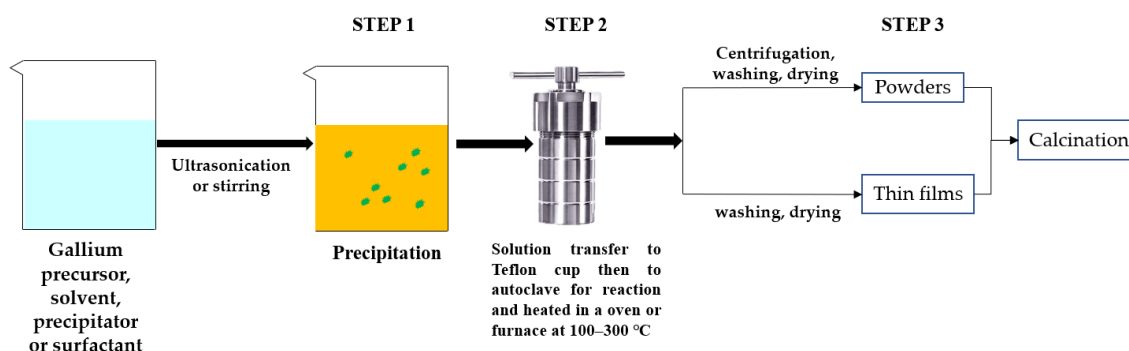


Figure 11. The schematic of hydrothermal preparation of gallium oxide illustrating all steps involved.

J. Zhang et al. [45] synthesized $\beta\text{-Ga}_2\text{O}_3$ nanorods by commercial Ga_2O_3 precursor. Ga_2O_3 was dissolved first in HCl and water or (DEG: water mixture) was added to it. The hydrothermally prepared GaOOH nanorods were calcined at 900°C in air. The pH of the solution affected the morphology of Ga_2O_3 . At pH = 6, the Ga_2O_3 quadrilateral nanorods formed, and at pH = 8, spindle-like nanorod arrays formed. The nanorods have preferential growth direction along c-axis. At pH = 6, the nanorods prepared without and with (DEG: water mixture) had the aspect ratio of 1:7, and 1:15 confirms that the addition of DEG affected the aspect ratio.

S. Krehula et al. [43] used GaCl_3 aqueous solution and TMAH to create $\alpha\text{-GaOOH}$ uniform submicron particles of various shapes (rhombic rods, rhombic prisms, hierarchical structures), as shown in Figure 12. The pH of the solution (pH = 5–9), reaction temperature (60°C or 160°C), and aging time (5–7 days with reaction temperature 60°C) affected the morphology of $\alpha\text{-GaOOH}$. Spindle-shaped particles were formed in acidic conditions at low temperatures, as shown in Figure 12a, and rhombic rods elongated in the c-axis direction were formed at high temperatures, as shown in Figure 12b. In neutral conditions, rhombic prisms were formed, while in base conditions uniform hierarchical $\alpha\text{-GaOOH}$ particles were formed. The $\alpha\text{-GaOOH}$ prepared at 160°C and at pH 7 (as shown in Figure 12d) has less crystallite size compared to acid or base conditions. At neutral conditions, the morphology was rhombic prisms of average length of 600 nm and edge length of (001) rhombic face of approximately 200 nm. When as-synthesized $\alpha\text{-GaOOH}$ calcined at 500°C , the $\alpha\text{-GaOOH}$ particles changed to $\alpha\text{-Ga}_2\text{O}_3$ retaining the morphology but at higher temperatures of

900 °C; samples collapsed severely except the sample prepared hydrothermally at 160 °C, which had retained the shape and particle structure.

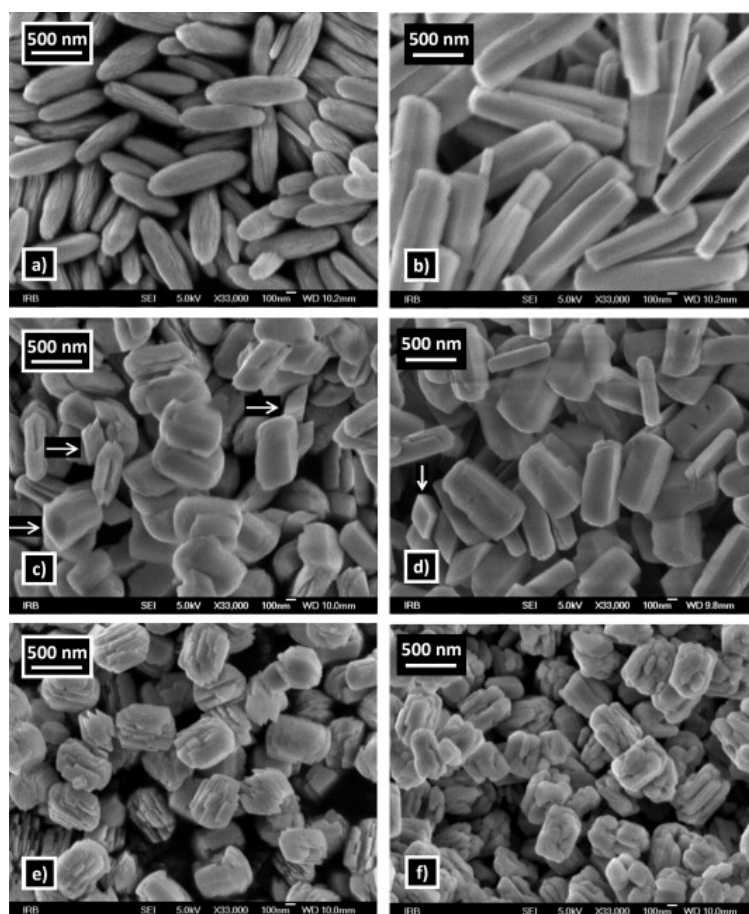


Figure 12. Morphology of α -GaOOH samples (a) A-60, (b) A-160, (c) N-60, (d) N-160, (e) B-60, and (f) B-160. Presence of rhombic faces shown with arrows. Reprinted figure with permission from [43]; copyright (2015) by Elsevier.

J. Liu et al. [202] synthesized mesoporous mixed phase Ga_2O_3 using Ga metal and water precursor solution. The obtained α -GaOOH samples were calcined at 400 °C for 5 h and then calcined subsequently at 600–800 °C for 1.5 h. The XRD and TEM results showed that the Ga_2O_3 sample calcined at 700 °C was porous and had a mixed phase of α - Ga_2O_3 and β - Ga_2O_3 . Both GaOOH and Ga_2O_3 showed rod-like morphology.

Y. Zhao et al. [203] prepared nano to micro sized β - Ga_2O_3 and γ - Ga_2O_3 with or without surfactant (PEO and CTAB) by a low temperature hydrothermal route. The quadrilateral GaOOH rods were obtained from the hydrothermal treatment of gallium hydrate precipitate (i.e., obtained from the solutions prepared by mixing of $\text{Ga}(\text{NO}_3)_3$, NaOH, and HNO_3 in two different procedures) to which the surfactants PEO or CTAB were added. The GaOOH rods prepared from the first procedure (i.e., Ga:OH = 1:3) were changed to β - Ga_2O_3 phase by calcination at 900 °C. In the second procedure (i.e., Ga:OH = 1:5), the γ - Ga_2O_3 rods were directly synthesized after hydrothermal treatment without further need for calcination. The addition of the surfactants PEO or CTAB had no effect on the morphology of hydrothermally synthesized GaOOH rods, but there was a significant difference in pore size, mesoporosity, and pore distribution of β - Ga_2O_3 rods.

In addition, the effect of other surfactants, such as sodium dodecyl benzene sulfonate (SDBS) and sodium acetate (SA) on the morphology of GaOOH was explained by Y. Quan et al. [204]. As shown in Figure 13a, the morphology of α -GaOOH prepared without adding any surfactants was spindle-like particles (i.e., 1.5 μm in length). The morphology

of α -GaOOH prepared with the SDBS surfactant were brush-like particles composed of the nanowires originating from a central knot, as shown in Figure 13b. The nanowire and nanobelt structured growth is related to the anisotropic growth due to selective absorption of the SDBS onto crystallographic facets of a growing crystal [232–234]. The products prepared with SA were agglomerated cuboid-like particles, as shown in Figure 13c.

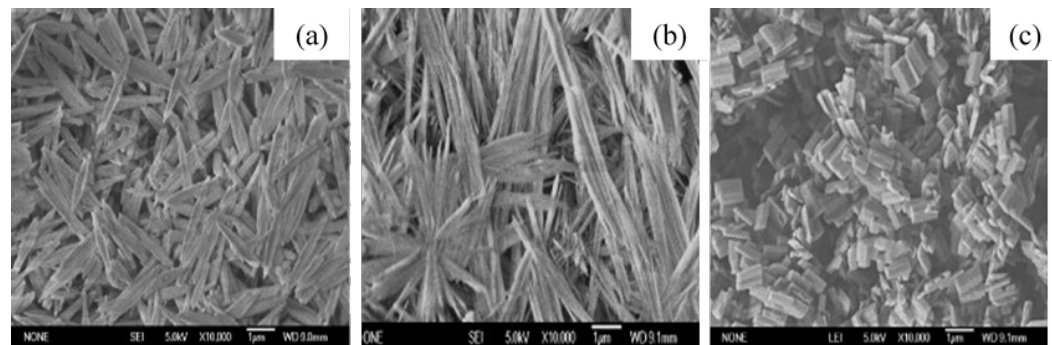


Figure 13. The morphologies of prepared GaOOH (a) without surfactant and with (b) SDBS and (c) SA. Reprinted figure with permission from [204]; copyright (2010) by Elsevier.

FTIR spectral studies confirmed that the GaOOH particles were turned into pure hexagonal phase of α -Ga₂O₃ at 600 °C (i.e., a broad band at 669.8 cm⁻¹ assigned to the valence band vibrations of Ga-O in the lattice formed by GaO₆ octahedra) and monoclinic phase of β -Ga₂O₃ at 900 °C (665.4 cm⁻¹-GaO₆, 753.1 cm⁻¹-GaO₄). The PL studies of β -Ga₂O₃ revealed that it can emit a stable and bright blue light with a peak at 2.84 eV (437 nm) in the blue range [196] due to recombination of an electron on an oxygen vacancy donor and a hole on a gallium vacancy acceptor [235].

J. Wang et al. [205] synthesized the microspheres of β -Ga₂O₃ with hollow interior by calcination of hydrothermally prepared GaOOH microspheres at 1000 °C for 10 h. They proposed a 3-step vesicle template mediated self-assembling process to explain the formation of GaOOH microspheres. In aqueous solutions, the assembly of surfactant molecules having bipolar functional group are more liable to formation of micelles and closed bilayer aggregates, such as vesicles. The bilayer structure separates the aqueous interior from the exterior, providing an interface between the surfactant groups and solution, presenting a specific site for material growth from solution. Vesicles are considered as soft templates that form the hollow spherical structure [236]. As the hydrothermal time prolongs, the nuclei grow anisotropically to nanorods at the surface of templates, resembling the vesicle-template mechanism for the formation of these microspheres.

M. Muruganadham et al. [206] synthesized hollow α -GaOOH microspheres by adding oxalic acid to gallium nitrate in a hydrothermal process. The SEM studies revealed that the reaction temperature had greatly affected the morphologies of as-synthesized GaOOH, shown in Figure 14. At a reaction temperature of 175 °C—flower-like morphology stacked by nano-sheets, at 200 °C—hollow microsphere, at 225 °C—microrods with few microspheres existed. The variation in the concentration of oxalic acid does not affect the morphologies of GaOOH.

The as-synthesized GaOOH was calcined for 3 h at 450 °C to get α -Ga₂O₃. The GaOOH micro flower changed to a rod/plate-like morphology during calcination, while the other GaOOH morphologies retained their shape. The as-synthesized GaOOH prepared without the oxalic acid at hydrothermal temperatures of 175 °C to 225 °C did not show any microsphere morphology. The HR-TEM images of α -Ga₂O₃ synthesized with calcination of GaOOH prepared at a hydrothermal temperature of 200 °C showed that the nanoparticles assembled on the microsphere surface with oriented attachment could grow similar to rods with a very sharp end, as shown in the insert red circle of Figure 15a. Figure 15b shows that these nanoparticles were well-crystalline and defect free.

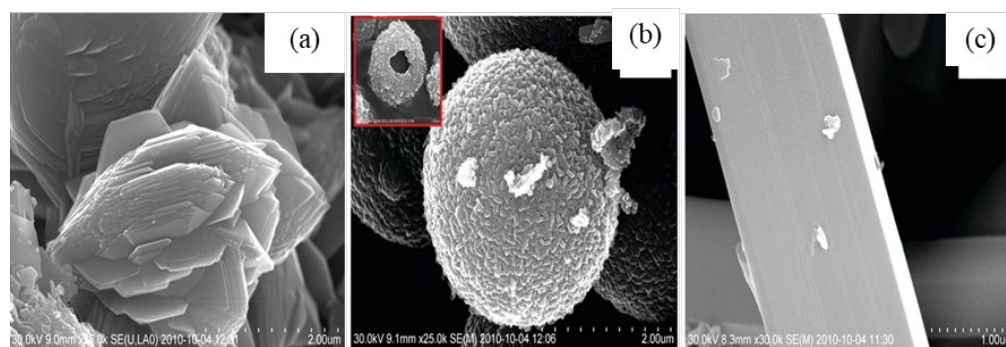


Figure 14. FESEM images of GaOOH morphologies prepared at various hydrothermal temperatures (a) 175 °C (b) 200 °C and (c) 225 °C. Reprinted figure with permission from [206]; copyright (2012) by ACS Publications.

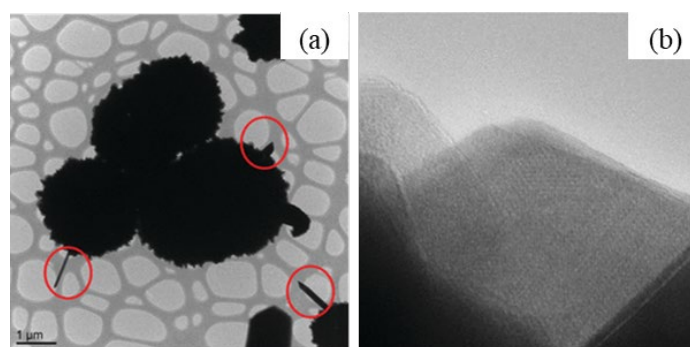


Figure 15. HR-TEM images of α -Ga₂O₃ (a) microspheres (Insert red circle shows shard-end rods with oriented attachment grown on microsphere surface) (b) nanoparticles assembled on the microsphere surface. Reprinted figure with permission from [206]; copyright (2012) by ACS Publications.

D. Li et al. [207] synthesized mesomorphs α -GaOOH hierarchical structures by a liquid-assisted hydrothermal method. The as-synthesized products have the morphology of a hierarchical structure with a diameter of 1 μ m, self-assembled by single crystalline GaOOH nanorods (i.e., diameter 50–100 nm and 0.5 μ m length) that grow along the [00 $\bar{1}$] axis. C₈H₁₆N₂O, also known as [Bmin][OH], had a key role as a soft template in the formation of the α -GaOOH hierarchical structure. As shown in Figure 16, the mesoporous α -Ga₂O₃ hierarchical structure was obtained by calcining the as-synthesized α -GaOOH hierarchical structure for 3 h at 450 °C.

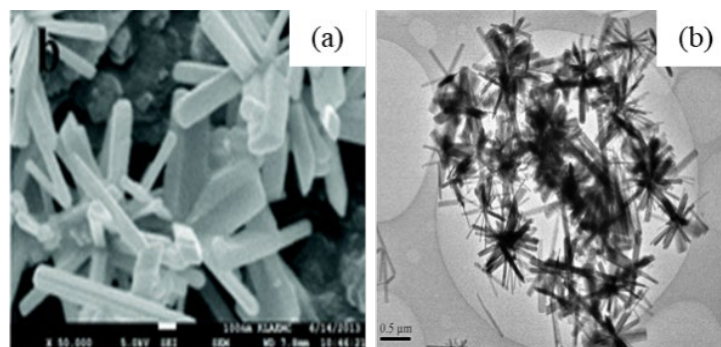


Figure 16. α -Ga₂O₃ hierarchical structure by (a) SEM and (b) TEM. Reprinted figure with permission from [207]; copyright (2013) by the Royal Society of Chemistry.

B. Arul Prakasam et al. [208] used the hydrothermal method to synthesize self-assembled α -GaOOH microrods and micro flowers. The micro rods were prepared by adding biuret to gallium nitrate in the hydrothermal process. The as-synthesized α -GaOOH

micro rods have a length of 2–5 μm . The micro flowers shown in Figure 17a were prepared by using oxalic acid ($\text{C}_2\text{H}_2\text{O}_4$) instead of biuret. The micro flowers were made from nanoribbons and nanorods together. The as-synthesized GaOOH micro flowers had two distinct size variations. The larger were in the size of 2–4 μm whereas the smaller were 500 nm. The smaller lacked nanoribbons. The width of the nanorod in the micro flower was 50 nm. The $\alpha\text{-Ga}_2\text{O}_3$ phase obtained by calcination of $\alpha\text{-GaOOH}$ for 3 h at 450 $^\circ\text{C}$. The TEM image of $\alpha\text{-Ga}_2\text{O}_3$ nanorod/ribbons in microflowers shown in Figure 17d, revealed the porous nature of $\alpha\text{-Ga}_2\text{O}_3$ and the TEM image of microrods shown in Figure 18 revealed the mesoporous nature.

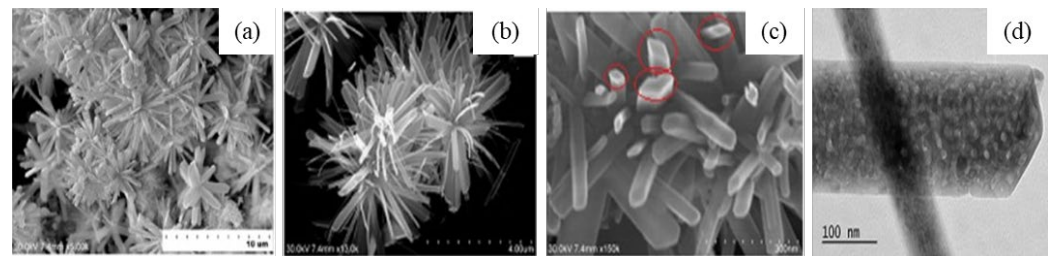


Figure 17. SEM images of (a) micro flowers of $\alpha\text{-Ga}_2\text{O}_3$ prepared with oxalic acid in solution (b) nanoribbons (c) nanorods (d) TEM image of $\alpha\text{-Ga}_2\text{O}_3$ nanorod/ribbon. Reprinted figure with permission from [208]; copyright (2015) by Elsevier.

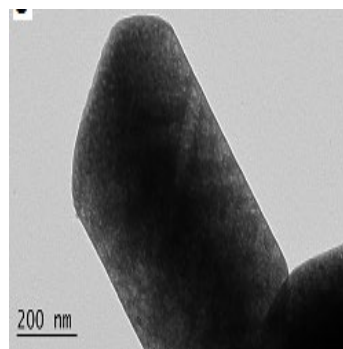
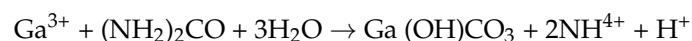


Figure 18. TEM image of $\alpha\text{-Ga}_2\text{O}_3$ micro rods prepared with biuret in solution. Reprinted figure with permission from [208]; copyright (2015) by Elsevier.

B.K. Kang et al. [209] fabricated uniform $\beta\text{-Ga}_2\text{O}_3$ hollow nanostructures by the hydrothermal method using carbon spheres as templates. The carbon nanospheres were prepared using a hydrothermal synthesis of a clear solution made by mixing glucose and distilled water. The carbon colloid solution was prepared by adding carbon nanospheres to a solution of ethanol and distilled water. The synthesis of $\text{Ga}(\text{OH})\text{CO}_3$ core shells around carbon spheres in the urea precipitating solution was described as follows:



FTIR spectra for Ga-coated core-shell structure had a sharp and intense band absorption at 1384 cm^{-1} due to the ν_3 mode of interlamellar $[\text{CO}_3]^{2-}$ ions. This Ga coated core shell nanostructures were calcined between 500–900 $^\circ\text{C}$. The sample calcined at 600 $^\circ\text{C}$ had shown low intensity peaks of $\beta\text{-Ga}_2\text{O}_3$. Calcination at 700 $^\circ\text{C}$, confirmed the well crystallized peaks of $\beta\text{-Ga}_2\text{O}_3$. The calcined $\beta\text{-Ga}_2\text{O}_3$ hollow nanostructures have the diameter of approximately 200–250 nm.

F. Shi et al. [210] synthesized $\beta\text{-Ga}_2\text{O}_3$ nanorods using the urea precipitating solution. They investigated the effect of reaction time on the morphologies and properties of $\beta\text{-Ga}_2\text{O}_3$ nanorods. SEM morphologies of $\beta\text{-Ga}_2\text{O}_3$ samples showed that the products with a short reaction time of 1 h were resulting in amorphous precipitates. In reaction

times of 3 h, these amorphous precipitates were converted into nanorods of uniform shape and size (i.e., length—3 μm , width—300 nm). With the 10 h reaction time, the length and width of nanorods increased to 6 μm and 1 μm , respectively. The morphology was micron-sized flowers composed of many elongated micrometer rods scattered along a common ground. The nanorods were porous and single crystalline as per TEM studies. The Raman spectrum for the sample obtained after 10 h of hydrothermal treatment has the highest intensity and narrowest full width at half-maximum, indicating the highest crystallinity. The photoluminescence spectra show that the three samples' emission peaks appear in the blue-violet region between 375 and 425 nm, which was greatly affected by the hydrothermal time.

L. Cui et al. [211] synthesized ultrafine $\gamma\text{-Ga}_2\text{O}_3$ nanocrystals using urea solution by a microwave hydrothermal method. The hydrothermal products synthesized at 140 $^\circ\text{C}$ for a maintain time of 2 min at low urea concentrations (2 and 2.7 g) were a mixed phase of GaOOH, $\gamma\text{-Ga}_2\text{O}_3$, and at high concentrations (3.4 and 4.1 g) were purely $\gamma\text{-Ga}_2\text{O}_3$. The nanocrystals synthesized with 3.4 g of urea at 140 $^\circ\text{C}$ for 2 min have higher crystallinity, whereas the products of the same amount of urea at 150 $^\circ\text{C}$ were GaOOH. The products prepared with 3 g of urea at 140 $^\circ\text{C}$ for more time (3 min, 4 min) resulted in GaOOH. The optimal hydrothermal conditions to prepare $\gamma\text{-Ga}_2\text{O}_3$ nanocrystals with 3.4 g of urea were 140 $^\circ\text{C}$ for 2 min maintaining time. When these as-synthesized $\gamma\text{-Ga}_2\text{O}_3$ nanocrystals were calcined for 2 h at 300–700 $^\circ\text{C}$, retained their $\gamma\text{-Ga}_2\text{O}_3$ phase up to 500 $^\circ\text{C}$ and changed to $\beta\text{-Ga}_2\text{O}_3$ at 600 $^\circ\text{C}$. The $\gamma\text{-Ga}_2\text{O}_3$ particles were round in shape and had the crystallite size of 5–7 nm with a band gap of 4.61 eV. The PL spectroscopy of calcined $\gamma\text{-Ga}_2\text{O}_3$ particles at 254 nm at room temperature showed that $\gamma\text{-Ga}_2\text{O}_3$ could exhibit violet-blue broadband emission with a peak wavelength of 410 nm, as reported by C.C. Huang et al. [20].

W. Zhao et al. [212] synthesized mesoporous $\beta\text{-Ga}_2\text{O}_3$ nanorods by hydrothermal method using different M.W PEG as a template in urea precipitating solution. PEG was used as a template reagent to synthesize mesoporous nanomaterials [237]. The morphology of obtained GaOOH nanorods was similar to the quadrilateral prisms reported by Zhang et al. [45]. The obtained GaOOH white precipitates were calcined at 800 $^\circ\text{C}$ for 2 h in a furnace to acquire the $\beta\text{-Ga}_2\text{O}_3$ nanorods. Without PEG, the morphologies of produced $\beta\text{-Ga}_2\text{O}_3$ nanorods had no pores, but the nanorods synthesized using 1 mL PEG200 had mesoporous nature, as illustrated in Figure 19b. The band gap of $\beta\text{-Ga}_2\text{O}_3$ mesoporous nanorods was approximately 4.4 eV which is less than 4.7 eV as reported by Hou et al. [238]. New states created due to N doping were just above the valence band for substitutional or interstitial nitrogen, which could narrow down the band gap by combining N 2p and O 2p states.

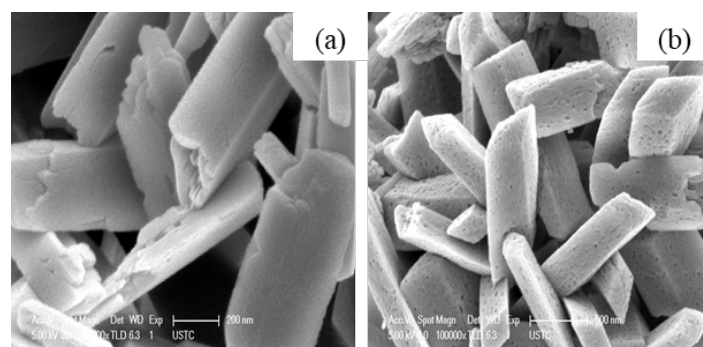
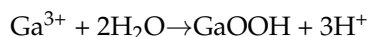


Figure 19. The morphologies of $\beta\text{-Ga}_2\text{O}_3$ prepared (a) without and (b) with 20 mL PEG200. Reprinted figure with permission from [212], Copyright (2011) by Elsevier.

Y. Wang et al. [213] also synthesized $\beta\text{-Ga}_2\text{O}_3$ nanorods by hydrothermal method using PEG in the urea precipitating solution. The as-synthesized products calcined for 10 h at 800 $^\circ\text{C}$. XRD studies showed that the obtained products were highly crystalline $\beta\text{-Ga}_2\text{O}_3$

phase. The TEM images of the β -Ga₂O₃ nanorod revealed that the synthesized nanorods were porous and had diameter of 60 nm with a length of 500 nm.

S. Fujihara et al. [214] synthesized rod-like polycrystalline β -Ga₂O₃ films by hydrothermal method using gallium nitrate aqueous solution. The as-synthesized GaOOH rods were calcined at 700 °C to get the β -Ga₂O₃ phase. The formation of GaOOH precipitate in the solution was governed by the following temperature dependent reaction [239].



Considerable changes in the chemistry of Ga³⁺ ions occur under hydrothermal conditions due to decreased viscosity, decreased dielectric constant and increased ionic product of water [240]. The synthesized GaOOH rods were 3 μ m in length with an aspect ratio of 4. The thermal decomposition of GaOOH into β -Ga₂O₃ increased the aspect ratio to 6–7 on average, even though morphology was retained.

L. S. Reddy et al. [21] also used gallium nitrate aqueous solution to synthesize α -Ga₂O₃ (at 500 °C) and β -Ga₂O₃ nanorods (at 800–1000 °C). The GaOOH prepared at room temperature looks like a cocoon-shaped structure formed by multi-layers of small nanoplates. At 50 °C, these small nanoplates merged and increased the thickness and width of each plate due to Ostwald ripening. At 75 °C, the stacked structure converted into a rod-like structure. At 95 °C, the length of these nanorods increased while the width decreased. TEM studies revealed that the α -Ga₂O₃ and β -Ga₂O₃ nanorods were porous and have length of 3 μ m and width in the range of (280–400 nm).

H. J. Bae et al. [215] also used gallium nitrate aqueous solution to synthesize high aspect ratio β -Ga₂O₃ nanorods (at 1000 °C for 5 h). The spindle-like nanorods of α -GaOOH precipitated with ageing at 60 °C for 1 h while with 6 h ageing time, spindles changed to prism-like nanorods due to face-to-face anisotropic stacking of nanoplates. After the hydrothermal reaction in an autoclave at 140 °C for 10 h, the morphologies of α -GaOOH precipitate changed. High aspect ratio α -GaOOH nanorods obtained with 2 h of ageing and followed by a hydrothermal reaction. After calcination, β -Ga₂O₃ nanorods retained the morphologies of hydrothermally synthesized α -GaOOH.

R. Pilliadugula et al. [216] synthesized α -Ga₂O₃ (at 400–700 °C) and β -Ga₂O₃ nanorods (900, 1000 °C) using gallium nitrate aqueous solution. The band gap of as-synthesized GaOOH and β -Ga₂O₃-1000 °C powders measured by diffuse reflectance spectra was 4.6 eV and 5.51 eV respectively. In their another study [217], they synthesized GaOOH powder samples at various (pH = 5, 7, 9, 11, 14) and calcined at 1000 °C to get β -Ga₂O₃. The Gallium oxide GO-5 and GO-14 samples resulted in less crystallite size (i.e., 30.07 nm and 48.97 nm respectively) due to the existence of compressive strain in those samples. GO-5 sample had rod-like morphology, and cocoon-shaped morphology from pH = 7 to 11, and the GO-14 sample showed hierarchical structure formed from the rod morphology.

F. Shi et al. [218] also synthesized microspheres of β -Ga₂O₃ at different reaction temperatures (40, 80, 120 and 160 °C) using aqueous solution (i.e., at pH = 10). The β -Ga₂O₃ microspheres prepared at hydrothermal temperatures of 120 °C and 160 °C collapsed seriously after calcination. Crystalline particles prepared at higher hydrothermal temperatures can combine with more crystalline water. The evaporation of crystalline water at high temperatures leads to the structural collapse of the β -Ga₂O₃ products. The β -Ga₂O₃ microspheres were 1.2 μ m in length and 300 nm and had dense holes on the surface. The PL spectra of β -Ga₂O₃ microspheres revealed emission peaks between 350 and 450 nm in the blue-violet region.

H. J. Lin [219] et al. synthesized pure β -Ga₂O₃ nanorod arrays (NRAs) a 50 nm thick SnO₂ seed layer sputtered on a 1 μ m SiO₂ insulating layer Si (100) substrate by hydrothermal method. The preferential growth orientation of the GaOOH nanorod arrays was found to be perpendicular to the (111) plane as shown in Figure 20b.

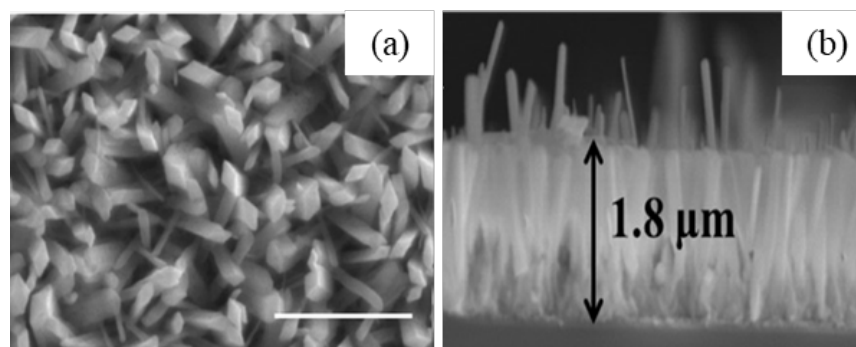


Figure 20. SEM images of (a) GaOOH NRA's on SnO₂/SiO₂/Si substrate (b) side view. Reprinted figure with permission from [219], Copyright (2016) by ACS Publications.

B. Zhang et al. [220] also synthesized β -Ga₂O₃ NRAs similar to the previous study [219]. The XRD of synthesized GaOOH array had a major peak of (111) which shows that preferential growth direction perpendicular to (111) plane. The nanorods had a length of 1.8 μ m and the tips of nanorods were uniform with a diagonal length of 200 nm. The SAED pattern of β -Ga₂O₃ nanorods confirms its growth direction perpendicular to (001) plane.

J. Zhang et al. [221] had grown β -Ga₂O₃ microrod arrays on a Si (100) substrate without any heterogeneous layers using a two-step hydrothermal method. The relatively larger interfacial energy between Si and GaOOH results into lack of nucleation sites, this problem was solved by the incubation of Si substrate in nucleation solution which is crucial to provide sufficient nucleation sites. The morphology of direct synthesized GaOOH microrods without nucleation stage was a one-site nucleated flower-like cluster. Ethanol reduces the surface tension, which reduces the contact angle between the solution cluster and the Si substrate. When the hydrothermal reaction was carried out directly in nucleation solution for a longer time of 12 h at 150 °C, the morphology resulted in spindle-like microrods consisting of an average length of 1.78 μ m and width of 0.42 μ m. The nucleation stage (with ethanol) followed by a growth stage (without ethanol) played a key role to get the array morphology of GaOOH microrods. The possibility of Ga³⁺ adsorption on the Si surface was greatly increased and density distribution sites were created. From the TEM studies, the β -Ga₂O₃ microrods were single crystalline and have a diameter of 768 nm with a length of 2.28 μ m and the morphology of MRAs was shown in Figure 21.

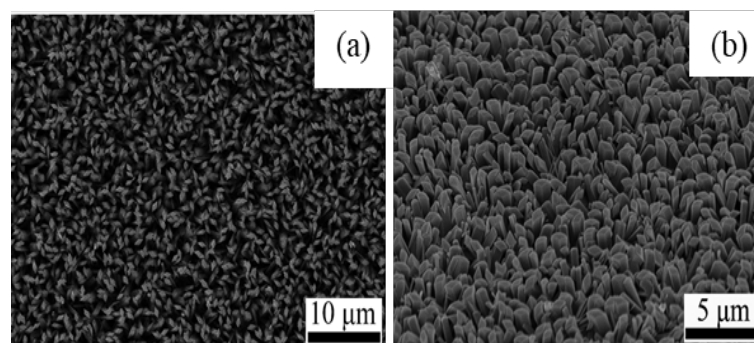


Figure 21. SEM images of (a) β -Ga₂O₃ microrod arrays on Si substrate (b) 45° tilt view. Reprinted figure with permission from [221]; copyright (2018) by the Royal Society of Chemistry.

A. Atilgan et al. [222] also used the same two-stage hydrothermal technique (nucleation and crystal formation) to create β -Ga₂O₃ nanoflakes on P Type-Si substrate. XRD studies showed strong peaks of (002), (111) related to crystalline β -Ga₂O₃ as same as in previous study [221].

D.Y. Guo [223] and C. Wu et al. [224] synthesized α / β -Ga₂O₃ phase junction NRAs hydrothermally on FTO conductive glass. The effect of concentration Ga(NO₃)₃ in solution

and growth time on morphology of GaOOH NRAs was studied [223]. GaOOH NRAs were first annealed at 400 °C for 4 h, then at 700 °C for 20 min to produce α/β -Ga₂O₃ phase junction NRAs shown in Figure 22.

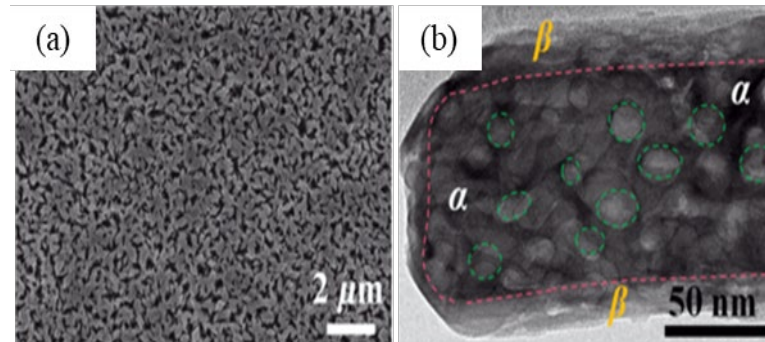


Figure 22. (a) FE-SEM and (b) TEM images of a α/β -Ga₂O₃ nanorod. Reprinted figure with permission from [223]; copyright (2020) by APS Physics.

The tip of nanorods had a rhombus shape and the side length was in the range of 100–500 nm, with an average height of 1.5 μ m. The band gaps of α -Ga₂O₃ and β -Ga₂O₃ were 4.96 eV and 4.66 eV, respectively. The flat potentials calculated according to the extrapolation of Mott-Schottky plots were -1.31 and -0.96 V. The α -Ga₂O₃ was more positive than that of β -Ga₂O₃ with the band offsets of ($\Delta E_c = 0.35$ eV, $\Delta E_v = 0.05$ eV), exhibiting type-II band alignment, which indicates that the photogenerated electron-hole pairs are separated into α -Ga₂O₃ and β -Ga₂O₃ (holes in α -Ga₂O₃ and electrons in β -Ga₂O₃). Based on the band level differences, photogenerated electrons in a conduction band of α -Ga₂O₃ will transfer to the conduction band of β -Ga₂O₃ while photogenerated holes in valence band of β -Ga₂O₃ will transfer to the conduction band of α -Ga₂O₃.

C. He et al. [225] synthesized α -Ga₂O₃ nanorod arrays (NRAs) on SnO₂/FTO substrate by a hydrothermal reaction and post-annealing treatment. S. Wang et al. [226] synthesized β -Ga₂O₃ nanorod arrays hydrothermally on a spin-coated Ga₂O₃ seed-layered FTO conductive glass. The seed layer was created by spinning an ethylene glycol monomethyl ether solution of ethanolamine and gallium isopropoxide at 3000 rpm for 15 s, followed by 30 min of air annealing at 450 °C. The as-prepared GaOOH NRAs were converted into β -Ga₂O₃ NRAs by calcination at 700 °C for 4 h. SEM studies showed that a highly dense flat surface of β -Ga₂O₃ NRAs aligned vertically on the FTO substrate. The nanorods have an average length of 1.287 μ m and the tips of NRAs are in a diamond shape with diagonal lengths in the range of 100–500 nm. The optical band gap of NRAs estimated from UV-vis spectrum data was 4.63 eV.

J. Zhang et al. [227] synthesized a tree-like branched structure with α -Ga₂O₃ covered with γ -Al₂O₃ by a simple two-step hydrothermal method. Initially, they had synthesized GaOOH nanorod arrays hydrothermally on a spin-coated Ga₂O₃ seed layered FTO conductive glass. The GaOOH nanorods grown on (Ga₂O₃/FTO) substrate were divided into two parts. One part was annealed at 500 °C for 4 h to convert into α -Ga₂O₃ while the other was immersed in a solution prepared with different concentrations of Al(NO₃)₃·9H₂O (i.e., 0.005 M, 0.01 M, 0.015 M) and 0.005 M C₆H₁₂N₄ at 180 °C for 12 h as a second step in the hydrothermal process. Then, the sample was annealed at 500 °C for 4 h to obtain Ga₂O₃-Al₂O₃. Figure 23 indicates that the morphology of Ga₂O₃ changed significantly after hydrothermal treatment with 0.015 M aluminum nitrate. HRTEM image of Ga₂O₃ nanorods after the hydrothermal treatment with 0.015 M aluminum nitrate shows that the α -Ga₂O₃ nanorod was completely covered by γ -Al₂O₃; (110) peak from the XRD study indicates that the preferential growth direction of α -Ga₂O₃ on FTO is perpendicular to the (110) crystal plane. The presence of γ -Al₂O₃ may change the surface properties of α -Ga₂O₃, such as dangling bond configuration, surface energy, and surface roughness [241], which promotes the formation of nucleation sites for γ -Al₂O₃, resulting in the eventual emergence

of a tree-like branch structure. The optical band gap of the α -Ga₂O₃ sample measured is 5.0 eV. The band gap of γ -Al₂O₃ is approximately 7.4 eV, and the valence band maximum position is estimated at 3.0 eV in the literature [242].

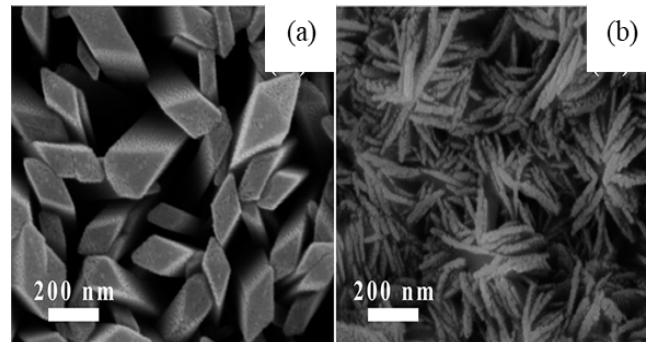


Figure 23. SEM images of pure α -Ga₂O₃ nanorods (a) and tree like branched structure Ga₂O₃ nanorods (b) after treatment with 0.015 M aluminum nitrate. Reprinted figure with permission from [227]; copyright (2021) by Elsevier.

Since the band gap of γ -Al₂O₃ is significantly larger than that of α -Ga₂O₃, UV light with the wavelengths below 300 nm can penetrate the γ -Al₂O₃ and be absorbed by α -Ga₂O₃.

H. Ryou et al. [228] synthesized Sn-doped β -Ga₂O₃ nanostructures via a hydrothermal process. β -Ga₂O₃ nanostructures had Sn concentrations of 0 to 7.3 at.%. At fewer concentrations of Sn, β -Ga₂O₃ nanostructures had a rice-like morphology. As the Sn concentration increased, nanorods began to form and became thicker and longer at high Sn concentrations. The EDS elemental mapping of a nanostructure with 2.2 at.% Sn showed uniform distribution of Sn along β -Ga₂O₃ nanostructure that was beyond the maximum solid solubility of Sn in β -Ga₂O₃ [243]. The radii of Sn⁴⁺ ions (55–81 pm) comparable to that of Ga³⁺ (62 pm) can be substituted at the octahedral sites of β -Ga₂O₃. With an increase in Sn concentration from 0 to 7.3 at.%, the optical band gap of Sn-doped β -Ga₂O₃ nanostructures decreased from 4.8 eV to 4.1 eV.

R. Pilliadugula et al. [229] Sn doped β -Ga₂O₃ by doping Sn into a GaOOH matrix via the hydrothermal method. Sn doped β -Ga₂O₃ showed less weight loss in the thermogravimetric analysis compared to un-doped β -Ga₂O₃, which may be attributed to thermally active Sn molecules in the host material, which certainly increased the thermal stability of samples due to the strong bond nature of Sn compared to Ga [244]. In XRD studies, the 4 mol% Sn doped sample showed (110) and (310) orientations of SnO₂ precipitate may be due to the dopant concentration exceeding the solubility limit of the host material. Sn doped samples showed minor shifts in 2 θ positions of peaks due to the difference in ionic radii of Ga³⁺ and Sn⁴⁺. The 2 mol% Sn-doped sample had a smaller crystallite size of 12.48 nm, a cocoon-shaped morphology, and a band gap of 4.67 eV. The 4 mol%. The Sn-doped sample showed a rod-like morphology resulted from the agglomeration of nanoplate structures with an increased aspect ratio, which showed that Sn doping has altered the morphology of Ga₂O₃ by controlling the Ostwald ripening [245]. The surface area of the 2 mol% Sn doped sample was 12.49 m²g⁻¹, with a pore diameter of 11.64 nm.

J. Wang et al. [230] synthesized Ga₂O₃/Al₂O₃ composite materials by hydrothermal method. The precipitates were calcined for 3 h at 550 °C. In XRD studies of composite, no peak of Ga₂O₃ was observed due to the low concentration of Ga₂O₃ and Ga₂O₃ particles having good dispersibility on the surface of Al₂O₃. TEM studies confirmed the (110) plane of Ga₂O₃. The morphology of Al₂O₃ was a nanosheet structure and Ga₂O₃ was nanorods of 26–28 nm long and 2.6–5 nm wide. The size of Ga₂O₃ in the composite was smaller because the growth of active material grains was inhibited by Al₂O₃ [246]. The slopes of MS plots were negative in the Mott-Schottky measurements which indicates that the Ga₂O₃/Al₂O₃ composite was P-Type.

S. Kim et al. [231] Al-doped β -Ga₂O₃ nanostructures by the hydrothermal method. Al-doped β -Ga₂O₃ nanostructures were obtained with the annealing of GaOOH nanostructures in O₂ ambient at 1000 °C for 6 h. The compressive strain of Al-doped Ga₂O₃ nanostructures was compared with that of thin film β -Ga₂O₃ with the same Al concentration, and it was found that β -Ga₂O₃ nanostructures have a higher compressive strain due to a higher surface energy in nanomaterials [247]. Al doping affected the morphology of β -Ga₂O₃ nanostructures, with an increase in Al content the pH of the solution decreased which in turn changed the morphology of β -Ga₂O₃ nanostructure from spindle-like morphology to microrod structure along with a reduction in length. The BET surface area was unchanged at approximately 7.4–7.6 m²g⁻¹ till the 1.2 Al at.%, then increases at higher Al concentrations attributed to morphology change with Al doping.

4.3. Ga₂O₃ by Chemical Bath Deposition (CBD)

The chemical bath method was a low-temperature process and widely used to synthesize thin films of Ga₂O₃. Morphologies depends on the type of Ga precursor and synthesizing conditions, such as pH of solution, reaction temperature, type of seed layer, and thickness of films, which depends on the deposition time. A schematic of the process is given in Figure 24, and complete literature for the synthesis of Ga₂O₃ by the CBD process is given in Table 5.

Table 5. Chemical bath synthesis of Ga₂O₃.

Method	Substrate/Template	Precursor	Synthesis Conditions	Properties	Applications	Ref.
Chemical bath method		[(((Ga ₂ O ₃ + Dy ₂ O ₃ + Dilute HCl) + DI water) – 500 mL (0.015 mol/L)) + urea (0.025 mol) + OH ⁻ source]—0.5 mol/L	Stirring at RT for 2 h, then to 90 °C in 1 h, films deposition at 90 °C for 4 h, precipitates centrifugated, washed then dried at 90 °C for 24 h. Calcination: 1000 °C for 4 h	At pH-4, submicrospindles. At pH-9, Self-assembled nanoparticle hierarchical microspheres.		[248]
Chemical bath method	Quartz glass, β -Ga ₂ O ₃ /Quartz (70 nm) SnO ₂ , TiO ₂ , MgO coated Quartz glass (Thickness: 70 nm), and FTO glass	(Ga(NO ₃) ₃ ·xH ₂ O + DI water)—0.015 mol/L	Substrates put in solution bottles, sealed and kept in oven at 60 °C for 1–48 h, Calcination: 600–900 °C for 1 h	A small number of heterogeneous nucleation GaOOH precipitates The rod like particles of GaOOH were build-up closely and vertically on substrates		[214]
Chemical bath method	SnO ₂ coated quartz glass	(Ga(NO ₃) ₃ ·nH ₂ O + Eu(CH ₃ COO) ₃ ·4H ₂ O + DI water)—0.015 mol/L + (urea—0.5 mol/L) concentrations of Eu ³⁺ dopants against Ga ³⁺ (1, 3, 5 and 10 at.%)	Substrates put in solution bottles, sealed and kept in oven at 90 °C for 24 h, Calcination: 900 °C for 1 h	β -Ga ₂ O ₃ :Eu ³⁺ oriented along [111] perpendicular to substrate		[249]
Chemical bath method	Glass	Ga(NO ₃) ₃ ·nH ₂ O (0.025 M, 0.05 M, 0.075 M) + HMT (0.5 M) + DI water —1 L	Solution under stirring while reaction at 95 °C for 5 h, films dried at 70 °C for 5 min, Calcination: 400 °C, 500 °C, or 600 °C for 3 h	α -Ga ₂ O ₃ film had high crystallinity at 500 °C	Photodegradation	[250]
Chemical bath method	Si (001)	(Ga(NO ₃) ₃ ·xH ₂ O + ultra-pure water)—(0.015–0.1 M)	Solution stirred at 70 °C for 12 h, Films deposited at 70 °C for 24 h, Films washed and dried under N ₂ , Calcination: 900 °C for 1 h	3 types of rod-like morphologies of β -Ga ₂ O ₃ formed directly on Si		[251]
Chemical bath method	ITO/glass (E-beam deposition) -200 nm	Ga(NO ₃) ₃ ·H ₂ O (A) + HMT (B) + DI water, C _m ratio: ($\frac{A}{B}$ = 0.5, 1, 2)	A seed layer deposition first 10, 20 and 30 min at 95 °C, Deposition at 95 °C for 2 h, Calcination: 400–600 °C for 1 h	α -Ga ₂ O ₃ film of thickness 3.5 μ m, Film's crystallinity is high for C _m = 1:1	pH sensor	[252]

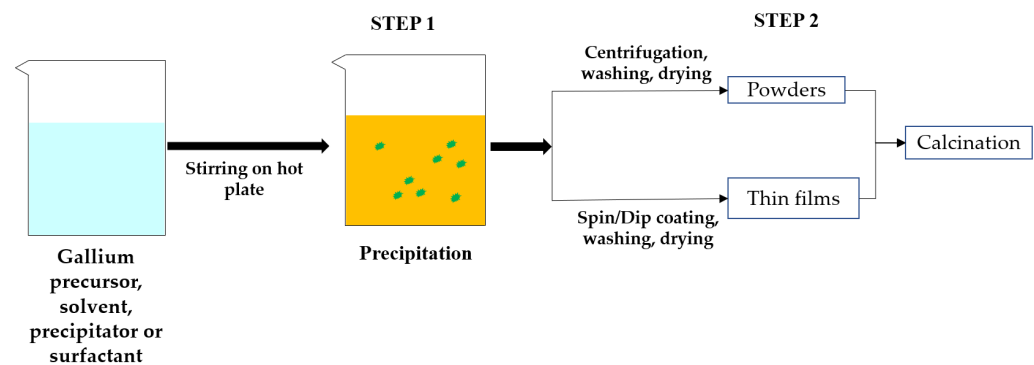


Figure 24. The schematic of chemical bath preparation of gallium oxide illustrating all steps involved.

G. Li et al. [249] used a simple soft-chemical method to create Dy³⁺-doped gallium oxide hydroxides (GaOOH: Dy³⁺) of various morphologies (submicrospindles, submicroellipsoids, and 3D hierarchical microspheres). The morphology of GaOOH: Dy³⁺ changed from submicrospindles to 3D hierarchical microspheres of self-assembled nanoparticles as the pH increased from 4 to 9. The GaOOH: Dy³⁺ submicrospindles prepared at pH 4 had a high aspect ratio with a length 0.85 μm and a width of 0.2 μm. Due to the lowest surface defects, GaOOH: Dy³⁺ phosphors with ellipsoid shapes exhibit the highest emission intensity and Photoluminescence quantum yield (QY) among the four differently shaped samples under UV and electron beam excitation.

S. Fujihara et al. [214] synthesized c-axis oriented GaOOH films, consisting of rod-like particles deposited on various substrates through “chemical solution deposition”. Quartz glass with or without under layers of β-Ga₂O₃, SnO₂, TiO₂, MgO, and FTO coated glass were used as substrates. Heterogeneous nucleation of GaOOH resulted on all of these substrates. The nucleation resulted in a smaller number of precipitates formed on Quartz and β-Ga₂O₃ under layer substrates. This heterogeneous nucleation and deposition of film were enhanced with SnO₂, TiO₂, MgO, and FTO substrates. The rod-like particles of GaOOH were built-up closely and vertically on these substrates. The XRD studies of the GaOOH film deposited on SnO₂ under layer confirmed that the rod-like particles were c-axis oriented perpendicular to the substrate. The XRD of annealed film confirmed that crystallinity of β-Ga₂O₃ increased with annealing temperature. The strong intensity peak (111) of β-Ga₂O₃ suggests that the film is oriented along [111] direction perpendicular to the substrate.

T. Mizunashi et al. [249] used an aqueous chemical bath deposition to synthesize β-Ga₂O₃:Eu³⁺ films. The presence of a relatively strong (111) peak ($2\theta = 35.2^\circ$) suggests that the films are oriented somewhat perpendicular to the substrate along the [111] direction. When 3.0 and 5.0 at.%. Eu³⁺ doped films are exposed to 271 nm UV light, relatively strong line emissions appeared in the wavelength range of 570 to 630 nm. These emissions can be attributed to transitions of the Eu³⁺ ions from the excited 5D₀ level to the ground 7F_J (J' = 0, 1, 2) levels. The strongest emission at 611 nm caused by electric-dipole 5D₀ → 7F₂ transition, indicates the presence of Eu³⁺ at a site with no inversion symmetry in β-Ga₂O₃. A larger Eu³⁺ ion would favor the site with a higher coordination number, but the octahedral site in β-Ga₂O₃ has inversion symmetry. Therefore, it is possible that the octahedral site undergoes distortion by the Eu³⁺ substitution for Ga³⁺ or Eu³⁺ is located in the tetrahedral site. A different spectrum was obtained when films were excited with a shorter wavelength of 254 nm. A broad blue-green emission band appears with a peak wavelength of approximately 451 nm, and emissive defect centers remain in the host of β-Ga₂O₃, demonstrating that the PL spectrum is tunable with different excitation wavelengths and Eu³⁺ concentrations.

C. Y. Yeh et al. [250] synthesized Ga₂O₃ thin films on glass substrates using the chemical bath method and a post-annealing process. As the concentration varied from 0.025 to 0.075 M, the aspect ratio of GaOOH nanorods was 3.23, 3.76, and 5.06, respectively. α-Ga₂O₃ film annealed at 500 °C had high crystallinity with less FWHM in the XRD pattern.

G. Hector et al. [251] synthesized β -Ga₂O₃ microrods by annealing of α -GaOOH microrods that were deposited on Si substrate by chemical bath deposition. As Ga(NO₃)₃·xH₂O concentration varies (i.e., 0.015, 0.025, and 0.05 M), three types of rod-like morphologies formed directly on Si. The 0.015 M concentration resulted in plate-layered rods (length 5 μ m, diameter 1.2 μ m) with a hierarchical structure having a few secondary nucleation at the base. The 0.025 M concentration resulted in round-plate rods (length 7.25 μ m, diameter 2 μ m) with a hierarchical structure having a few secondary nucleations at the base. As the concentration increased more than 0.05 M, the morphology changed to round rods with no secondary nucleation. The aspect ratio of microrods decreased with increasing concentration and reached a maximum value of 3.30 at the highest concentration. The apparent density of rods is much less (1 rod/100 μ m²).

J. L. Chiang et al. [252] synthesized the α -Ga₂O₃ nanorods on a ITO (95% In₂O₃ + 5% SnO₂) coated glass substrate. A 200 nm thick ITO material was coated on a glass substrate by E-beam deposition. The GaOOH nanorods have a length of 500–700 nm. Based on XRD studies, the (111) of GaOOH with less FWHM was resulted for a 1:1 concentration ratio sample. The (104) of α -Ga₂O₃ was the major orientation in all the samples.

4.4. Other Methods

Apart from the above-mentioned methods, the other methods to synthesize Ga₂O₃ materials were solvothermal, forced hydrolysis, reflux condensation, and electrochemical deposition. The complete literature for the synthesis of Ga₂O₃ by these four processes was given in Table 6.

Table 6. Other methods to synthesize Ga₂O₃.

Method	Substrate/Template	Precursor	Synthesis Conditions	Properties	Applications	Ref.
Solvothermal		GaCl ₃ aqueous solution (5.79 mmol) + Eu(NO ₃) ₃ ·6H ₂ O (4.06 × 10 ⁻² mmol) + Tb(NO ₃) ₃ ·6H ₂ O (2.32 × 10 ⁻² mmol) + (ethylene glycol (EG) and water mixture—2:3)	NaOH (1 mol/L) added dropwise till pH = 10, stirred for 2 h, Reaction in autoclave at 200 °C for 4 h, Products separated by centrifugation then washed and dried at 100 °C in vacuum for 4 h.	PL spectra: Un doped β -Ga ₂ O ₃ —Bright blue emission, 0.01% Tb ³⁺ doped—Green, 0.01% Eu ³⁺ doped—Red, Co-doped—White		[253]
Solvothermal	Si	(Ga metal + HF) + (Solvent: mixture of ethylenediamine (En) and water (volume ratio—80:20, 60:40, 50:50, 40:60 and 30:70))	Selected amount of precipitate and solvent then stirred for 1 h, Films deposition in autoclave at 200 °C for 4 h, films washed then dried at 100 °C for 1 h	50:50 sample—2D interconnected nanoflakes structure of flake thickness of 15 nm, 60:40 sample—3D microstructures of order 0.4 μ m diameter		[254]
Solvothermal		(Gallium nitrate—0.65 g) + ethanol—50 mL) + (Sodium acetate—0.6 g + ethanol—50 mL)	Reaction in autoclave at 200 °C for 5h and 10 h, washed with DI water and ethanol then dried in oven at 120 °C for 2 h, No calcination	5 h—GaOOH morphology was incomplete, 10 h—GaOOH semi nanosphere morphology (size: 100–500 nm)		[255]
Solvothermal		(Ga(NO ₃) ₃ ·nH ₂ O—0.5 g + HCl—mL + H ₂ O) + ethylene glycol—4.5 mL, (water to EG ratio-2:3)	pH of solution = 10, Reaction in autoclave at 195 °C for 6 h, Precipitates washed with water and ethanol then dried at 80 °C	Ga ₂ O ₃ nanoparticles size range: 5–10 nm, liquid metal/metal oxide (LM/MO) frameworks with Ga ₂ O ₃ via ultrasonication	Photocatalyst	[256]
Forced hydrolysis		(Ga ₂ (SO ₄) ₃ ·xH ₂ O + Ga(NO ₃) ₃ ·xH ₂ O)—0.01 M + urea—0.1 M + DI water—100 mL, Concentration ratio : R = SO ₄ ²⁻ / NO ₃ ⁻ = 0– ∞	Solution mixture aged in oil bath at 98 ± 1 °C for 2 h, Precipitates separated by centrifugation and washed then freeze dried at -110 °C, Calcination: 500–1000 °C for 1 h	Uniform polycrystalline β -Ga ₂ O ₃ Ns (diameter 200 nm) by calcination at 1000 °C ® R = 0.33		[257]

Table 6. Cont.

Method	Substrate/Template	Precursor	Synthesis Conditions	Properties	Applications	Ref.
Forced hydrolysis		$(\text{Ga}_2(\text{SO}_4)_3 \cdot x\text{H}_2\text{O} + \text{Ga}(\text{NO}_3)_3 \cdot x\text{H}_2\text{O}) - 0.01 \text{ M} + \text{urea} - 0.1 \text{ M} + \text{DI water} - 100 \text{ mL}$, Concentration ratio: $R = \text{SO}_4^{2-} / \text{NO}_3^- = 0.33$	Solution mixture aged in oil bath at $98 \pm 1^\circ\text{C}$ for 2–10 h, Precipitates separated by centrifugation and washed then freeze dried at -110°C , Calcination: 500–1000 $^\circ\text{C}$ for 1 h	Aging time: 2 h—NSs morphology, 10 h—microrods morphology, CL spectra: $\beta\text{-Ga}_2\text{O}_3$ NSs—UV blue emission peak at 375 nm, $\beta\text{-Ga}_2\text{O}_3$ microrods—Strong blue emission peak at 416 nm		[258]
Forced hydrolysis		$(\text{Ga}(\text{NO}_3)_3 \cdot x\text{H}_2\text{O})$ (A—0.03 mol/L) + urea (B—0.18 mol/L) + DI water + DI water + NaNO_3 (C), C_m ratio: $(\frac{A}{B} = \frac{1}{6})$, Ionic strength ratio ($R = \frac{I_A}{I_C} = \infty, 3, 2, 1, 0.5, 0.3, 0.2$)	Hydrolysis at 90°C for 9 h, Products centrifuged and washed, Calcination: 450°C in vacuum	Morphology: At $R = \infty$ —spindle like nanorods having two narrow sides and wide center, $R = 1$ —dumbbell shape with wide sides and narrow center, $R = 0.2$ — Ga_2O_3 broken into fragments		[259]
Reflux condensation		$\text{Ga}(\text{NO}_3)_3 \cdot x\text{H}_2\text{O} - 0.01 \text{ M} + \text{DI water} - 30 \text{ mL} + \text{urea} - 0.1 \text{ M}$	Solution refluxed with continuous stirring at 90°C for 12 h, Precipitate centrifuged and washed then dried at 100°C , Calcination: 500°C and 900°C for 3 h	Self-assembled pattern of $\beta\text{-Ga}_2\text{O}_3$ nanorods	Photocatalyst	[260]
Reflux condensation		$\text{Ga}(\text{NO}_3)_3 \cdot x\text{H}_2\text{O}$ (A)—0.01 M + DI water—30 min + CTAB (B)—stoichiometric amount) C_m ratio: $(\frac{B}{A} = \frac{1}{2}, \frac{5}{1}, \frac{50}{1})$	Solution under stirring for 30 min, solution refluxed with continuous stirring at 90°C for 12 h, precipitate washed and dried at 100°C , Calcination: 900°C for 3 h	At optimal C_m ratio = 5/1, uniform and side to side aligned of $\beta\text{-Ga}_2\text{O}_3$ nanorods (length = 200 nm, diameter = 50 nm)	Photocatalyst	[261]
Electro-deposition	FTO glass	$\text{Ga}_2(\text{SO}_4)_3 - 20 \text{ mM} + \text{H}_2\text{O}_2$ (9.79 M H_2O_2 solution)—0.13 mL	Applied potential: -1.0 to -1.2 , Cathode: FTO glass, Cathode: Pt Deposition time: 2–10 min, Calcination: $500\text{--}600^\circ\text{C}$	At -1.0 and -1.1 V , deposition rate = $30\text{--}60 \text{ nm/min}$, At -1.2 V , deposition rate = $1 \mu\text{m/min}$		[262]
Electro-deposition	Si (100)	$(\text{Ga}_2\text{O}_3$ (0.1 M, 0.5 M, 1.0 M) + $\text{HCl} - 1.5 \text{ mL}$) + DI water—6.5 mL	NH_4OH added to vary the pH = 4–10, deposition time = 2 h, Cathode: Pt wire current density = 0.15 A/cm^2	At pH = 4: High density nanodots at 0.1 M, High density nanorods at 1.0 M		[263]

4.4.1. Solvothermal Method

The solvothermal synthesis process was similar to the hydrothermal process, except that the solution used for synthesis was non-aqueous.

G. Sinha et al. [253] synthesized pure and rare-earth doped Ga_2O_3 nanoparticles by a mixture of ethylene glycol (EG) and water as solvent. Pure and co-doped (0.01% Eu^{3+} and 0.01% Tb^{3+}) Ga_2O_3 nanoparticles were prepared with the same procedure. The PL spectra of nanoparticles showed that a bright white emission was generated due to energy transfer from (Ga_2O_3 -blue) host to rare-earth ions (Eu^{3+} (green) and Tb^{3+} (red) ions). In their other study [254], they directly synthesized 3D micro structured $\beta\text{-Ga}_2\text{O}_3$ films on silicon (Si) substrate via an ethylenediamine (En)-mediated solvothermal process. The XRD analysis of films revealed that the films were well-crystalline in nature and a phase transformation occurred from $\alpha\text{-GaOOH}$ to $\beta\text{-Ga}_2\text{O}_3$ at a volume ratio of 60:40. For a given volume ratio of En to water, increasing the reaction time results in increased crystallinity. The TEM image showed that the morphology of a 40:60 sample with a reaction time of 2 h was composed of nanowires that are attached along their edges due to plastic deformation. With increasing the reaction time to 4 h, the morphology changed to branched nanoflakes of 8 nm width. The FESEM image of a 50:50 sample showed that the morphology becomes a 2D interconnected nanoflakes structure with a flake thickness of 15 nm, and these structures were assembled together to form 3D microstructures of an order of 0.4 μm in diameter for a 60:40 sample. The diameter becomes 2 μm with flakes thickness of 20–60 nm for an 80:20 sample. It was assumed that the En molecules interact with the hydroxyl groups of the

precursors, allowing for complete dehydration of gallium hydroxide and the formation of β -Ga₂O₃ at lower temperatures of 200 °C

M. Muruganandham et al. [255] synthesized mesoporous α -GaOOH by the solvothermal method using anhydrous ethanol as a solvent. The GaOOH particles synthesized at 200 °C for 10 h had semi-nanosphere morphology with a dense core and thin shell-like structures. The particle size ranged from 100 to 500 nm and had a high surface area of 193 m²g⁻¹. The GaOOH, prepared at less than 200 °C, did not yield semi-nanosphere morphology. The GaOOH prepared at a 5 h reaction time showed that the formation of morphology was incomplete. The semi-nanosphere morphology GaOOH had not obtained using water or water-ethanol as solvent. The high pressures resulted from the low boiling point of ethanol (78 °C) in the solvothermal process could be the reason for the different morphologies from the corresponding hydrothermal process.

W. Zhang et al. [256] synthesized γ -Ga₂O₃ nanoparticles by the solvothermal method and incorporated them into liquid metal/metal oxide (LM/MO) frameworks.

4.4.2. Forced Hydrolysis Method

B. K. Kang et al. [257] synthesized monodispersed β -Ga₂O₃ nanospheres via morphology-controlled gallium precursors using a simple and reproducible urea-based forced hydrolysis method, followed by thermal calcination processes. The rod-like structures of GaOOH (i.e., diameter 200–400 nm and length of 1.5–2 μ m) were obtained at a concentration ratio of 0 (i.e., without sulfate ions). The crystalline rods of GaOOH were obtained due to aggregation of Ga(OH)₄ aqueous solution, which was a precursor obtained by decomposition of urea at 80 °C and releasing uniform OH⁻ ions into a Ga(OH)₃ solution. As the concentration ratio R increased to 0.33, a monodispersed spherical amorphous precursor Ga₄(OH)₁₀SO₄ formed in the solution due to the higher affinity of SO₄²⁻ ions than NO₃⁻. These spheres were agglomerated as R increased. The as-synthesized amorphous NSs were converted to uniform polycrystalline β -Ga₂O₃ NSs (diameter 200 nm) by annealing at 1000 °C. In their following study [258], they investigated the effect of ageing time on the morphology of gallium precursors, while fixing the concentration ratio R = 0.33 and varying the ageing time from 2–10 h. After increasing the reaction time to 6 h, the α -GaOOH microrods structure with preferential growth direction [001] was dominant. The size of α -GaOOH microrods increased as the size of NSs decreased, indicating that the NSs were dissolved in the solution and aggregated on the surfaces of the microrods. When the reaction time was increased to 10 h, the NSs vanished and the morphology changed completely to well-crystalline α -GaOOH microrods with branched rods growing along {001} planes of primary rods. This growth mechanism is illustrated in Figure 25.

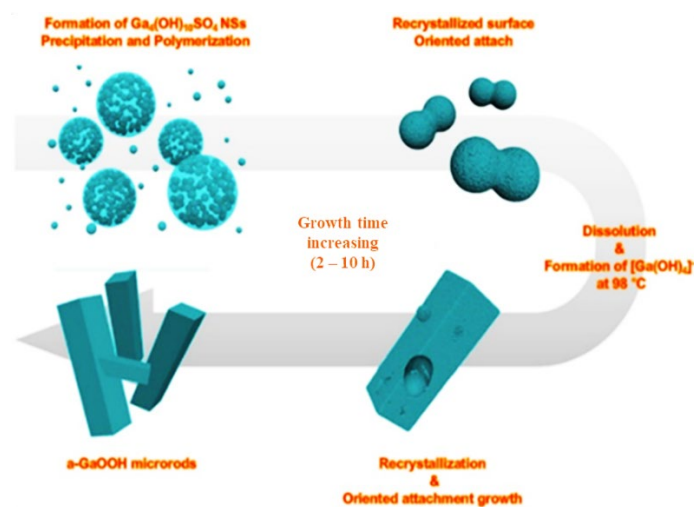


Figure 25. Illustration of time dependent growth of gallium precursors. Reprinted figure with permission from [258]; copyright (2016) by Elsevier.

E. Huang et al. [259] synthesized GaOOH via forced hydrolysis from a solution containing different ionic ratios of $\text{Ga}(\text{NO}_3)_3 \cdot x\text{H}_2\text{O}$ and sodium nitrate (NaNO_3).

$$\text{Ionic-strength}(I) = \frac{1}{2} \sum_B m_B z_B^2 \text{ where } m_B \text{ is the molality of ion B in the solution,}$$

z_B is its charge number (Negative for anions and positive for cations).

When R increased from 0.2 to 1, the relative crystallinity of $\alpha\text{-Ga}_2\text{O}_3$ increased distinctly and decreased with a further increase in R-value. The optimized ionic strength was 1, which has high crystallinity. The morphology of Ga_2O_3 without the addition of NaNO_3 ($R = \infty$), was spindle-like nanorods having two narrow sides and a wide center. With $R = 3$ and 2, Ga_2O_3 appeared as nanorods of uniform width. At $R = 1$, Ga_2O_3 crystals transform into a dumbbell shape with wide sides and a narrow center. From $R = 0.5$ to 0.3, nanorods exfoliated to nanoplates, strips and fragments. This morphology-controlled synthesis was illustrated in Figure 26. At $R = 0.2$, Ga_2O_3 was fully broken into fragments.

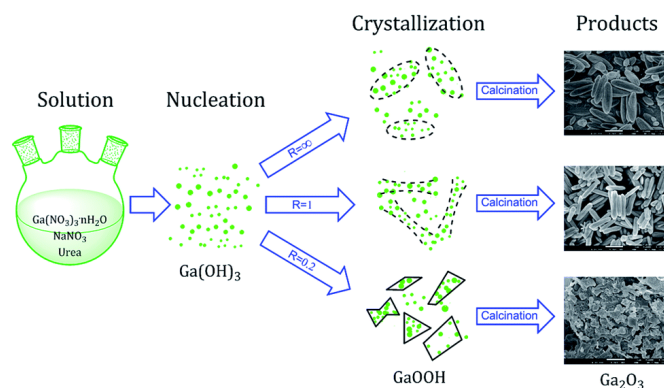


Figure 26. Schematic of morphology-controlled synthesis of Ga_2O_3 . Reprinted figure with permission from [259]; copyright (2017) by the Royal Society of Chemistry.

The highest absorption with an edge up to 360 nm is obtained with the $\alpha\text{-Ga}_2\text{O}_3$ sample at $R = 1$, indicating its highest defect site concentration in the UV-vis spectra of $\alpha\text{-Ga}_2\text{O}_3$ synthesized at different R values. The highest photoluminescence intensity (One signal at 460 nm-blue, the other is at 600 nm-orange) is obtained for $\alpha\text{-Ga}_2\text{O}_3$ prepared at $R = 1$, which is several times greater than the commercial $\alpha\text{-Ga}_2\text{O}_3$ sample. Surface areas of Ga_2O_3 samples synthesized at different R values are measured to be in the range of $30\text{--}50 \text{ m}^2\text{g}^{-1}$, which is significantly higher than the surface area of commercial Ga_2O_3 ($15 \text{ m}^2\text{g}^{-1}$).

4.4.3. Reflux Condensation Method

K. Girija et al. [260] synthesized self-assembled novel floral $\beta\text{-Ga}_2\text{O}_3$ nanorods via the reflux condensation method. The precipitate calcined for 3 h at 500°C was changed to crystalline $\alpha\text{-Ga}_2\text{O}_3$ and calcined at 900°C was changed to crystalline $\beta\text{-Ga}_2\text{O}_3$. Figure 27a shows the SEM image of a self-assembled pattern (i.e., size $\sim 1 \mu\text{m}$) made by individual nanorods of size 100 nm. As shown in Figure 27b, the TEM image suggests the single crystalline nature of nanorods. From the UV-vis diffuse reflectance spectrum, it was found that the absorption edge was at 280 nm and the band gap E_g of $\beta\text{-Ga}_2\text{O}_3$ nanorods was found to be 4.59 eV. When excited at 254 nm, the PL spectrum showed a strong UV luminescence peak centered at 360 nm and a small peak at 302 nm.

In their other study [261], they prepared single crystalline $\beta\text{-Ga}_2\text{O}_3$ nanorods by a facile reflux condensation method using $\text{Ga}(\text{NO}_3)_3 \cdot n\text{H}_2\text{O}$ and anionic surfactant CTAB as starting materials. Time-dependent experiments were carried out to investigate the morphology evaluation. The initial molar concentration of surfactant was as follows: metal ions were set at 5:1, and the reaction time ranged from 3 to 12 h. At 3 h, an agglomerated

rod-like structure was observed, as seen in Figure 28a; when the reaction time was increased to 6 h, nanorods were formed, indicating the presence of Ostwald ripening. The nanorods were non-uniform and randomly aligned, as seen Figure 28b. When the reaction time is increased to 12 h, the nanorods become uniform and side by side aligned, as seen in Figure 28c. The nanorods measured 200 nm in length and 50 nm in diameter.

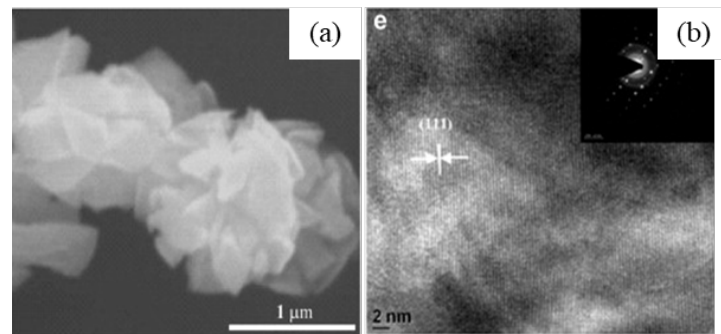


Figure 27. (a) SEM image of Floral β - Ga_2O_3 (b) TEM image of nanorod inside the floral structure of β - Ga_2O_3 . Reprinted figure with permission from [260], copyright (2013) by Elsevier.

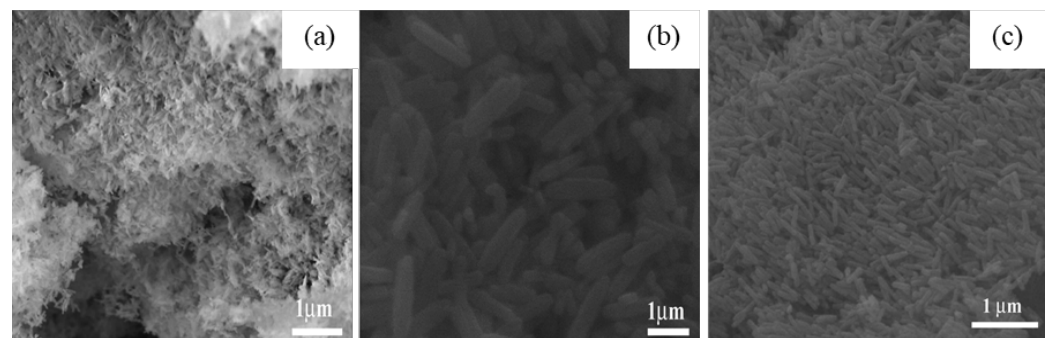


Figure 28. Time dependent morphology evolution of β - Ga_2O_3 . (a) agglomerated rod-like structure (b) Randomly aligned non-uniform nanorods (c) Side-by-side aligned uniform nanorods. Reprinted figure with permission from [261]; copyright (2014) by Elsevier.

To study the effect of CTAB concentration on morphology, three concentration ratios (CTAB: metal ion—1:2, 5:1 and 50:1) were chosen while the reaction time was fixed at 12 h. At low concentrations of CTAB (ratio—1:2), the morphology was composed of agglomerated nanoparticles as shown in Figure 29a. At higher concentrations (ratio: 5:1), the morphology became side-to-side aligned nanorods and at very high concentrations the nanorods lost uniformity and alignment, as shown in Figure 29c.

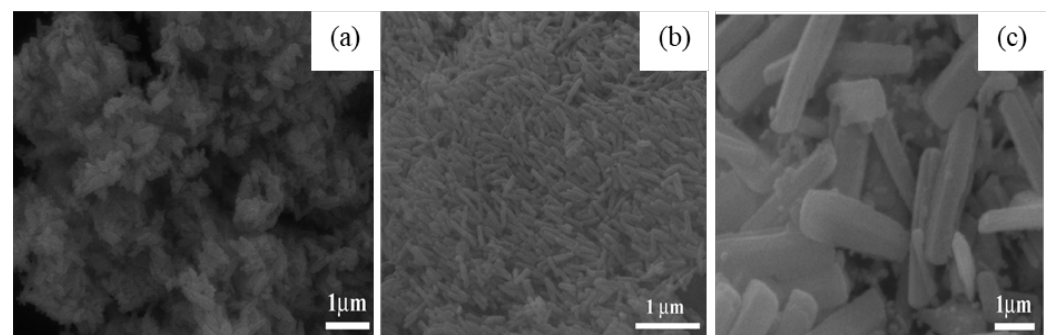
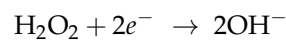


Figure 29. Concentration dependent morphology evolution of β - Ga_2O_3 . (a) agglomerated nanoparticles (b) Side-by-side aligned uniform nanorods (c) Randomly aligned non-uniform nanorods. Reprinted figure with permission from [261]; copyright (2014) by Elsevier.

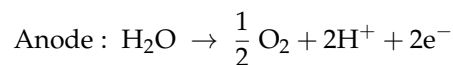
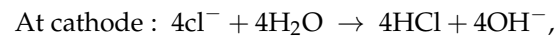
4.4.4. Electrochemical Deposition

J. J. M. Vequizo et al. [262] synthesized α -Ga₂O₃ thin film on FTO substrate by electrochemical deposition and a post-annealing process. A cyclic voltammetry (CV) experiment was performed to determine the best-applied voltage for various deposition times (2–10 min). A cathodic peak appeared at approximately -0.68 V, but no significant thickness was achieved for potentials greater than -1.0 V, indicating that a large over-potential is required to activate the reaction on the FTO substrate. As a result, the chosen potential values are greater than or equal to -1.0 V. A higher amount of H₂O₂ in solution results in a high non-uniformity and roughness of films due to the bubbling effect or due to oxygen gas generation during reaction. Hence, an optimal quantity (i.e., 0.13 mL) of H₂O₂ was chosen based on uniform thickness of the film. A deposition voltage of -1.1 V for a deposition time of 3 min and a deposition voltage of -1.0 V for a deposition time of 3–10 min produced a crack-free surface of films.



When a cathodic voltage was applied, the OH[−] ions generated near the cathode by electrochemical reduction could be used to generate GaOOH at room temperature via the reaction of OH[−] with Ga³⁺. The films converted into α -Ga₂O₃ at the temperature range of 500–600 °C.

N. M. Ghazali et al. [263] synthesized β -Ga₂O₃ nanostructures on Si (100) substrate. The possible reactions during the electrochemical deposition process are summarized below:



At a low molarity of 0.1 M, nanodot-like structures of Ga₂O₃ were deposited on Si substrate in both acidic and alkaline conditions. The dot structure has a high density in the acidic medium, as shown in Figure 30a. When molarity was increased to 0.5 and 1.0 M, nanorods started to form at a low pH level while a nanodot structure without or with less density of nanorods was obtained at a high pH level. High-density nanorods of a length of 200–500 nm and a length of 2–4 μm were obtained at pH 4, as shown in Figure 30b.

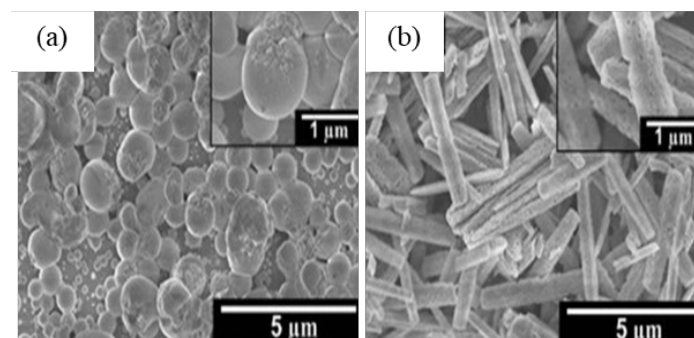


Figure 30. (a) Nanodot structure of Ga₂O₃ prepared at molarity of 0.1 M (b) Nanorod structure of Ga₂O₃ prepared molarity of 1.0 M in acidic medium (i.e., at pH 4). Reprinted figure with permission from [263]; copyright (2014) by Springer.

5. Applications

In this chapter, the applications of Ga₂O₃ will be discussed from various solution processes (including hydrothermal, sol-gel, chemical bath deposition, etc.). This chapter will contain deep ultraviolet photodetector, gas sensors, pH sensors, thin film transistors, and other applications. By optimizing the process parameters, Ga₂O₃ material synthesized

through various solution processes can be applied to the sensors for better response characteristics. However, due to the influence of human operation, environment, or other factors, the reliability and repeatability of sensors fabricated by the solution process are not as stable as the vacuum process.

5.1. Deep-Ultraviolet Photodetectors (PD)

In the past, ultraviolet (UV) detection was applied in many fields, such as civilian, military, and scientific research. The ultraviolet spectral region is defined as $\lambda = 400\text{--}10\text{ nm}$. According to ref. [264], it is usually divided into the following subdivisions: near ultraviolet (NUV, 400–300 nm), mid ultraviolet (MUV, 300–200 nm), far ultraviolet (FUV, 200–122 nm), and extreme ultraviolet (EUV, 122–10 nm). According to another definition, it can also be divided into four regions namely ultraviolet A, B, C, and vacuum ultraviolet (VUV). A detailed description can be found in reference [265].

It is generally recognized that sunlight is the most important source of natural ultraviolet. It can emit ultraviolet radiation of various wavelengths. However, all UVC radiation from the sunlight is absorbed by the diatomic oxygen or ozone in the atmosphere [265]. In addition, vacuum UV is almost absorbed by molecular oxygen in the air. Therefore, a range of 200–280 nm of the UV region is called “solar blind”, which means that it can be detected without interference from solar radiation. In addition, the characteristics of solar-blind detectors are that they possess a cutoff wavelength below 280 nm because they only respond to ultraviolet radiation with wavelengths shorter than the solar radiation that can penetrate Earth’s atmosphere. If they are exposed to normal outdoor lighting, they will not produce a measurable signal. Solar-blind DUV-PDs with excellent thermal stability and reliability have been widely applied in many fields, such as ozone monitored, flame detection, communications, military defense, biochemistry, ultraviolet leakage, and other fields [266].

There are many scientific reports and much literature that mention solar-blind photodetectors made from wide-band gap semiconductors [266–279], such as GaN [266], ZnO [267], ZnS [268], ZnSe [269], SiC [270,271], AlN [272], diamond [273,274], BN [275], Ga₂O₃ [276,277,279], Al_xGa_{1-x}N [278], and so on. These materials are also applied to high-power and high-temperature applications [280,281] because they have high breakdown field strength. However, to meet the standard for solar-blind photodetectors with a cut-off wavelength of less than 280 nm, it is necessary for alloy engineering to adjust the band gap to 4.42 eV, and Ga₂O₃ has the potential as a solar-blind DUV detector. Because the monoclinic structure of β -Ga₂O₃ has a wide band gap of 4.4–4.8 eV [276] (corresponding to a wavelength of 258–280 nm) and its solar-blind sensitivity is expected to cover most solar blind ultraviolet regions [265]. Besides the thin film type, Ga₂O₃ nanorods and nanowires also synthesized through hydrothermal [274], sol-gel [275], chemical bath deposition [250–252], and so on. This section will discuss photodetectors made from solution-based gallium oxide (Ga₂O₃).

Y. Kokubun et al. [181] synthesized the β -Ga₂O₃ on sapphire substrate by the sol-gel method at 600–1200 °C different annealing temperatures. They analyzed the effect of annealing temperature on the spectral responses of photoconductive detectors. As shown in Figure 31, the top surface of film is exposed to radiation. It can be seen that the Ga₂O₃ films annealed at 600 and 800 °C, the photocurrent peak appears at 250 nm, and no photocurrent was observed greater than 280 nm. As the annealing temperature exceeds 900 °C, the photocurrent peak shifted to shorter wavelengths. The maximum value of responsivity $\sim 8 \times 10^{-5}$ A/W occurred for the film annealing at 1000 °C. It indicated that the β -Ga₂O₃ films prepared by the sol-gel process have potential applications as solar-blind photodetectors.

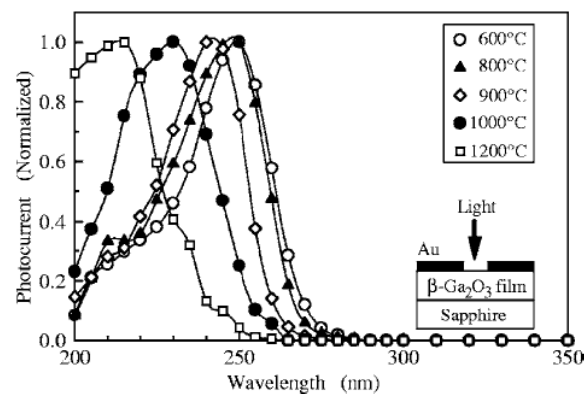


Figure 31. Photocurrent characteristics responses of β -Ga₂O₃ photodetectors prepared at 600–900 °C temperatures. Reprinted figure with permission from [181]; copyright (2007) by the American Institute of Physics.

In addition, Rikiya Suzuki et al. [178] prepared epitaxial grown β -Ga₂O₃ thin films on a (100) β -Ga₂O₃ substrate using the sol-gel method. They prepared photodiodes with and without the sol-gel prepared β -Ga₂O₃ cap layer. It is revealed that the Au/ β -Ga₂O₃/ β -Ga₂O₃ structure of photodiodes possesses a lower leakage current. From the dark I-V curves of photodiodes, it was revealed that the cap layer was highly resistive having a resistivity of $10^6 \Omega\text{-cm}$. The photodiode with a cap layer operated at a 5.4 V turn-on voltage, which was more than that of the photodiode without a cap layer (i.e., 1.6 V). Figure 32 shows the spectral response of Ga₂O₃ photodiodes with and without a cap layer at reverse and forward biases of 3 V. Under the forward bias of 3 V, a maximum responsivity of 4.3 A/W was noted for the β -Ga₂O₃ photodiode with a cap layer.

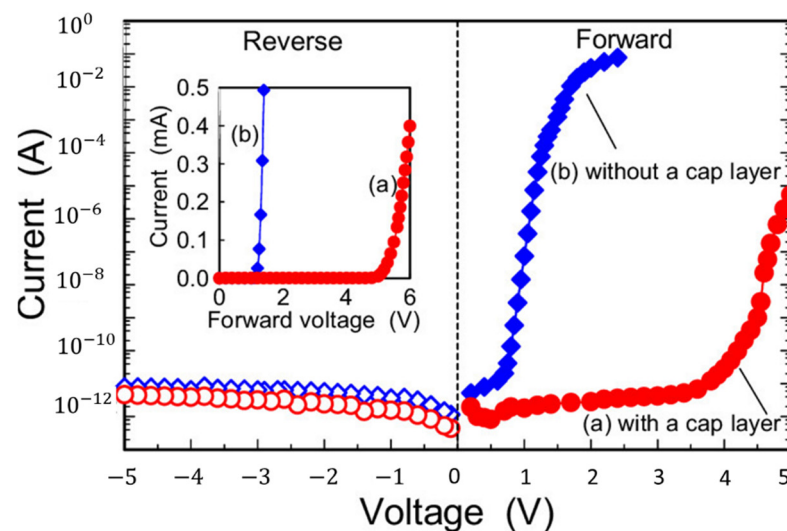


Figure 32. (Color online) Spectral response of Ga₂O₃ photodiodes with and without a cap layer at reverse and forward biases of 3 V. The inset shows the incident light intensity dependence of the photocurrent at (a) forward and (b) reverse biases of 3 V under illumination with 250 nm light. Reprinted figure with permission from [182]; copyright (2011) by the American Institute of Physics.

H. Shen et al. [188] and M. Yu et al. [189] have also used the sol-gel technique to synthesize Ga₂O₃ thin films on sapphire substrate. The (I-V) test and time-resolved photo response of the photo-detector fabricated with β -Ga₂O₃ thin film annealed at 700 °C, showing a high $I_{\text{photo}}/I_{\text{dark}}$ ratio of 18.34 along with the fast rise time of 0.10 s and decay time of 0.10 s [188]. In addition, the photodetector made by α/β polycrystalline Ga₂O₃ thin films had a low-dark current (18 pA), an $I_{\text{photo}}/I_{\text{dark}}$ ratio of 1664, detectivity(D^*) of

5.41×10^{11} Jones, and a fast photo-response speed (that is rise time(t_r) of 0.03 s/0.23 s and decay time(t_d) of 0.04s/0.41s) [189].

In addition, many research reports mentioned Ga_2O_3 nanorod arrays (NRAs) synthesized by a hydrothermal reaction [224–226]. S. Wang et al. [226] synthesized $\beta\text{-Ga}_2\text{O}_3$ nanorod arrays (NRAs) hydrothermally on a spin-coated Ga_2O_3 seed layered FTO conductive glass. A Ti/Au electrode was formed on $\beta\text{-Ga}_2\text{O}_3$ NRAs to build a solar-blind DUV photodetector. Figure 33 shows the device structure and the current-voltage characteristic curves. The PD was operated without and with light (i.e., 254 nm illumination) at various light densities. When the PD operated at 0 bias and 1.2 mW/cm² light intensity, it exhibited an $I_{\text{photo}}/I_{\text{dark}}$ ratio of 9.14, a responsivity of 10.80 mA/W, an external quantum efficiency (EQE) of 5.27×10^{-3} , and rise/decay times of 0.64 s/0.38 s, respectively. In addition, the photo response switching behaviors at various bias voltages were also observed. Obviously, the I_{dark} and I_{photo} increased with increasing the bias voltage from 0 V to 1.5 V. At 1.5 V, a I_{photo} of 17.60 pA was observed, which is approximately 11 times that at 0 V. Furthermore, the I_{photo} increased linearly with the electric field due to more electron-hole pair separation and more transport excite of photogenerated electron-hole pairs, resulting in a higher photocurrent [226]. These experimental results indicate that the PD possesses high conversion efficiency and low power consumption properties. It has the potential for use in solar-blind photodetector application.

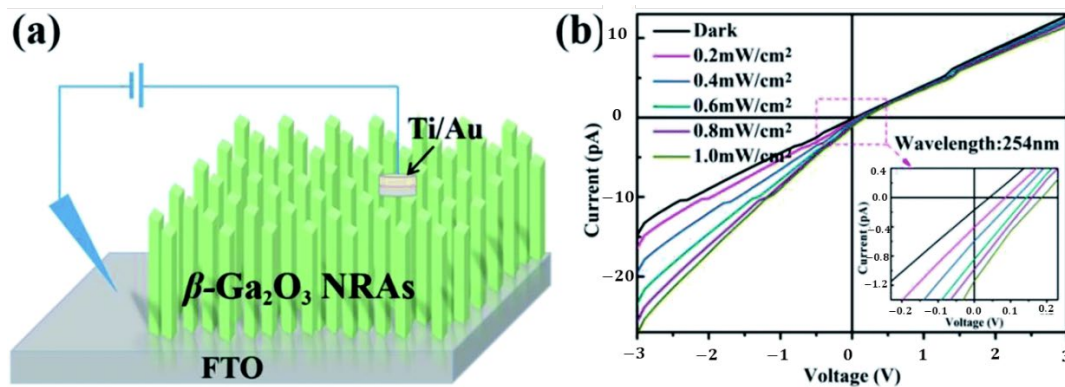


Figure 33. (a) The $\beta\text{-Ga}_2\text{O}_3$ NRAs solar-blind photodetector. (b) Current–voltage curves of the device in the dark and under 254 nm illumination with various light power densities. Reprinted figure with permission from [226]; copyright (2019) by the Royal Society of Chemistry.

Furthermore, $\alpha\text{-Ga}_2\text{O}_3$ nanorod arrays (NRAs) via a hydrothermal process and thermal annealing was proposed by C. He et al. [225], where the p-type Cu_2O microspheres were grown on the $\alpha\text{-Ga}_2\text{O}_3$ nanorod arrays. The $\alpha\text{-Ga}_2\text{O}_3/\text{Cu}_2\text{O}$ heterojunction was a p–n junction structure that could effectively enhance the photo-induced carriers and the range of light detection. The PEC-type photodetectors fabricated with an $\alpha\text{-Ga}_2\text{O}_3/\text{Cu}_2\text{O}$ p–n junction structure displayed distinguishable spectral signatures with opposite photocurrent responses when illuminated by UV light at 254 and 365 nm. It has the potential to be developed into a self-powered PD capable of distinguishing between ultraviolet and visible bands. When exposed to 254–365 nm UV light, the PD showed a superior responsivity region of 0.42–0.57 mA/W. The PD showed a fast response of ($t_r \sim 103$ ms) under 365 nm UV light. C. He et al. provide a solution to distinguish different illumination bands through a photodetector with heterojunction.

D.Y. Guo [223] synthesized $\alpha/\beta\text{-Ga}_2\text{O}_3$ phase junction NRAs hydrothermally on FTO conductive glass. To make a solid-state type photodetector a simple structure of Ti/Au electrode was deposited on the top of NRAs. The solar blind solid-state photodetector showed rectifying characteristics as observed in I–V curve. Photogenerated carriers cannot be separated effectively in this structure of device because only the upper end of nanorods will be in contact with electrode while the perimeter of nanorods will be contactless. Under 0 V bias and at the constant light intensity, the photocurrent from $\alpha/\beta\text{-Ga}_2\text{O}_3$ photoelectrochemical-

type photo detector was more than that of α -Ga₂O₃ photo detector. Both α -Ga₂O₃ and α/β -Ga₂O₃ phase junction photo detectors had showed linear relationship between the photo current and light intensity.

A solar-blind photodetector of vertical α/β -Ga₂O₃ phase junction NRAs was built on FTO glass via the hydrothermal method that has been proposed by C. Wu et al. [224]. To get a large detection range, a $0.5 \times 1 \text{ cm}^2$ mono layered graphene-silver nanowire (Ag NWs of 150 nm in diameter and a length several tens of hundreds of μm) hybrid film was synthesized on top of NRAs. A $0.005 \times 0.05 \text{ cm}^2$ circular Ag electrode was deposited on the corner of hybrid film for point connection for external circuit. The experimental results found that the current of the photodetector in the dark was 1.72 nA under 254 nm UV light with 0 V, and the current increased to 211.07 nA when the light intensity was $3000 \mu\text{W}/\text{cm}^2$. The responsivity decreases from 0.26 mA/W to 0.14 mA/W due to the increased probability of electron-hole pair recombination at higher light intensities. The maximum value of detectivity (D) of 2.8×10^9 jones ($\text{cm Hz}^{1/2} \text{ W}^{-1}$) occurred at a light intensity of $100 \mu\text{W}/\text{cm}^2$ and decreased with an increase in light intensity. In addition, the photodetector showed a high $I_{\text{photo}}/I_{\text{dark}}$ ratio of 2.1×10^2 and a rise time of 0.54 s. Furthermore, the photodetector operated in a vacuum environment ($\sim 1 \text{ Pa}$), the $I_{\text{photo}}/I_{\text{dark}}$ ratio of 3.48 was lower than that of atmospheric conditions, and it also exhibited a faster response of rise time of 0.16 s.

A. Atilgan et al. [222] mentioned that β -Ga₂O₃ nanoflakes were synthesized on p-Si substrate by the hydrothermal process. The back electrode covering the entire back side of the device was made by screen-printing of Ag paste. An Ag/Al/Au ohmic electrode was fabricated on the $1 \times 1 \text{ cm}^2$ selective area of β -Ga₂O₃ nanoflakes to make a heterojunction β -Ga₂O₃/p-Si photodiode. The nanoflake structure has a main advantage, it can effectively improve the electron-hole pairs upon UV illumination at the junction region. The device showed rectifying characteristics due to heterojunction and had a high rectifying ratio of 1387 at $\pm 10 \text{ V}$. The photoresponsivity is significantly different at 0 V (0.16 mA/W) and at 10 V (17.1 A/W). It can be shown that the β -Ga₂O₃ nanoflakes have potential in self-powered photodiode applications.

Recently, the tree-like branched structure of α -Ga₂O₃ covered with γ -Al₂O₃ was synthesized using a simple two-step hydrothermal method by J. Zhang et al. [227]. They succeeded in fabricating a PEC self-powered UV detector. The responsivity of the UV detector made with a Ga₂O₃-Al₂O₃ heterojunction and α -Ga₂O₃ nanorods was 0.174 mA/W and 0.129 mA/W, respectively. In addition, the high $I_{\text{photo}}/I_{\text{dark}}$ ratio of 51.3 and 14.5 was also determined, respectively. The experimental results found that the detection performance could be improved.

According to the above-mentioned, Ga₂O₃ materials by the solution process have *successfully* been applied as a photodetector. It possesses a low-cost process, low power consumption abilities, a high $I_{\text{photo}}/I_{\text{dark}}$ ratio, a fast response, and so on. Its superior properties can be a promising candidate for solar-blind photodetection applications.

5.2. Gas Sensors

Resistive gas sensors have been under development for a long time. Ga₂O₃ is one of the most important materials for high temperature gas sensing due to its high melting point ($\sim 1800 \text{ }^\circ\text{C}$). S. J. Pearton et al. [7] reported on the processing and devices of gallium oxide material in 2018, which mentioned the application of gallium oxide gas sensors. In general, polycrystalline Ga₂O₃ materials can be used either as a gas sensor for sensing oxygen ($T \geq 900 \text{ }^\circ\text{C}$) or reducing gases ($T < 900 \text{ }^\circ\text{C}$), depending on the working temperature. In addition, the advantage of monoclinic β -Ga₂O₃ is very stable, which can be easily prepared with annealing temperatures at 800–900 $^\circ\text{C}$.

For high-temperature applications, such as internal combustion engines or furnace installations, Ga₂O₃ gas sensors have been used to monitor the composition of exhaust gases. Ga₂O₃ thin films possess the ability to sense oxygen by the resistivity of changes with the concentration of oxygen. S. J. Pearton et al. have summarized the gas sensor applications,

operating temperature range, and detection ranges for Ga₂O₃ gas sensors [7]. According to many reports, the Ga₂O₃ thin films for gas sensors can be deposited by sputtering, reactive thermal evaporation, the sol-gel process, the synthesis method, and others. In this review, we have organized and discussed the preparation and gas applications of gallium oxide materials synthesized through solution processes.

Y. Li et al. [179] have investigated the gas sensing performance of sol-gel prepared Ga₂O₃ thin film doped with Ce, Sb, W, and Zn. It was concluded that the sensor doped with Zn showed O₂ gas sensing performance at operating temperatures below 420 °C. Ce doped sensor showed a lower response yet a fast response time (40 s). The W doped sensor showed a higher response with O₂ gas and the Sb doped sensor showed the least response compared to other sensors. In addition, the experimental results show the dynamic response of the doped Ga₂O₃ gas sensor when exposed to a pure N₂ baseline and a 1000 ppm oxygen pulse at 500 °C. Furthermore, they also found that the sensor doped with Sb possesses a higher base resistance than the sensors doped with other materials. Meanwhile, sensors doped with Ce, W, and Zn possess a base resistance of similar orders of magnitude. In summary, the sensors made by Ga₂O₃ films doped with Sb, Ce, W, and Zn possess a superior response, stability, and repeatability when operated at various temperatures [179].

A. Trinchi et al. [282] mentioned that a kind of Schottky diode (Pt/Ga₂O₃/SiC) can be characterized for H₂ sensing applications. Its sensing characteristic is correlated with the operating temperature. In this research, Schottky diodes possess more superior advantages than the pure Ga₂O₃ thin film of conductometric sensors. Among these, the Ga₂O₃ materials were prepared by the sol-gel process and deposited onto the transducers by spin-coating. The sensor placed under cycling the ambient from synthetic air (SA) to 1% H₂ in SA air, produces repeatable changes at fixed forward bias. When the sensors were operated above 500 °C, they possessed a fast response time. In addition, the response of the sensors show good stability in H₂ sensing applications with a 210 mV drop in bias voltage for 1% H₂ [282].

M. R Mohammadi et al. [187] mentioned that the mesoporous TiO₂ and Ga₂O₃ thin films was synthesized on quartz and alumina substrate transducers with various Ti:Ga atomic ratios using the particulate sol-gel method. Due to a high specific surface area, the gas sensor made with binary oxide (atomic ratio Ti/Ga = 1) annealed at 600 °C had shown the highest response toward the gases of CO and NO₂.

H. J. Lin et al. [219] deposited a 50 nm-thick SnO₂ seed layer on a 1 μm SiO₂ insulating layer Si (100) substrate by sputtering. Afterwards, they synthesized pure β-Ga₂O₃ nanorod arrays (NRAs) by the hydrothermal method on the Sn/SiO₂ substrate. Pt nanoparticles by dip-coating or LSFO (La_{0.8}Sr_{0.2}FeO₃) nanoparticles by sputtering were decorated on this β-Ga₂O₃ nanorod array, done post-annealing to improve crystallinity. This structure was used as a gas sensor for CO gas detection at various concentrations (20, 50, 80, and 100 ppm in N₂ balance). Those two kinds of sensors showed same performance at low concentrations. LSFO (La_{0.8}Sr_{0.2}FeO₃) nanoparticles coated β-Ga₂O₃ nanorod arrays showed a fast response over that coated by Pt nanoparticles.

R. Pilliadugula et al. [216] synthesized β-Ga₂O₃ nanorods by the hydrothermal method. These calcined nanorods were mixed with ethanol at room temperature and drop casted onto a silver coated glass substrate, with a period of wait until the ethanol was completely dry. Afterwards, the films were sintered at 100 °C to improve adhesion. The morphology of calcined nanorods revealed that the porosity was increased with an increase in calcination temperature. These pores are favorable for CO₂ gas sensing. In addition, surface area studies were obtained from BET—N₂ adsorption-desorption studies. The BET surface areas for GaOOH and β-Ga₂O₃—1000 °C samples were 6.7494 m²g⁻¹ and 6.1034 m²g⁻¹. These two samples were compared for CO₂ gas sensing. It was seen that the sensing response was linear for both samples. For all concentrations of CO₂, the β-Ga₂O₃—1000 °C had shown a higher sensing response and better repeatability when compared to GaOOH due to its low band gap and high pore density.

Furthermore, R. Pilliadugula et al. [217] fabricated β-Ga₂O₃ sensing films over IDE pattern printed on glass substrates by drop casting. The films were dried at 80 °C for 10 h

to allow complete evaporation of the NMP solvent from the film, and heated at 250 °C for 2 h to improve adhesion. Of all the samples, GO—5 and GO—14 have a high aspect ratio of 5.88 and 6.89. The excess alkaline environment facilitated the directional attachment of these high aspect ratio particles. It was found that the GO—5 sample has highest band gap of 4.75 eV; the band gap was influenced with pH value and decreased with increasing pH. Meanwhile, the GO—14 sample had the lowest band gap of 4.61 eV, and its high aspect ratio nanoparticles morphology showed an enhanced sensing response at all NH₃ vapor concentrations between 25–200 ppm, except at the concentrations below 100 ppm. In addition, R. Pilliadugula et al. [229] also proposed Sn doped β -Ga₂O₃ by doping Sn into GaOOH matrix by the hydrothermal method. The experimental results found that the 2 mol% Sn doped sample had a superior surface area and exhibited an enhanced sensing response property at 25 ppm to 200 ppm of NH₃.

In addition, J. Wang et al. [230] synthesized Ga₂O₃/Al₂O₃ composite materials by the hydrothermal method. The composite showed a 58.2% response to NO_x—100 ppm at room temperature, which was 6.8 times higher than pure Ga₂O₃ prepared under the same hydrothermal conditions.

B. Zhang et al. [220] has successfully synthesized β -Ga₂O₃ NRAs. The La based LSCO perovskite oxide (La_{0.8}Sr_{0.2}CoO₃) catalytical nanoparticles of two different thicknesses (3 and 8 nm) were deposited on β -Ga₂O₃ NRAs by RF magnetron sputtering. This structure was subjected to NO₂ gas sensing at various concentrations at 800 °C. By LSCO nanoparticle decoration, the NO₂ response of β -Ga₂O₃ NRAs can be enhanced by more than 500%. After incorporation of LSCO, it has a faster response time but a longer recovery time. For high-temperature detection, the device possesses 0.1625 ppm⁻¹ at 800 °C, the sensitivity is very high. Because the LSCO/ β -Ga₂O₃ structure is a p–n heterojunction, the charge carrier diffusion occurs at the junction, amplifying the overall n-type response of the heterojunction. Therefore, the LSCO nanoparticles facilitate detection of NO₂ gas and improve its response speed at high temperatures.

According to the above-mentioned gas sensor applications of Ga₂O₃, by modifying the solution process parameters, Ga₂O₃ can be used to detect O₂, H₂, CO, CO₂, NO_x, NO₂, NH₃, and so on. Ga₂O₃ materials were synthesized using a solution process and have a low temperature process, fast response, high potential for use in gas sensing, and superior sensing characteristics.

5.3. pH Sensors

In the past decade, public health problems caused by irregular lifestyles and unhealthy diets have become a global concern. One of the established health biomarkers is a stable pH, which is associated with all tissues of the body. Hence, biosensors for pH sensing have attracted significant interest in the scientific community [283]. Therefore, several metal-oxide materials have been used as sensing materials, widely applied to pH or biochemical sensors. SnO₂, ZnO, RuO₂, WO₃, ITO, TiO₂, ZrO₂, Ta₂O₅, HfO₂, and Ga₂O₃ have been widely used as sensing materials for pH sensors [252,283,284]. Among oxide materials, Ga₂O₃ is a wide band gap material that has attracted considerable attention in very recent years because it possesses many advantages (including nontoxicity, thermal stability, and excellent chemical and ideal biocompatible properties) [252,283,284]. In addition to being widely used in photodetectors, gas sensors, photocatalysis, and photodegradation, gallium oxide is also used in pH sensors. According to ref. [284], micro- and nanostructured sensing materials have a superior ratio of surface/volume. These materials were applied in electrochemical and biomedical sciences, and other scientific areas, possessing good potential applications. They can enhance sensing response and select ability and catalytic activity; thus, as a pH sensing material, it possesses many applications in life, the medical industry, environmental pollution, and so on because of its fast response, wide testing range, high sensitivity, and easy and low-cost fabrication.

J. L. Chiang et al. [252] proposed synthesized α -Ga₂O₃ nanorods on an ITO-coated glass substrate via the chemical bath deposition (CBD) method. The top view of the SEM micrograph of the Ga₂O₃ nanorods was shown in Figure 34.

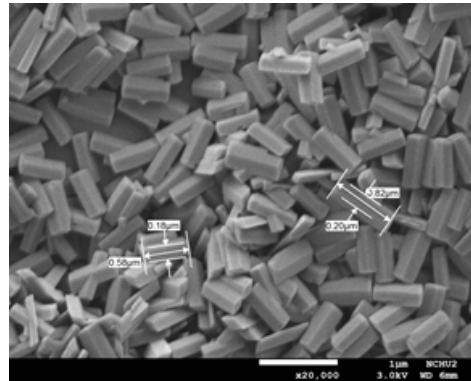


Figure 34. The as-deposited surface morphology of GaOOH nanorods, with the same molar concentration ratios ($\text{Ga}(\text{NO}_3)_3/\text{HMT} = 1$).

The α -Ga₂O₃/ITO sensing structure based on EGFET had been used to detect pH response behavior in the different (pH = 1, 3, 5, 7, 9, and 11) buffer solutions. Figure 35a shows the current–voltage (I–V) characteristic curves of the α -Ga₂O₃ nanorod pH-EGFET. The pH-EGFET based on α -Ga₂O₃ nanorod had superior sensitivity of 51.59–64.29 mV/pH. In addition, the linear response is shown in Figure 35b. The results found that α -Ga₂O₃ nanorod pH sensor possesses superior linear response with linearity close to 1. In addition, the long-term response of the α -Ga₂O₃ nanorod pH sensor was also monitored. At room temperature, a drift phenomenon was measured via an instrument amplifier circuit (AD620). The Output voltage of α -Ga₂O₃ pH sensor was monitored and recorded in pH 4, 7, and 10 buffer solutions over 6 h; the lower drift rate (~2.75 mV/h) in pH 7 buffer solution was observed.

In addition, the pH sensing properties of metal oxide materials (including α -Ga₂O₃ nanorods) have been discussed and proposed in ref. [252]. The linearity and pH sensitivity of the α -Ga₂O₃/ITO sensing structure was found to be superior, with a stable signal output and a fast response. The α -Ga₂O₃ nanorods are suitable for a wide range of pH detecting environments (pH 1–11). When compared to other materials, the Ga₂O₃ nanorod materials have a superior pH Nernst response. Chiang et al. provides a simple process of Ga₂O₃ nanomaterials for the low-temperature and low-cost fabrication of highly sensitive and disposable pH sensors.

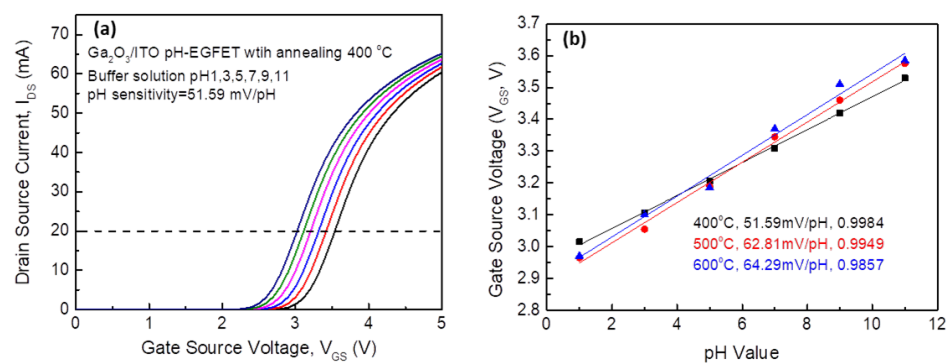


Figure 35. A family of current–voltage characteristic curves and pH response of α -Ga₂O₃ pH-EGFET, (a) annealed 400 °C, immersed in pH 1, 3, 5, 7, 9, 11 buffer solutions, respectively. (b) pH sensitivity and linearity of α -Ga₂O₃ pH-EGFETs were annealed at 400–600 °C. Reprinted figure with permission from [252]; copyright (2022) by Elsevier.

5.4. Photocatalytic and Photodegradation Applications

Recently, metal oxide materials, such as TiO_2 , ZnO , and Ga_2O_3 have been considered promising for photocatalytic and photodegradation applications [21,285–288] because the metal oxides possess excellent physical and chemical properties. The photocatalytic processes include two steps: one is hydroxyl radical oxidation ($\cdot\text{OH}$) and the other is photo-generated holes oxidation [289,290]. The generation of ($\cdot\text{OH}$) from water is controlled by the relative humidity of water molecules or gases on the photocatalyst surface. The oxidative properties of photo generated holes were greatly influenced by the structural and electronic properties of photocatalysts. Ga_2O_3 has a wide band gap (4.2–4.9 eV), and it has many superior properties that are important for semiconductor devices and industrial applications.

In addition, according to the above-mentioned (Section 5.1), the Ga_2O_3 materials synthesized solution process possesses a superior response to UV and DUV. In terms of photocatalytic and photodegradation applications, also the Ga_2O_3 materials have been investigated and published, as described below.

L. S. Reddy et al. [21] synthesized the $\beta\text{-Ga}_2\text{O}_3$ nanorods by a simple hydrothermal synthesis. The photocatalytic activity of samples explained in Figure 36a shows the photodegradation absorbance spectra of Rhodamine B (RhB) solution under UV light irradiation.

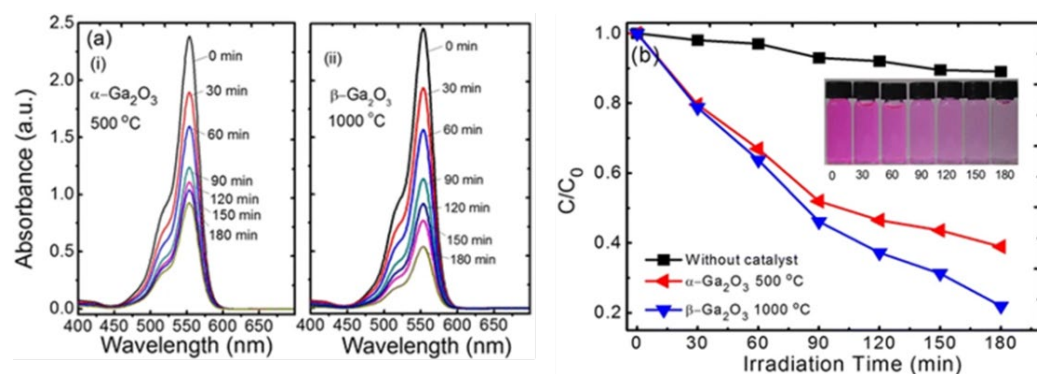


Figure 36. Photocatalytic activity of $\alpha\text{-Ga}_2\text{O}_3$ and $\beta\text{-Ga}_2\text{O}_3$ under different UV irradiation. (a) (i) absorbance spectra of $\alpha\text{-Ga}_2\text{O}_3$ and (ii) absorbance spectra of $\beta\text{-Ga}_2\text{O}_3$ nanorods. (b) Calculated constant reaction rate of the photodegradation of RhB solution (C/C_0) as a function of UV irradiation time for $\alpha\text{-Ga}_2\text{O}_3$ and $\beta\text{-Ga}_2\text{O}_3$ nanorods. Reprinted figure with permission from [21]; copyright (2015) by Springer.

The maximum absorbance of RhB under UV light at different absorption times occurred at 553 nm for $\alpha\text{-Ga}_2\text{O}_3$ and $\beta\text{-Ga}_2\text{O}_3$. The photographic of the RhB solution for various UV irradiation times (i.e., 0–180 min) is also shown in the inset of Figure 36b. Under the UV irradiation time of 180 min, photodegradation efficiency reached 62% for $\alpha\text{-Ga}_2\text{O}_3$ and 79% for $\beta\text{-Ga}_2\text{O}_3$, as shown in Figure 36b.

W. Zhao et al. [212] synthesized mesoporous $\beta\text{-Ga}_2\text{O}_3$ nanorods by the hydrothermal method using different M.W PEG as a template. These $\beta\text{-Ga}_2\text{O}_3$ mesoporous nanorods were used as a catalyst for photodegradation of toluene. It was concluded from their studies that mesoporous $\beta\text{-Ga}_2\text{O}_3$ nanorods synthesized with PEG (M.W 200, 20 mL) can obtain the largest BET surface area ($29\text{ m}^2\text{g}^{-1}$) and mean pore size (30 nm). The percentage of dangerous pollutant intermediates (i.e., acetaldehyde and formaldehyde) produced from the photocatalytic activity of $\beta\text{-Ga}_2\text{O}_3$ was less than that of conventional TiO_2 as a catalyst.

M. Muruganadham et al. [206] reported the synthesis of $\alpha\text{-Ga}_2\text{O}_3$ microspheres by using hydrothermal method. The experimental results of photocatalytic degradation showed that $\alpha\text{-Ga}_2\text{O}_3$ microsphere is more efficient than conventional TiO_2 for AO7 dye degradation and Cr (VI) reduction.

D. Li et al. [207] synthesized mesomorphs α -Ga₂O₃ hierarchical structures by using a liquid assisted hydrothermal method. The synthesized α -Ga₂O₃ subjected to photodegradation of RhB dye under UV irradiation. The absorption spectra of RhB solution under different irradiation times showed that the maximum peak occurred at 556 nm. Under exposure via UV light irradiation for 100 min, the as-prepared α -Ga₂O₃ removed 95% of the dye, while the commercial α -Ga₂O₃ only removed 60%. The greater absorption ability mostly attributed to the larger surface area of BET (35.94 m²g⁻¹).

Y. Wang et al. [213] synthesized β -Ga₂O₃ nanorods by the hydrothermal method. The photocatalytic activity of β -Ga₂O₃ nanorods was studied by photocatalytic degradation of dye under solar irradiation. According to experimental results, with simulated solar irradiation after 4 h, the degradation rate of methylene blue (MB) and methyl orange (MO) reaches 95.32% and 90.47%, respectively.

J. Liu et al. [202] synthesized mesoporous mixed phase Ga₂O₃ by calcination of α -GaOOH at 600–700 °C. The absorption spectrum of photocatalytic degradation of Ga₂O₃-700 °C sample in metronidazole solution has a characteristic peak at 320 nm, and the peak decreases with the increase of irradiation time, indicating that the degradation of metronidazole solution occurred. Under UV irradiation for 120 min, 95.55% of the solution was removed with mesoporous mixed phase Ga₂O₃ photocatalyst

L. Cui et al. [211] synthesized ultrafine γ -Ga₂O₃ nanocrystals by the microwave hydrothermal method. Under UV light illumination, with RhB the calcined nanocrystals of γ -Ga₂O₃ exhibited a higher photodegradation efficiency of 90.7% compared to that of 68.2% for the as-synthesized pure γ -Ga₂O₃ nanocrystals.

H. Ryou et al. [228] synthesized Sn-doped β -Ga₂O₃ nanostructures via the hydrothermal process. The intrinsic β -Ga₂O₃ nanostructure had 40% photocatalytic activity and increased to 90% with 0.7 at.% Sn, decreased with an increase in Sn concentration, and flattened out from 3.2 to 7.3 at.% Sn, which was attributed to absorption capacity limitation due to a reduction in quantum yield because of absorption or scattering of UVC light by precipitated Sn oxides. The presence of SnO or SnO₂ degraded the photocatalytic performance of β -Ga₂O₃ nanostructure.

S. Kim et al. [231] synthesized Al-doped β -Ga₂O₃ nanostructures by the hydrothermal method. These Al doped β -Ga₂O₃ nanostructures were used as a photocatalyst for degradation of the MB solution. The redox potential and surface area of β -Ga₂O₃ nanostructures increased with the increase in Al content but the defects increased. The defects in photocatalyst can either enhance or degrade the activity by acting as carrier separation and recombination sites [291]. With the increase in the Al content from (0.6–3.2 at.%) in β -Ga₂O₃ nanostructures the photocatalytic activity decreased. This decrease in photocatalytic activity was attributed to the generation of deep trap levels due to GB/crystallography [77,292] and oxygen vacancy defects [293].

In addition, the Ga₂O₃ materials were synthesized on glass substrates using the chemical bath method with a post-annealing process by C. Y. Yeh et al. [250]. A 0.075 M concentration of Ga(NO₃)₃ was used to prepare GaOOH materials. Afterwards, α -Ga₂O₃ materials were obtained by annealing, and the MB in the solution was photodegraded by more than 90% after 5 h of UV irradiation.

W. Zhang et al. [256] incorporated the solvent-synthesized γ -Ga₂O₃ nanoparticles into liquid metal/metal oxide (LM/MO) frameworks. The quantity of LM/MO frameworks (5.45 mg) and Ga₂O₃ nanoparticles (3.3, 16.3, and 32.6 μ L) were regulated to yield 0.2, 1, and 2 wt.%, respectively. The photocatalytic performance of LM/MO frameworks incorporating γ -Ga₂O₃ nanoparticles was evaluated using Congo red (CR) as the indicator dye, in which the LM/MO framework incorporating 1 wt.% Ga₂O₃ nanoparticles was demonstrated to exhibit the best photocatalytic efficiency of $\sim 100\% \text{ h}^{-1}$ within 1 h with high reusability.

K. Girija et al. [260] synthesized self-assembled novel floral β -Ga₂O₃ nanorods via the reflux condensation method. The floral β -Ga₂O₃ nanorods possess the BET-specific surface area of 40.8 m²g⁻¹. In comparison with commercial Degussa TiO₂ (P25), the photodegradation of RhB by the synthesized β -Ga₂O₃ had a high efficiency of 90%. In

their other study [261], they prepared single crystalline β -Ga₂O₃ nanorods by a facile reflux condensation method using Ga(NO₃)₃·nH₂O and anionic surfactant CTAB as the precursor materials. The as prepared β -Ga₂O₃ nanorods possess a large surface area of 49.5 m²g⁻¹ and a band gap of 4.50 eV; β -Ga₂O₃ nanorods showed a good photo degradation efficiency of 92% and RhB degradation was achieved.

According to the above-mentioned, it can be found that the Ga₂O₃ material has excellent photodegradation characteristics, and the parameters affecting photodegradation characteristics include process parameters, annealing temperature, types of added materials, formulation ratios, and the micro-nano structure and crystal phase of the gallium oxide material.

5.5. Other Devices

In addition to the above-mentioned applications, some reports also propose other applications of gallium oxide materials via solution process method. Here, it is described as follows:

M. Tadatsugu et al. [12] prepared the first Ga₂O₃ based thin film via the sol-gel method. The Ga₂O₃: Mn thin film emitting layer (TFEL) was used to make a TFEL device combined with BaTiO₃ substrate in which they concluded that the film annealed at 900 °C and had an optimal performance. The TFEL device exhibited luminance of 1271 and 401 cd/m² when driven by sinusoidal wave voltages of 1 kHz and 60 Hz, respectively.

H. J. Bae et al. [215] synthesized high aspect ratio β -Ga₂O₃ nanorods by the hydrothermal method. Hydrothermally prepared β -Ga₂O₃ nanorods were used to fabricate FET by mechanically transferring nanorods onto back gated SiO₂/P⁺ Si substrate. It revealed the charge transfer properties of an n-type semiconductor. This unintentional n-type behavior in un-doped β -Ga₂O₃ was also reported by Kohei Sasaki et al. [294].

A. Kaya et al. [14] synthesized the β -Ga₂O₃ thin films on p-Si substrate using the sol-gel method. The electrical properties, such as break-down voltage, interface trap density, series resistance, and dielectric properties, were investigated by fabricating a MOS capacitor using sol-gel prepared β -Ga₂O₃ as oxide, p-Si as a semiconductor, and Ni/Au as a metal contact.

S. Gao et al. [15] synthesized β -Ga₂O₃ thin films coated on MOCVD grown GaN substrate by using the sol-gel method. They prepared a Ni/sol-gel β -Ga₂O₃/GaN MOS structure and found that its electrical parameters, such as I_o , n , and Φ_{ap} were strongly affected by temperature due the lateral inhomogeneity of barrier height.

5.6. Limitations and Challenges

There has been significant research on Ga₂O₃ material via solution-based synthesis methods and their applications to the present day. Even though growth processes in solution-based synthesis cannot be precisely controlled, they are considerably cheaper than vacuum-based synthesis methods. When compared to vacuum-based methods such as CVD and PVD, thin films prepared by solution methods have several defects and nanoparticles that were relatively large in size. The surface of thin films prepared by CVD and PVD is much smoother than that of solution methods. The surface area to volume ratio of nanomaterials synthesized using solution-based methods was high, which is important in sensor [187,216,217,220] and photocatalyst [212,231,260] applications. Large-scale synthesis and cost-effective approaches are critical for photoelectrodes and photocatalysis [295]. Process simplification and defect minimization, as well as growth and size control of solution processes can promote large-scale production and in-turn facilitates practical demonstration.

6. Conclusions

In this review, we have summarized the characteristics comparison and application fields of gallium oxide materials prepared by the hydrothermal method, sol-gel method, chemical bath method, and so on. Gallium oxide materials have shown a potential development in emerging technologies based on varied nanostructures via solution processes.

These structures are influenced by various techniques, materials, and process parameters employed in those corresponding synthesis methods. These used parameters also have a major role, as with change in parameters a change in formation was observed. In addition, gallium oxide materials can be effectively used as DUV detectors, gas sensors, pH sensors, photocatalytic and photodegradation applications, and so on. Hence, we hope that this review can provide a reference for researchers when preparing gallium oxide materials using solutions processes.

Author Contributions: Conceptualization, review and editing, D.-S.W.; writing—original draft preparation, review and editing, J.-L.C., B.K.Y. and M.-I.C. All authors have read and agreed to the published version of the manuscript.

Funding: This work was supported by the Ministry of Science and Technology (Taiwan, R.O.C.) under Grant Nos. 108-2221-E-005-028-MY3, 109-2811-E-005-508-MY2, and 109-2811-E-005-504. The authors also wish to express their sincere gratitude for the financial support by the “Innovation and Development Center of Sustainable Agriculture” from The Featured Areas Research Center Program within the framework of the Higher Education Sprout Project by the Ministry of Education (MOE) in Taiwan.

Institutional Review Board Statement: Not applicable.

Informed Consent Statement: Not applicable.

Data Availability Statement: The data that support the findings of this study are available from the corresponding author upon reasonable request.

Conflicts of Interest: The authors declare no conflict of interest.

References

1. De Boisbaudran, L. On the chemical and spectroscopic characters of a new metal (gallium). *Lond. Edinb. Dublin Philos. Mag. J. Sci.* **2009**, *50*, 414–416. [[CrossRef](#)]
2. Hill, V.G.; Roy, R.; Osborn, E.F. The system alumina-gallia-water. *J. Am. Ceram. Soc.* **1952**, *35*, 135–142. [[CrossRef](#)]
3. Roy, R.; Hill, V.G.; Osborn, E.F. Polymorphism of Ga_2O_3 and the system $\text{Ga}_2\text{O}_3\text{—H}_2\text{O}$. *J. Am. Chem. Soc.* **1952**, *74*, 719–722. [[CrossRef](#)]
4. Tippins, H.H. Optical absorption and photoconductivity in band edge of $\beta\text{-Ga}_2\text{O}_3$. *Phys. Rev.* **1965**, *140*, A316–A319. [[CrossRef](#)]
5. Zhang, J.Y.; Shi, J.L.; Qi, D.C.; Chen, L.; Zhang, K.H.L. Recent progress on the electronic structure, defect, and doping properties of Ga_2O_3 . *APL Mater.* **2020**, *8*, 35. [[CrossRef](#)]
6. Galazka, Z. $\beta\text{-Ga}_2\text{O}_3$ for wide-bandgap electronics and optoelectronics. *Semicond. Sci. Technol.* **2018**, *33*, 113001. [[CrossRef](#)]
7. Pearton, S.J.; Yang, J.; Cary, P.H.; Ren, F.; Kim, J.; Tadjer, M.J.; Mastro, M.A.A. Review of Ga_2O_3 materials, processing, and devices. *Appl. Phys. Rev.* **2018**, *5*, 011301. [[CrossRef](#)]
8. Shi, F.; Qiao, H. Preparations, properties and applications of gallium oxide nanomaterials—A Review. *Nano Select.* **2022**, *3*, 348–373. [[CrossRef](#)]
9. Kim, S.; Kim, J. Highly selective ozone-treated $\beta\text{-Ga}_2\text{O}_3$ solar-blind deep-UV photodetectors. *Appl. Phys. Lett.* **2020**, *117*, 6. [[CrossRef](#)]
10. Hasan, M.N.; Lai, J.Y.; Swinnich, E.; Zheng, Y.X.; Baboukani, B.S.; Nalam, P.C.; Seo, J.H. Investigation of nano-gaps in fractured $\beta\text{-Ga}_2\text{O}_3$ nanomembranes formed by uniaxial strain. *Adv. Electron. Mater.* **2021**, *7*, 9. [[CrossRef](#)]
11. Jedrzejczyk, M.; Zbudniewek, K.; Rynkowski, J.; Keller, V.; Grams, J.; Ruppert, A.M.; Keller, N. Wide band gap Ga_2O_3 as efficient UV-C photocatalyst for gas-phase degradation applications. *Environ. Sci. Pollut. Res.* **2017**, *24*, 26792–26805. [[CrossRef](#)]
12. Minami, T.; Shirai, T.; Nakatani, T.; Miyata, T. Electroluminescent devices with $\text{Ga}_2\text{O}_3\text{:Mn}$ thin-film emitting layer prepared by sol-gel process. *Jpn. J. Appl. Phys.* **2000**, *39*, L524–L526. [[CrossRef](#)]
13. Ji, Z.G.; Du, J.; Fan, J.; Wang, W. Gallium oxide films for filter and solar-blind UV detector. *Opt. Mater.* **2006**, *28*, 415–417. [[CrossRef](#)]
14. Kaya, A.; Mao, H.; Gao, J.; Chopdekar, R.V.; Takamura, Y.; Chowdhury, S.; Islam, M.S. An Investigation of Electrical and Dielectric Parameters of Sol–Gel Process Enabled $\beta\text{-Ga}_2\text{O}_3$ as a Gate Dielectric Material. *IEEE Trans. Electron. Devices* **2017**, *64*, 2047–2053. [[CrossRef](#)]
15. Gao, J.; Kaya, A.; Chopdekar, R.V.; Xu, Z.; Takamura, Y.; Islam, M.S.; Chowdhury, S. A Study of Temperature Dependent Current–Voltage (I–V–T) Characteristics in Ni/Sol–Gel $\beta\text{-Ga}_2\text{O}_3/\text{n-GaN}$ Structure. *J. Mater. Sci. Mater. Electron.* **2018**, *29*, 11265–11270. [[CrossRef](#)]
16. Kaur, D.; Kumar, M.A. Strategic review on gallium oxide based deep-ultraviolet photodetectors: Recent progress and future prospects. *Adv. Opt. Mater.* **2021**, *9*, 34. [[CrossRef](#)]

17. Zhao, B.; Wang, F.; Chen, H.Y.; Zheng, L.X.; Su, L.X.; Zhao, D.X.; Fang, X.S. An ultrahigh responsivity (9.7 MA W^{-1}) self-powered solar-blind photodetector based on individual ZnO-Ga₂O₃ heterostructures. *Adv. Funct. Mater.* **2017**, *27*, 8. [[CrossRef](#)]
18. Stepanov, S.I.; Nikolaev, V.I.; Bougrov, V.E.; Romanov, A.E. Gallium Oxide: Properties and Applications-A Review. *Rev. Adv. Mater. Sci.* **2016**, *44*, 63–86.
19. Xu, W.Y.; Chen, L.; Han, S.; Cao, P.J.; Fang, M.; Liu, W.J.; Zhu, D.L.; Lu, Y.M. Aqueous solution-processed boron-doped gallium oxide dielectrics for high-performance thin-film transistors. *J. Phys. Chem. C* **2020**, *124*, 8015–8023. [[CrossRef](#)]
20. Huang, C.C.; Yeh, C.S. GaOOH, and β - and γ -Ga₂O₃ nanowires: Preparation and photoluminescence. *New J. Chem.* **2010**, *34*, 103–107. [[CrossRef](#)]
21. Reddy, L.S.; Ko, Y.H.; Yu, J.S. Hydrothermal synthesis and photocatalytic property of β -Ga₂O₃ nanorods. *Nanoscale Res. Lett.* **2015**, *10*, 364. [[CrossRef](#)]
22. Chen, D.Z.; Xu, Y.; An, Z.Y.; Li, Z.; Zhang, C.F. Thin-film transistors based on wide bandgap Ga₂O₃ films grown by aqueous-solution spin-coating method. *Micro Nano Lett.* **2019**, *14*, 1052–1055. [[CrossRef](#)]
23. Jamwal, N.S.; Kiani, A. Gallium Oxide Nanostructures: A Review of Synthesis, Properties and Applications. *Nanomaterials* **2022**, *12*, 2061. [[CrossRef](#)]
24. Alhalaili, B.; Mao, H.; Islam, S. Ga₂O₃ Nanowire Synthesis and Device Applications. In *Novel Nanomaterials-Synthesis and Applications*; Mao, H., Ed.; InTech: Rijeka, Croatia, 2018; p. Ch. 2; ISBN 978-1-78923-089-5.
25. Marezio, M.; Remeika, J.P. Bond Lengths in α -Ga₂O₃ Structure and the high-pressure phase of Ga_{2-x}Fe_xO₃. *J. Chem. Phys.* **1967**, *46*, 1862–1865. [[CrossRef](#)]
26. Kohn, J.A.; Katz, G.; Broder, J.D. Characterization of β -Ga₂O₃ and its alumina isomorph, θ -Al₂O₃. *Am. Miner.* **1957**, *42*, 398–407.
27. He, H.Y.; Blanco, M.A.; Pandey, R. Electronic and thermodynamic properties of β -Ga₂O₃. *Appl. Phys. Lett.* **2006**, *88*, 3. [[CrossRef](#)]
28. He, H.Y.; Orlando, R.; Blanco, M.A.; Pandey, R.; Amzallag, E.; Baraille, I.; Rerat, M. First-principles study of the structural, electronic, and optical properties of Ga₂O₃ in its monoclinic and hexagonal phases. *Phys. Rev. B* **2006**, *74*, 195123. [[CrossRef](#)]
29. Cuong, N.D.; Park, Y.W.; Yoon, S.G. Microstructural and electrical properties of Ga₂O₃ nanowires grown at various temperatures by vapor-liquid-solid technique. *Sens. Actuators B-Chem.* **2009**, *140*, 240–244. [[CrossRef](#)]
30. Saurat, M.; Revcolevschi, A. Preparation by floating zone method, of refractory oxide monocrystals, in particular of gallium oxide, and study of some of their properties. *Rev. Int. Hautes Temp. Refract.* **1971**, *8*, 291.
31. Ahman, J.; Svensson, G.; Albertsson, J.A. Reinvestigation of β -Gallium oxide. *Acta Crystallogr. Sect. C-Cryst. Struct. Commun.* **1996**, *52*, 1336–1338. [[CrossRef](#)]
32. Playford, H.Y.; Hannon, A.C.; Barney, E.R.; Walton, R.I. Structures of uncharacterised polymorphs of gallium oxide from total neutron diffraction. *Chem.-A Eur. J.* **2013**, *19*, 2803–2813. [[CrossRef](#)] [[PubMed](#)]
33. Masataka, H.; Kohei, S.; Hisashi, M.; Yoshinao, K.; Akinori, K.; Akito, K.; Takekazu, M.; Shigenobu, Y. Recent progress in Ga₂O₃ power devices. *Semicond. Sci. Technol.* **2016**, *31*, 34001.
34. Higashiwaki, M.; Kuramata, A.; Murakami, H.; Kumagai, Y. State-of-the-art technologies of gallium oxide power devices. *J. Phys. D: Appl. Phys.* **2017**, *50*, 333002. [[CrossRef](#)]
35. Geller, S. Crystal structure of β -Ga₂O₃. *J. Chem. Phys.* **1960**, *33*, 676–684. [[CrossRef](#)]
36. Playford, H.Y.; Hannon, A.C.; Tucker, M.G.; Dawson, D.M.; Ashbrook, S.E.; Kastiban, R.J.; Sloan, J.; Walton, R.I. Characterization of structural disorder in γ -Ga₂O₃. *J. Phys. Chem. C* **2014**, *118*, 16188–16198. [[CrossRef](#)]
37. Yoshioka, S.; Hayashi, H.; Kuwabara, A.; Oba, F.; Matsunaga, K.; Tanaka, I. Structures and energetics of Ga₂O₃ polymorphs. *J. Phys. Condens. Matter* **2007**, *19*, 11. [[CrossRef](#)]
38. Zhao, Y.; Frost, R.L.; Yang, J.; Martens, W.N. Size and Morphology Control of Gallium Oxide Hydroxide GaO(OH), Nano- to Micro-Sized Particles by Soft-Chemistry Route without Surfactant. *J. Phys. Chem. C* **2008**, *112*, 3568–3579. [[CrossRef](#)]
39. Shi, L.; Zhang, J.; Wu, S.; Li, Y.; Jiang, L.; Cui, Q. Phase Evolution of Ga₂O₃ Produced from Morphology-Controllable α -GaOOH Nanocrystals. *J. Am. Ceram. Soc.* **2014**, *97*, 2607–2614. [[CrossRef](#)]
40. Shiba, F.; Yuasa, M.; Okawa, Y. Controlling the shape of wedge-like α -GaOOH particles formed by a hydrolysis process using sodium acetate as a growth modifier. *CrystEngComm* **2018**, *20*, 4910–4915. [[CrossRef](#)]
41. Qian, H.S.; Gunawan, P.; Zhang, Y.X.; Lin, G.F.; Zheng, J.W.; Xu, R. Template-Free Synthesis of Highly Uniform α -GaOOH Spindles and Conversion to α -Ga₂O₃ and β -Ga₂O₃. *Cryst. Growth Des.* **2008**, *8*, 1282–1287. [[CrossRef](#)]
42. Li, S.J.; Zheng, C.; Lobring, K.C. Refinement of the crystal structure of gallium oxide hydroxide, GaO(OH). *Z. Fur Krist.-New Cryst. Struct.* **2003**, *218*, 11–12.
43. Krehula, S.; Ristić, M.; Kubuki, S.; Iida, Y.; Fabián, M.; Musić, S. The formation and microstructural properties of uniform α -GaOOH particles and their calcination products. *J. Alloys Compd.* **2015**, *620*, 217–227. [[CrossRef](#)]
44. Markov, I.V. *Crystal Growth for Beginners*, 2nd ed.; World Scientific: Singapore, 2003; Volume 75, p. 564. [[CrossRef](#)]
45. Zhang, J.; Liu, Z.; Lin, C.; Lin, J.A. A simple method to synthesize β -Ga₂O₃ nanorods and their photoluminescence properties. *J. Cryst. Growth* **2005**, *280*, 99–106. [[CrossRef](#)]
46. Chikoidze, E.; von Bardeleben, H.J.; Akaiwa, K.; Shigematsu, E.; Kaneko, K.; Fujita, S.; Dumont, Y. Electrical, optical, and magnetic properties of Sn doped α -Ga₂O₃ thin films. *J. Appl. Phys.* **2016**, *120*, 9. [[CrossRef](#)]
47. Xue, H.; He, Q.; Jian, G.; Long, S.; Pang, T.; Liu, M. An Overview of the Ultrawide Bandgap Ga₂O₃ Semiconductor-Based Schottky Barrier Diode for Power Electronics Application. *Nanoscale Res. Lett.* **2018**, *13*, 290. [[CrossRef](#)]

48. Guo, D.; Guo, Q.; Chen, Z.; Wu, Z.; Li, P.; Tang, W. Review of Ga₂O₃-based optoelectronic devices. *Mater. Today Phys.* **2019**, *11*, 100157. [[CrossRef](#)]
49. Cocchi, C.; Zschiesche, H.; Nabok, D.; Mogilatenko, A.; Albrecht, M.; Galazka, Z.; Kirmse, H.; Draxl, C.; Koch, C.T. Atomic signatures of local environment from core-level spectroscopy in β -Ga₂O₃. *Phys. Rev. B* **2016**, *94*, 075147. [[CrossRef](#)]
50. Li, L.; Wei, W.; Behrens, M. Synthesis and characterization of α -, β -, and γ -Ga₂O₃ prepared from aqueous solutions by controlled precipitation. *Solid State Sci.* **2012**, *14*, 971–981. [[CrossRef](#)]
51. Zinkevich, M.; Morales, F.M.; Nitsche, H.; Ahrens, M.; Ruhle, M.; Aldinger, F. Microstructural and thermodynamic study of γ -Ga₂O₃. *Z. Fur Met.* **2004**, *95*, 756–762. [[CrossRef](#)]
52. Otero Areán, C.; Bellan, A.L.; Mentrui, M.P.; Delgado, M.R.; Palomino, G.T. Preparation and characterization of mesoporous γ -Ga₂O₃. *Microporous Mesoporous Mater.* **2000**, *40*, 35–42. [[CrossRef](#)]
53. Sharma, A.; Varshney, M.; Saraswat, H.; Chaudhary, S.; Parkash, J.; Shin, H.J.; Chae, K.H.; Won, S.O. Nano-structured phases of gallium oxide (GaOOH, α -Ga₂O₃, β -Ga₂O₃, γ -Ga₂O₃, δ -Ga₂O₃, and ϵ -Ga₂O₃): Fabrication, structural, and electronic structure investigations. *Int. Nano Lett.* **2020**, *10*, 71–79. [[CrossRef](#)]
54. Cora, I.; Mezzadri, F.; Boschi, F.; Bosi, M.; Caplovicova, M.; Calestani, G.; Dodony, I.; Pecz, B.; Fornari, R. The real structure of ϵ -Ga₂O₃ and its relation to κ -Phase. *Crystengcomm* **2017**, *19*, 1509–1516. [[CrossRef](#)]
55. Ollivier, B.; Retoux, R.; Lacorre, P.; Massiot, D.; Ferey, G. Crystal structure of κ -alumina: An X-ray powder diffraction, TEM and NMR study. *J. Mater. Chem.* **1997**, *7*, 1049–1056. [[CrossRef](#)]
56. Matsuzaki, K.; Hiramatsu, H.; Nomura, K.; Yanagi, H.; Kamiya, T.; Hirano, M.; Hosono, H. Growth, structure and carrier transport properties of Ga₂O₃ epitaxial film examined for transparent field-effect transistor. *Thin Solid Film.* **2006**, *496*, 37–41. [[CrossRef](#)]
57. Orita, M.; Hiramatsu, H.; Ohta, H.; Hirano, M.; Hosono, H. Preparation of highly conductive, deep ultraviolet transparent β -Ga₂O₃ thin film at low deposition temperatures. *Thin Solid Film.* **2002**, *411*, 134–139. [[CrossRef](#)]
58. Mezzadri, F.; Calestani, G.; Boschi, F.; Delmonte, D.; Bosi, M.; Fornari, R. Crystal Structure and Ferroelectric Properties of ϵ -Ga₂O₃ Films Grown on (0001)-Sapphire. *Inorg. Chem.* **2016**, *55*, 12079–12084. [[CrossRef](#)]
59. Xia, X.; Chen, Y.; Feng, Q.; Liang, H.; Tao, P.; Xu, M.; Du, G. Hexagonal phase-pure wide band gap ϵ -Ga₂O₃ films grown on 6H-SiC substrates by metal organic chemical vapor deposition. *Appl. Phys. Lett.* **2016**, *108*, 202103. [[CrossRef](#)]
60. Maccioni, M.B.; Fiorentini, V. Phase diagram and polarization of stable phases of (Ga_{1-x}In_x)₂O₃. *Appl. Phys. Express* **2016**, *9*, 4. [[CrossRef](#)]
61. Tadjer, M.J.; Mastro, M.A.; Mahadik, N.A.; Currie, M.; Wheeler, V.D.; Freitas, J.A.; Greenlee, J.D.; Hite, J.K.; Hobart, K.D.; Eddy, C.R.; et al. Structural, Optical, and Electrical Characterization of Monoclinic β -Ga₂O₃ Grown by MOVPE on Sapphire Substrates. *J. Electron. Mater.* **2016**, *45*, 2031–2037. [[CrossRef](#)]
62. Kracht, M.; Karg, A.; Schörmann, J.; Weinhold, M.; Zink, D.; Michel, F.; Rohnke, M.; Schowalter, M.; Gerken, B.; Rosenauer, A.; et al. Tin-Assisted Synthesis of ϵ -Ga₂O₃ by Molecular Beam Epitaxy. *Phys. Rev. Appl.* **2017**, *8*, 54002. [[CrossRef](#)]
63. Cho, S.B.; Mishra, R. Epitaxial engineering of polar ϵ -Ga₂O₃ for tunable two-dimensional electron gas at the heterointerface. *Appl. Phys. Lett.* **2018**, *112*, 5. [[CrossRef](#)]
64. Yamaguchi, K. First principles study on electronic structure of β -Ga₂O₃. *Solid State Commun.* **2004**, *131*, 739–744. [[CrossRef](#)]
65. Binet, L.; Gourier, D.; Minot, C. Relation between Electron Band Structure and Magnetic Bistability of Conduction Electrons in β -Ga₂O₃. *J. Solid State Chem.* **1994**, *113*, 420–433. [[CrossRef](#)]
66. Hajnal, Z.; Miro, J.; Kiss, G.; Reti, F.; Deak, P.; Herndon, R.C.; Kuperberg, J.M. Role of oxygen vacancy defect states in the n-type conduction of β -Ga₂O₃. *J. Appl. Phys.* **1999**, *86*, 3792–3796. [[CrossRef](#)]
67. Li, C.; Yan, J.L.; Zhang, L.Y.; Zhao, G. Electronic structures and optical properties of Zn-doped β -Ga₂O₃ with different doping sites. *Chin. Phys. B* **2012**, *21*, 6. [[CrossRef](#)]
68. Ping, L.K.; Mohamed, M.A.; Mondal, A.K.; Taib, M.F.M.; Samat, M.H.; Berhanuddin, D.D.; Menon, P.S.; Bahru, R. First-Principles Studies for Electronic Structure and Optical Properties of Strontium Doped β -Ga₂O₃. *Micromachines* **2021**, *12*, 16. [[CrossRef](#)]
69. Zhao, Y.; Yan, J. First-principles study of n-type tin/fluorine codoped beta-gallium oxides. *J. Semicond.* **2015**, *36*, 82004. [[CrossRef](#)]
70. Zhang, L.Y.; Yan, J.L.; Zhang, Y.J.; Li, T.; Ding, X.W. First-principles study on electronic structure and optical properties of N-doped P-type β -Ga₂O₃. *Sci. China-Phys. Mech. Astron.* **2012**, *55*, 19–24. [[CrossRef](#)]
71. Zhang, Y.J.; Yan, J.L.; Zhao, G.; Xie, W.F. First-principles study on electronic structure and optical properties of Sn-doped β -Ga₂O₃. *Phys. B-Condens. Matter* **2010**, *405*, 3899–3903. [[CrossRef](#)]
72. Peelaers, H.; Van deWalle, C.G. Brillouin zone and band structure of β -Ga₂O₃. *Phys. Status Solidi B-Basic Solid State Phys.* **2015**, *252*, 828–832. [[CrossRef](#)]
73. Navarro-Quezada, A.; Alamé, S.; Esser, N.; Furthmüller, J.; Bechstedt, F.; Galazka, Z.; Skuridina, D.; Vogt, P. Near valence-band electronic properties of semiconducting β -Ga₂O₃ (100) single crystals. *Phys. Rev. B* **2015**, *92*, 195306. [[CrossRef](#)]
74. Varley, J.B.; Weber, J.R.; Janotti, A.; Van de Walle, C.G. Oxygen vacancies and donor impurities in β -Ga₂O₃. *Appl. Phys. Lett.* **2010**, *97*, 142106. [[CrossRef](#)]
75. Furthmüller, J.; Bechstedt, F. Quasiparticle bands and spectra of Ga₂O₃ polymorphs. *Phys. Rev. B* **2016**, *93*, 16. [[CrossRef](#)]
76. Dong, L.P.; Jia, R.X.; Xin, B.; Peng, B.; Zhang, Y.M. Effects of oxygen vacancies on the structural and optical properties of β -Ga₂O₃. *Sci. Rep.* **2017**, *7*, 12. [[CrossRef](#)]
77. Ma, X.F.; Zhang, Y.M.; Dong, L.P.; Jia, R.X. First-principles calculations of electronic and optical properties of aluminum-doped β -Ga₂O₃ with intrinsic defects. *Results Phys.* **2017**, *7*, 1582–1589. [[CrossRef](#)]

78. Yan, H.Y.; Guo, Y.R.; Song, Q.G.; Chen, Y.F. First-principles study on electronic structure and optical properties of Cu-doped β -Ga₂O₃. *Phys. B-Condens. Matter* **2014**, *434*, 181–184. [[CrossRef](#)]
79. Orita, M.; Ohta, H.; Hirano, M.; Hosono, H. Deep-ultraviolet transparent conductive β -Ga₂O₃ thin films. *Appl. Phys. Lett.* **2000**, *77*, 4166–4168. [[CrossRef](#)]
80. Litimein, F.; Rached, D.; Khenata, R.; Baltache, H. FPLAPW study of the structural, electronic, and optical properties of Ga₂O₃: Monoclinic and hexagonal phases. *J. Alloys Compd.* **2009**, *488*, 148–156. [[CrossRef](#)]
81. Von Wenckstern, H. Group-III Sesquioxides: Growth, Physical Properties and Devices. *Adv. Electron. Mater.* **2017**, *3*, 1600350. [[CrossRef](#)]
82. Higashiwaki, M.; Sasaki, K.; Kuramata, A.; Masui, T.; Yamakoshi, S. Gallium oxide (Ga₂O₃) metal-semiconductor field-effect transistors on single-crystal β -Ga₂O₃ (010) substrates. *Appl. Phys. Lett.* **2012**, *100*, 13504. [[CrossRef](#)]
83. Sang, L.W.; Liao, M.Y.; Sumiya, M. A Comprehensive Review of Semiconductor Ultraviolet Photodetectors: From Thin Film to One-Dimensional Nanostructures. *Sensors* **2013**, *13*, 10482–10518. [[CrossRef](#)]
84. Chen, H.Y.; Liu, K.W.; Hu, L.F.; Al-Ghamdi, A.A.; Fang, X.S. New concept ultraviolet photodetectors. *Mater. Today* **2015**, *18*, 493–502. [[CrossRef](#)]
85. Zhao, B.; Wang, F.; Chen, H.Y.; Wang, Y.P.; Jiang, M.M.; Fang, X.S.; Zhao, D.X. Solar-Blind Avalanche Photodetector Based On Single ZnO-Ga₂O₃ Core-Shell Microwire. *Nano Lett.* **2015**, *15*, 3988–3993. [[CrossRef](#)]
86. Suzuki, N.; Ohira, S.; Tanaka, M.; Sugawara, T.; Nakajima, K.; Shishido, T. Fabrication and characterization of transparent conductive Sn-doped β -Ga₂O₃ single crystal. *Phys. Status Solidi C* **2007**, *4*, 2310–2313. [[CrossRef](#)]
87. Zhang, J.G.; Li, B.; Xia, C.T.; Pei, G.Q.; Deng, Q.; Yang, Z.H.; Xu, W.S.; Shi, H.S.; Wu, F.; Wu, Y.Q.; et al. Growth and spectral characterization of β -Ga₂O₃ single crystals. *J. Phys. Chem. Solids* **2006**, *67*, 2448–2451. [[CrossRef](#)]
88. Villora, E.G.; Yamaga, M.; Inoue, T.; Yabasi, S.; Masui, Y.; Sugawara, T.; Fukuda, T. Optical Spectroscopy Study on β -Ga₂O₃. *Jpn. J. Appl. Phys. Part 2-Lett. Express Lett.* **2002**, *41*, L622–L625. [[CrossRef](#)]
89. Ueda, N.; Hosono, H.; Waseda, R.; Kawazoe, H. Synthesis and control of conductivity of ultraviolet transmitting β -Ga₂O₃ single crystals. *Appl. Phys. Lett.* **1997**, *70*, 3561–3563. [[CrossRef](#)]
90. Korhonen, E.; Tuomisto, F.; Gogova, D.; Wagner, G.; Baldini, M.; Galazka, Z.; Schewski, R.; Albrecht, M. Electrical compensation by Ga vacancies in Ga₂O₃ thin films. *Appl. Phys. Lett.* **2015**, *106*, 3. [[CrossRef](#)]
91. Dong, L.P.; Jia, R.X.; Li, C.; Xin, B.; Zhang, Y.M. Ab initio study of N-doped β -Ga₂O₃ with intrinsic defects: The structural, electronic and optical properties Linpeng The Structural, Electronic and Optical Properties. *J. Alloys Compd.* **2017**, *712*, 379–385. [[CrossRef](#)]
92. Galazka, Z.; Irmischer, K.; Uecker, R.; Bertram, R.; Pietsch, M.; Kwasniewski, A.; Naumann, M.; Schulz, T.; Schewski, R.; Klimm, D.; et al. On the bulk β -Ga₂O₃ single crystals grown by the Czochralski method. *J. Cryst. Growth* **2014**, *404*, 184–191. [[CrossRef](#)]
93. Qin, Y.; Long, S.B.; Dong, H.; He, Q.M.; Jian, G.Z.; Zhang, Y.; Hou, X.H.; Tan, P.J.; Zhang, Z.F.; Lv, H.B.; et al. Review of deep ultraviolet photodetector based on gallium oxide. *Chin. Phys. B* **2019**, *28*, 17. [[CrossRef](#)]
94. Higashiwaki, M.; Murakami, H.; Kumagai, Y.; Kuramata, A. Current status of Ga₂O₃ power devices To. *Jpn. J. Appl. Phys.* **2016**, *55*, 7. [[CrossRef](#)]
95. Sasaki, K.; Kuramata, A.; Masui, T.; Villora, E.G.; Shimamura, K.; Yamakoshi, S. Device-Quality β -Ga₂O₃ Epitaxial Films Fabricated by Ozone Molecular Beam Epitaxy. *Appl. Phys. Express* **2012**, *5*, 35502. [[CrossRef](#)]
96. Villora, E.G.; Shimamura, K.; Yoshikawa, Y.; Ujiie, T.; Aoki, K. Electrical conductivity and carrier concentration control in β -Ga₂O₃ by Si doping. *Appl. Phys. Lett.* **2008**, *92*, 202120. [[CrossRef](#)]
97. Ma, N.; Tanen, N.; Verma, A.; Guo, Z.; Luo, T.F.; Xing, H.; Jena, D. Intrinsic electron mobility limits in β -Ga₂O₃. *Appl. Phys. Lett.* **2016**, *109*, 212101. [[CrossRef](#)]
98. Baliga, B.J. Power Semiconductor Device Figure of Merit for High-Frequency Applications. *IEEE Electron Device Lett.* **1989**, *10*, 455–457. [[CrossRef](#)]
99. Baliga, B.J. Semiconductors for high-voltage, vertical channel field-effect transistors. *J. Appl. Phys.* **1982**, *53*, 1759–1764. [[CrossRef](#)]
100. Ueda, N.; Hosono, H.; Waseda, R.; Kawazoe, H. Anisotropy of electrical and optical properties in β -Ga₂O₃ single crystals. *Appl. Phys. Lett.* **1997**, *71*, 933–935. [[CrossRef](#)]
101. Schubert, M.; Korlacki, R.; Knight, S.; Hofmann, T.; Schoche, S.; Darakchieva, V.; Janzen, E.; Monemar, B.; Gogova, D.; Thieu, Q.T.; et al. Anisotropy, phonon modes, and free charge carrier parameters in monoclinic β -gallium oxide single crystals. *Phys. Rev. B* **2016**, *93*, 18. [[CrossRef](#)]
102. Ueda, O.; Ikenaga, N.; Koshi, K.; Iizuka, K.; Kuramata, A.; Hanada, K.; Moribayashi, T.; Yamakoshi, S.; Kasu, M. Structural evaluation of defects in β -Ga₂O₃ single crystals grown by edge-defined film-fed growth process. *Jpn. J. Appl. Phys.* **2016**, *55*, 8. [[CrossRef](#)]
103. Guo, Z.; Verma, A.; Wu, X.F.; Sun, F.Y.; Hickman, A.; Masui, T.; Kuramata, A.; Higashiwaki, M.; Jena, D.; Luo, T.F. Anisotropic thermal conductivity in single crystal β -gallium oxide. *Appl. Phys. Lett.* **2015**, *106*, 5. [[CrossRef](#)]
104. Mu, W.X.; Jia, Z.T.; Yin, Y.R.; Hu, Q.Q.; Li, Y.; Wu, B.Y.; Zhang, J.; Tao, X.T. High quality crystal growth and anisotropic physical characterization of β -Ga₂O₃ single crystals grown by EFG method. *J. Alloys Compd.* **2017**, *714*, 453–458. [[CrossRef](#)]
105. Hebb, J.P.; Jensen, K.F. The Effect of Patterns on Thermal Stress during Rapid Thermal Processing of Silicon Wafers. *IEEE Trans. Semicond. Manuf.* **1998**, *11*, 99–107. [[CrossRef](#)]

106. Heuer, A.H.; Reddy, A.; Hovis, D.B.; Veal, B.; Paulikas, A.; Vlad, A.; Ruhle, M. the effect of surface orientation on oxidation-induced growth strains in single crystal NiAl: An in situ synchrotron study. *Scr. Mater.* **2006**, *54*, 1907–1912. [[CrossRef](#)]
107. Ang, K.W.; Chui, K.J.; Bliznetsov, V.; Tung, C.H.; Du, A.; Balasubramanian, N.; Samudra, G.; Li, M.F.; Yeo, Y.C. Lattice strain analysis of transistor structures with silicon-germanium and silicon-carbon source/drain stressors. *Appl. Phys. Lett.* **2005**, *86*, 3. [[CrossRef](#)]
108. Toda, A.; Ikarashi, N.; Ono, H.; Ito, S.; Toda, T.; Imai, K. Local lattice strain distribution around a transistor channel in metal-oxide-semiconductor devices. *Appl. Phys. Lett.* **2001**, *79*, 4243–4245. [[CrossRef](#)]
109. Villora, E.G.; Shimamura, K.; Ujiie, T.; Aoki, K. Electrical conductivity and lattice expansion of β -Ga₂O₃ below room temperature. *Appl. Phys. Lett.* **2008**, *92*, 3. [[CrossRef](#)]
110. Orlandi, F.; Mezzadri, F.; Calestani, G.; Boschi, F.; Fornari, R. Thermal expansion coefficients of β -Ga₂O₃ single crystals. *Appl. Phys. Express* **2015**, *8*, 3. [[CrossRef](#)]
111. Cheng, Z.Z.; Hanke, M.; Galazka, Z.; Trampert, A. Thermal expansion of single-crystalline β -Ga₂O₃ from RT to 1200 K studied by synchrotron-based high-resolution x-ray diffraction. *Appl. Phys. Lett.* **2018**, *113*, 4. [[CrossRef](#)]
112. Adachi, K.; Ogi, H.; Takeuchi, N.; Nakamura, N.; Watanabe, H.; Ito, T.; Ozaki, Y. Unusual elasticity of monoclinic β -Ga₂O₃. *J. Appl. Phys.* **2018**, *124*, 7. [[CrossRef](#)]
113. Luan, S.Z.; Dong, L.P.; Jia, R.X. Analysis of the structural, anisotropic elastic and electronic properties of β -Ga₂O₃ with various pressures. *J. Cryst. Growth* **2019**, *505*, 74–81. [[CrossRef](#)]
114. Handwerg, M.; Mitdank, R.; Galazka, Z.; Fischer, S.F. Temperature-dependent thermal conductivity and diffusivity of a mg-doped insulating β -Ga₂O₃ single crystal along [100], [010] and [001]. *Semicond. Sci. Technol.* **2016**, *31*, 6. [[CrossRef](#)]
115. Galazka, Z.; Uecker, R.; Irmscher, K.; Albrecht, M.; Klimm, D.; Pietsch, M.; Brutzam, M.; Bertram, R.; Ganschow, S.; Fornari, R. czochralski growth and characterization of β -Ga₂O₃ single crystals. *Cryst. Res. Technol.* **2010**, *45*, 1229–1236. [[CrossRef](#)]
116. Rebien, M.; Henrion, W.; Hong, M.; Mannaerts, J.P.; Fleischer, M. Optical properties of gallium oxide thin films. *Appl. Phys. Lett.* **2002**, *81*, 250–252. [[CrossRef](#)]
117. Hoeneisen, B.; Mead, C.A.; Nicolet, M.A. Permittivity of β -Ga₂O₃ at low frequencies. *Solid-State Electron.* **1971**, *14*, 1057–1059. [[CrossRef](#)]
118. Pritula, I.; Sangwal, K. 29-Fundamentals of Crystal Growth from Solutions. In *Handbook of Crystal Growth*, 2nd ed.; Rudolph, P., Ed.; Elsevier: Boston, MA, USA, 2015; Volume 2, pp. 1185–1227. ISBN 978-0-444-63303-3.
119. Kashchiev, D.; van Rosmalen, G.M. Review: Nucleation in solutions revisited. *Cryst. Res. Technol.* **2003**, *38*, 555–574. [[CrossRef](#)]
120. Charitidis, C.A.; Georgiou, P.; Koklioti, M.A.; Trompeta, A.F.; Markakis, V. Manufacturing nanomaterials: From research to industry. *Manuf. Rev.* **2014**, *1*, 11. [[CrossRef](#)]
121. Karatutlu, A.; Barhoum, A.; Sapelkin, A. Chapter 1-Liquid-phase synthesis of nanoparticles and nanostructured materials. In *Emerging Applications of Nanoparticles and Architecture Nanostructures: Current Prospects and Future Trends*; Barhoum, A., Makhoulouf, A.S.H., Eds.; Elsevier: Amsterdam, The Netherlands, 2018; pp. 1–28. ISBN 978-0-323-51254-1.
122. Hench, L.L.; West, J.K. The Sol-Gel Process. *Chem. Rev.* **1990**, *90*, 33–72. [[CrossRef](#)]
123. Bokov, D.; Jalil, A.T.; Chupradit, S.; Suksatan, W.; Ansari, M.J.; Shewael, I.H.; Valiev, G.H.; Kianfar, E. Nanomaterial by Sol-Gel Method: Synthesis and Application. *Adv. Mater. Sci. Eng.* **2021**, *2021*, 21. [[CrossRef](#)]
124. Wang, J.; Li, C.; Xu, B. Basic principle advance and current application situation of Sol-Gel method. *Chem. Ind. Eng.* **2009**, *26*, 273–277.
125. Aggarwal, G.; Nagpal, M. Pharmaceutical Polymer Gels in Drug Delivery. In *Polymer Gels; Gels Horizons: From Science to Smart Materials*; Thakur, V.K., Thakur, M.K., Voicu, S.I., Eds.; Springer: Singapore, 2018; pp. 249–284. ISBN 978-981-10-6079-3.
126. Shinde, S.S.; Bhosale, C.H.; Rajpure, K.Y. Photocatalytic degradation of toluene using sprayed N-doped ZnO thin films in aqueous suspension. *J. Photochem. Photobiol. B-Biol.* **2012**, *113*, 70–77. [[CrossRef](#)] [[PubMed](#)]
127. Shinde, S.S.; Bhosale, C.H.; Rajpure, K.Y. Photoelectrochemical properties of highly mobilized Li-doped ZnO thin film. *J. Photochem. Photobiol. B-Biol.* **2013**, *120*, 1–9. [[CrossRef](#)] [[PubMed](#)]
128. Shinde, S.S.; Shinde, P.S.; Bhosale, C.H.; Rajpure, K.Y. Zinc oxide mediated heterogeneous photocatalytic degradation of organic species under solar radiation. *J. Photochem. Photobiol. B-Biol.* **2011**, *104*, 425–433. [[CrossRef](#)]
129. Jaroenworarluck, A.; Sunsaneeyametha, W.; Kosachan, N.; Stevens, R. Characteristics of silica-coated TiO₂ and its UV absorption for sunscreen cosmetic applications. *Surf. Interface Anal.* **2006**, *38*, 473–477. [[CrossRef](#)]
130. Vijayalakshmi, R.; Rajendran, V. Synthesis and characterization of nano-TiO₂ via different methods. *Arch. Appl. Sci. Res.* **2012**, *4*, 1183–1190.
131. Li, B.R.; Wang, X.H.; Yan, M.Y.; Li, L.T. Preparation and characterization of nano-TiO₂ powder. *Mater. Chem. Phys.* **2003**, *78*, 184–188. [[CrossRef](#)]
132. Verma, R.; Mantri, B.; Kumar Srivastava, A. Shape control synthesis, characterizations, mechanisms and optical properties of large scaled metal oxide nanostructures of ZnO and TiO₂. *Adv. Mater. Lett.* **2015**, *6*, 324–333. [[CrossRef](#)]
133. Kandiel, T.A.; Robben, L.; Alkaim, A.; Bahnemann, D. Brookite versus anatase TiO₂ photocatalysts: Phase transformations and photocatalytic activities. *Photochem. Photobiol. Sci.* **2013**, *12*, 602–609. [[CrossRef](#)]
134. Li, H.X.; Bian, Z.F.; Zhu, J.; Zhang, D.Q.; Li, G.S.; Huo, Y.N.; Li, H.; Lu, Y.F. Mesoporous Titania Spheres with Tunable Chamber Structure and Enhanced Photocatalytic Activity. *J. Am. Chem. Soc.* **2007**, *129*, 8406–8407. [[CrossRef](#)]

135. Verma, R.; Awasthi, A.; Singh, P.; Srivastava, R.; Sheng, H.P.; Wen, J.G.; Miller, D.J.; Srivastava, A.K. Interactions of titania based nanoparticles with silica and green-tea: Photo-degradation and -luminescence. *J. Colloid Interface Sci.* **2016**, *475*, 82–95. [[CrossRef](#)]
136. Zhang, L.J.; Menendez-Flores, V.M.; Murakami, N.; Ohno, T. Improvement of photocatalytic activity of brookite titanium dioxide nanorods by surface modification using chemical etching. *Appl. Surf. Sci.* **2012**, *258*, 5803–5809. [[CrossRef](#)]
137. Collinson, M.M.; Wang, H.M.; Makote, R.; Khramov, A. The effects of drying time and relative humidity on the stability of sol-gel derived silicate films in solution. *J. Electroanal. Chem.* **2002**, *519*, 65–71. [[CrossRef](#)]
138. Kajihara, K. Recent advances in sol-gel synthesis of monolithic silica and silica-based glasses. *J. Asian Ceram. Soc.* **2013**, *1*, 121–133. [[CrossRef](#)]
139. Li, Y.; White, T.; Lim, S.H. Structure Control and Its Influence on Photoactivity and Phase Transformation of TiO₂ Nano-Particles. *Rev. Adv. Mater. Sci.* **2003**, *5*, 211–215.
140. Niederberger, M.; Pinna, N. *Metal Oxide Nanoparticles in Organic Solvents: Synthesis, Formation, Assembly and Application*; Springer Science & Business Media: New York, NY, USA, 2009. ISBN 1848826710.
141. Modan, E.M.; Plăiașu, A.G. Advantages and Disadvantages of Chemical Methods in the Elaboration of Nanomaterials. *Ann. “Dunarea De Jos” Univ. Galati. Fascicle IX Metall. Mater. Sci.* **2020**, *43*, 53–60. [[CrossRef](#)]
142. Byrappa, K.; Yoshimura, M.; McGuire, G.E.; Rossnagel, S.M.; Bunshah, R.F. Hydrothermal Technology—Principles and Applications. In *Handbook of hydrothermal technology: A Technology for Crystal Growth and Materials Processing*; William Andrew: New York, NY, USA, 2012; pp. 1–52. ISBN 143778364.
143. Byrappa, K.; Adschiri, T. Hydrothermal technology for nanotechnology. *Prog. Cryst. Growth Charact. Mater.* **2007**, *53*, 117–166. [[CrossRef](#)]
144. Yoshimura, M.; Byrappa, K. Hydrothermal processing of materials: Past, present and future. *J. Mater. Sci.* **2008**, *43*, 2085–2103. [[CrossRef](#)]
145. Zheng, H.; Yu, T.; Qu, C.; Li, W.; Wang, Y. Basic Characteristics and Application Progress of Supercritical Water. *IOP Conf. Ser. Earth Environ. Sci.* **2020**, *555*, 12036. [[CrossRef](#)]
146. Lester, E.; Blood, P.; Denyer, J.; Giddings, D.; Azzopardi, B.; Poliakoff, M. Reaction engineering: The supercritical water hydrothermal synthesis of nano-particles. *J. Supercrit. Fluids* **2006**, *37*, 209–214. [[CrossRef](#)]
147. Hayashi, H.; Hakuta, Y. Hydrothermal Synthesis of Metal Oxide Nanoparticles in Supercritical Water. *Materials* **2010**, *3*, 3794–3817. [[CrossRef](#)]
148. Brunner, G.; Kiran, E. *Properties of Pure Water In Hydrothermal and Supercritical Water Processes*; Elsevier: Amsterdam, The Netherlands, 2014; Volume 5, p. 10. ISBN 0444594183.
149. Prakasam, M.; Viraphong, O.; Cambon, O.; Largeteau, A. Hydrothermal Crystal Growth and Applications. In *Advances in Solid Oxide Fuel Cells and Electronic Ceramics*; Bansal, N.P., Kusnezoff, M., Shimamura, K., Eds.; Wiley: Hoboken, NJ, USA, 2015; pp. 151–156.
150. Demazeau, G.; Largeteau, A. Hydrothermal/Solvothermal Crystal Growth: An Old but Adaptable Process. *J. Inorg. Gen. Chem.* **2015**, *641*, 159–163. [[CrossRef](#)]
151. McMillen, C.D.; Kolis, J.W. Bulk single crystal growth from hydrothermal solutions. *Philos. Mag.* **2012**, *92*, 2686–2711. [[CrossRef](#)]
152. Xu, H.Y.; Wang, H.; Jin, T.N.; Yan, H. Rapid fabrication of luminescent Eu: YVO₄ films by microwave-assisted chemical solution deposition. *Nanotechnology* **2005**, *16*, 65–69. [[CrossRef](#)]
153. Xu, H.Y.; Le Xu, S.; Li, X.D.; Wang, H.; Yan, H. chemical bath deposition of hausmannite Mn₃O₄ thin films. *Appl. Surf. Sci.* **2006**, *252*, 4091–4096. [[CrossRef](#)]
154. Niesen, T.P.; De Guire, M.R. Review: Deposition of ceramic thin films at low temperatures from aqueous solutions. *J. Electroceramics* **2001**, *6*, 169–207. [[CrossRef](#)]
155. Mane, R.S.; Lokhande, C.D. Chemical deposition method for metal chalcogenide thin films. *Mater. Chem. Phys.* **2000**, *65*, 1–31. [[CrossRef](#)]
156. Cheng, A.; Fan, D.B.; Wang, H.; Liu, B.W.; Zhang, Y.C.; Yan, H. chemical bath deposition of crystalline ZnS thin films. *Semicond. Sci. Technol.* **2003**, *18*, 676–679. [[CrossRef](#)]
157. Varkey, A.J.; Fort, A.F. Some optical properties of silver peroxide (AgO) and silver oxide (Ag₂O) films produced by chemical-bath deposition. *Sol. Energy Mater. Sol. Cells* **1993**, *29*, 253–259. [[CrossRef](#)]
158. Varkey, A.J.; Fort, A.F. Solution growth technique for deposition of nickel oxide thin films. *Thin Solid Film.* **1993**, *235*, 47–50. [[CrossRef](#)]
159. Saeed, T.; O'Brien, P. Deposition and characterisation of ZnO thin films grown by chemical bath deposition. *Thin Solid Film.* **1995**, *271*, 35–38. [[CrossRef](#)]
160. Zang, L. Lecture 10: Homogeneous Nucleation. University of Utah. Available online: <https://my.eng.utah.edu/~ljzang/teaching/index.html> (accessed on 1 May 2022).
161. Zang, L. Lecture 12: Heterogeneous Nucleation—A Surface Catalyzed Process. University of Utah. Available online: <https://my.eng.utah.edu/~ljzang/teaching/index.html> (accessed on 6 May 2022).
162. Nucleation. Encyclopaedia Britannica. Available online: <https://www.britannica.com/science/nucleation> (accessed on 11 May 2022).

163. Nair, P.K.; Nair, M.T.S.; Garcia, V.M.; Arenas, O.L.; Pena, Y.; Castillo, A.; Ayala, I.T.; Gomezdaza, O.; Sanchez, A.; Campos, J.; et al. Semiconductor thin films by chemical bath deposition for solar energy related applications. *Sol. Energy Mater. Sol. Cells* **1998**, *52*, 313–344. [[CrossRef](#)]
164. Choi, J.Y.; Kim, K.J.; Yoo, J.B.; Kim, D.H. Properties of Cadmium Sulfide Thin Films Deposited by Chemical Bath Deposition with Ultrasonication. *Sol. Energy* **1998**, *64*, 41–47. [[CrossRef](#)]
165. Nichols, L. 1.4K: Reflux. In *Organic Chemistry Lab Techniques*; Nichols, L., Ed.; LibreTexts: Oroville, CA, USA, 2017; p. 6.
166. Matijevic, E. Monodispersed Metal (Hydrous) Oxides—A Fascinating Field of Colloid Science. *Acc. Chem. Res.* **1981**, *14*, 22–29. [[CrossRef](#)]
167. Cao, G.; Wang, Y. Zero-dimensional nanostructures: Nanoparticles. In *Nanostructures and Nanomaterials: Synthesis, Properties, and Applications*; Brock, S.L., Ed.; Imperial College Press: London, UK, 2004; pp. 51–109.
168. Jiang, Y. Forced hydrolysis and chemical co-precipitation. In *Handbook of Nanophase and Nanostructured Materials Vol. 1 Synthesis*; Wang, Z.L., Liu, Y., Zhang, Z., Eds.; Springer: Boston, MA, USA, 2003; Volume 1, pp. 55–71. ISBN 0306467372.
169. Ring, T.A.; Kudo, Y. Fundamentals of Forced Hydrolysis of Indium Hydroxide. In *Fine Particles Science and Technology: From Micro to Nanoparticles*; Pelizzetti, E., Ed.; Springer: Dordrecht, The Netherlands, 1996; Volume 12, pp. 141–159. ISBN 978-94-009-0259-6.
170. Kandori, K.; Shigetomi, T.; Ishikawa, T. study on forced hydrolysis reaction of acidic $\text{Fe}_2(\text{SO}_4)_3$ solution—structure and properties of precipitates. *Colloids Surf. a-Physicochem. Eng. Asp.* **2004**, *232*, 19–28. [[CrossRef](#)]
171. Gattorno, G.R.; Oskam, G. Forced Hydrolysis vs Self-Hydrolysis of Zinc Acetate in Ethanol and Iso-butanol. *ECS Trans.* **2006**, *3*, 23–28. [[CrossRef](#)]
172. Pathan, H.M.; Lokhande, C.D. Deposition of metal chalcogenide thin films by successive ionic layer adsorption and reaction (SILAR) method. *Bull. Mater. Sci.* **2004**, *27*, 85–111. [[CrossRef](#)]
173. Sartale, S.D.; Lokhande, C.D. Growth of copper sulphide thin films by successive ionic layer adsorption and reaction (SILAR) method. *Mater. Chem. Phys.* **2000**, *65*, 63–67. [[CrossRef](#)]
174. Ghosh, B.; Das, M.; Banerjee, P.; Das, S. Fabrication and optical properties of SnS thin films by SILAR method. *Appl. Surf. Sci.* **2008**, *254*, 6436–6440. [[CrossRef](#)]
175. Ratnayake, S.P.; Ren, J.W.; Colusso, E.; Guglielmi, M.; Martucci, A.; DellaGaspara, E. SILAR Deposition of Metal Oxide Nanostructured Films. *Small* **2021**, *17*, 32. [[CrossRef](#)]
176. Mageshwari, K.; Sathyamoorthy, R. Physical properties of nanocrystalline CuO thin films prepared by the SILAR method. *Mater. Sci. Semicond. Process.* **2013**, *16*, 337–343. [[CrossRef](#)]
177. Rodriguez, C.A.D.; Tremiliosi-Filho, G. Electrochemical Deposition. In *Encyclopedia of Tribology*; Wang, Q.J., Chung, Y.W., Eds.; Springer: Boston, MA, USA, 2013; pp. 918–922. ISBN 978-0-387-92897-5.
178. Therese, G.H.A.; Kamath, P.V. Electrochemical Synthesis of Metal Oxides and Hydroxides. *Chem. Mater.* **2000**, *12*, 1195–1204. [[CrossRef](#)]
179. Li, Y.; Trinchi, A.; Wlodarski, W.; Galatsis, K.; Kalantar-Zadeh, K. investigation of the oxygen gas sensing performance of Ga_2O_3 thin films with different dopants. *Sens. Actuators B Chem.* **2003**, *93*, 431–434. [[CrossRef](#)]
180. Ristić, M.; Popović, S.; Musić, S. Application of Sol–Gel Method in the Synthesis of Gallium(III)-Oxide. *Mater. Lett.* **2005**, *59*, 1227–1233. [[CrossRef](#)]
181. Kokubun, Y.; Miura, K.; Endo, F.; Nakagomi, S. Sol-gel prepared $\beta\text{-Ga}_2\text{O}_3$ thin films for ultraviolet photodetectors. *Appl. Phys. Lett.* **2007**, *90*, 2–4. [[CrossRef](#)]
182. Suzuki, R.; Nakagomi, S.; Kokubun, Y. Solar-blind photodiodes composed of a Au Schottky contact and a $\beta\text{-Ga}_2\text{O}_3$ single crystal with a high resistivity cap layer. *Appl. Phys. Lett.* **2011**, *98*, 13–15. [[CrossRef](#)]
183. Gopal, R.; Goyal, A.; Saini, A.; Nagar, M.; Sharma, N.; Gupta, D.K.; Dhayal, V. Sol-gel synthesis of Ga_2O_3 nanorods and effect of precursor chemistry on their structural and morphological properties. *Ceram. Int.* **2018**, *44*, 19099–19105. [[CrossRef](#)]
184. Sinha, G.; Ganguli, D.; Chaudhuri, S. Crystallization and optical properties of finite sized $\beta\text{-Ga}_2\text{O}_3$ in sol-gel derived $\text{Ga}_2\text{O}_3\text{:SiO}_2$ nanocomposites. *J. Phys. Condens. Matter* **2006**, *18*, 11167–11176. [[CrossRef](#)]
185. Sinha, G.; Datta, A.; Panda, S.K.; Chavan, P.G.; More, M.A.; Joag, D.S.; Patra, A. Self-catalytic growth and field-emission properties of Ga_2O_3 nanowires. *J. Phys. D Appl. Phys.* **2009**, *42*, 185409. [[CrossRef](#)]
186. Cheng, B.; Samulski, E.T. Fabrication and characterization of nanotubular semiconductor oxides In_2O_3 and Ga_2O_3 . *J. Mater. Chem.* **2001**, *11*, 2901–2902. [[CrossRef](#)]
187. Mohammadi, M.R.; Fray, D.J. Semiconductor $\text{TiO}_2\text{-Ga}_2\text{O}_3$ thin film gas sensors derived from particulate sol-gel route. *Acta Mater.* **2007**, *55*, 4455–4466. [[CrossRef](#)]
188. Shen, H.; Yin, Y.; Tian, K.; Baskaran, K.; Duan, L.; Zhao, X.; Tiwari, A. Growth and characterization of $\beta\text{-Ga}_2\text{O}_3$ thin films by sol-gel method for fast-response solar-blind ultraviolet photodetectors. *J. Alloys Compd.* **2018**, *766*, 601–608. [[CrossRef](#)]
189. Yu, M.; Lv, C.; Yu, J.; Shen, Y.; Yuan, L.; Hu, J.; Zhang, S.; Cheng, H.; Zhang, Y.; Jia, R. High-performance photodetector based on sol-gel epitaxially grown $\alpha/\beta\text{-Ga}_2\text{O}_3$ thin films. *Mater. Today Commun.* **2020**, *25*, 101532. [[CrossRef](#)]
190. Yu, S.; Zhang, G.; Carloni, D.; Wu, Y. fabrication, microstructure and optical properties of Ga_2O_3 transparent ceramics. *Ceram. Int.* **2020**, *46*, 21757–21761. [[CrossRef](#)]
191. Zhu, Y.; Xiu, X.; Cheng, F.; Li, Y.; Xie, Z.; Tao, T.; Chen, P.; Liu, B.; Zhang, R.; Zheng, Y.D. Growth and nitridation of $\beta\text{-Ga}_2\text{O}_3$ thin films by sol-gel spin-coating epitaxy with post-annealing process. *J. Sol-Gel Sci. Technol.* **2021**, *100*, 183–191. [[CrossRef](#)]

192. Sinha, G.; Adhikary, K.; Chaudhuri, S. Effect of annealing temperature on structural transformation of gallium based nanocrystalline oxide thin films and their optical properties. *Opt. Mater.* **2007**, *29*, 718–722. [[CrossRef](#)]
193. Fleischer, M.; Hanrieder, W.; Meixner, H. Stability of semiconducting gallium oxide thin films. *Thin Solid Film.* **1990**, *190*, 93–102. [[CrossRef](#)]
194. Battiston, G.A.; Gerbasi, R.; Porchia, M.; Bertinello, R.; Caccavale, F. Chemical vapour deposition and characterization of gallium oxide thin films. *Thin Solid Film.* **1996**, *279*, 115–118. [[CrossRef](#)]
195. Mayo, M.J.; Suresh, A.; Porter, W.D. Thermodynamics for nanosystems: Grain and particle-size dependent phase diagrams. *Rev. Adv. Mater. Sci.* **2003**, *5*, 100–109.
196. Binet, L.; Gourier, D. Origin of the blue luminescence of β -Ga₂O₃. *J. Phys. Chem. Solids* **1998**, *59*, 1241–1249. [[CrossRef](#)]
197. Yao, Y.; Okur, S.; Lyle, L.A.M.; Tompa, G.S.; Salagaj, T.; Sbrockey, N.; Davis, R.F.; Porter, L.M. Growth and characterization of α -, β -, and ϵ -phases of Ga₂O₃ using MOCVD and HVPE techniques. *Mater. Res. Lett.* **2018**, *6*, 268–275. [[CrossRef](#)]
198. Nakagomi, S.; Kokubun, Y. Cross-sectional TEM imaging of β -Ga₂O₃ thin films formed on c-plane and a -plane sapphire substrates. *Phys. Status Solidi A Appl. Mater. Sci.* **2013**, *210*, 1738–1744. [[CrossRef](#)]
199. Xu, W.; Shi, J.; Li, Y.; Xiu, X.; Ding, S.; Xie, Z.; Tao, T.; Chen, P.; Liu, B.; Zhang, R.; et al. Study of β -Ga₂O₃ films hetero-epitaxially grown on off-angled sapphire substrates by halide vapor phase epitaxy. *Mater. Lett.* **2021**, *289*, 129411. [[CrossRef](#)]
200. Li, Y.; Xiu, X.; Xu, W.; Zhang, L.; Xie, Z.; Tao, T.; Chen, P.; Liu, B.; Zhang, R.; Zheng, Y. Microstructural analysis of heteroepitaxial β -Ga₂O₃ films grown on (0001) sapphire by halide vapor phase epitaxy. *J. Phys. D Appl. Phys.* **2021**, *54*, 014003. [[CrossRef](#)]
201. Suman, S.; Mukurala, N.; Kushwaha, A.K. Annealing induced surface restructuring in hydrothermally synthesized gallium oxide nano-cuboids. *J. Cryst. Growth* **2021**, *554*, 125946. [[CrossRef](#)]
202. Liu, J.; Zhang, G. Mesoporous mixed-phase Ga₂O₃: Green synthesis and enhanced photocatalytic activity. *Mater. Res. Bull.* **2015**, *68*, 254–259. [[CrossRef](#)]
203. Zhao, Y.; Frost, R.L.; Martens, W.N. Synthesis and Characterization of Gallium Oxide Nanostructures via a Soft-Chemistry Route. *J. Phys. Chem. C* **2007**, *111*, 16290–16299. [[CrossRef](#)]
204. Quan, Y.; Fang, D.; Zhang, X.; Liu, S.; Huang, K. Synthesis and Characterization of Gallium Oxide Nanowires via a Hydrothermal Method. *Mater. Chem. Phys.* **2010**, *121*, 142–146. [[CrossRef](#)]
205. Wang, J.; Li, Q.; Qiu, X.; He, Y.; Liu, W. Soft-Template Mediated Synthesis of GaOOH Nanorod-Shelled Microspheres and Thermal Conversion to β -Ga₂O₃. *J. Nanosci. Nanotechnol.* **2010**, *10*, 4308–4311. [[CrossRef](#)]
206. Muruganandham, M.; Amutha, R.; Wahed, M.S.M.A.; Ahmmad, B.; Kuroda, Y.; Suri, R.P.S.; Wu, J.J.; Sillanpää, M.E.T. Controlled Fabrication of α -GaOOH and α -Ga₂O₃ Self-Assembly and Its Superior Photocatalytic Activity. *J. Phys. Chem. C* **2012**, *116*, 44–53. [[CrossRef](#)]
207. Li, D.; Duan, X.; Qin, Q.; Fan, H.; Zheng, W. Ionic liquid-assisted synthesis of mesoporous α -Ga₂O₃ hierarchical structures with enhanced photocatalytic activity. *J. Mater. Chem. A* **2013**, *1*, 12417. [[CrossRef](#)]
208. Arul Prakasam, B.; Lahtinen, M.; Muruganandham, M.; Sillanpää, M. Synthesis of self-assembled α -GaOOH microrods and 3d hierarchical architectures with flower like morphology and their conversion to α -Ga₂O₃. *Mater. Lett.* **2015**, *158*, 370–372. [[CrossRef](#)]
209. Kang, B.K.; Mang, S.R.; Song, K.M.; Lee, K.S.; Yoon, D.H. Hydrothermal synthesis and characterization of uniform β -Ga₂O₃ hollow nanostructures by carbon nanospheres. *J. Ceram. Process. Res.* **2014**, *15*, 200–203.
210. Shi, F.; Qiao, H. Influence of hydrothermal reaction time on crystal qualities and photoluminescence properties of β -Ga₂O₃ nanorods. *J. Mater. Sci. Mater. Electron.* **2020**, *31*, 20223–20231. [[CrossRef](#)]
211. Cui, L.; Wang, H.; Xin, B.; Mao, G. One-step rapid synthesis of ultrafine γ -Ga₂O₃ nanocrystals by microwave hydrothermal method in ammonium hydroxide medium. *Appl. Phys. A Mater. Sci. Process.* **2017**, *123*, 634. [[CrossRef](#)]
212. Zhao, W.; Yang, Y.; Hao, R.; Liu, F.; Wang, Y.; Tan, M.; Tang, J.; Ren, D.; Zhao, D. Synthesis of mesoporous β -Ga₂O₃ nanorods using PEG as template: Preparation, characterization and photocatalytic properties. *J. Hazard. Mater.* **2011**, *192*, 1548–1554. [[CrossRef](#)]
213. Wang, Y.; Li, N.; Duan, P.; Sun, X.; Chu, B.; He, Q. Properties and Photocatalytic Activity of β -Ga₂O₃ Nanorods under Simulated Solar Irradiation. *J. Nanomater.* **2015**, *2015*, 5. [[CrossRef](#)]
214. Fujihara, S.; Shibata, Y.; Hosono, E. Chemical Deposition of Rodlike GaOOH and β -Ga₂O₃ Films Using Simple Aqueous Solutions. *J. Electrochem. Soc.* **2005**, *152*, C764. [[CrossRef](#)]
215. Bae, H.J.; Yoo, T.H.; Yoon, Y.; Lee, I.G.; Kim, J.P.; Cho, B.J.; Hwang, W.S. High-Aspect Ratio β -Ga₂O₃ Nanorods via Hydrothermal Synthesis. *Nanomaterials* **2018**, *8*, 594. [[CrossRef](#)]
216. Pilliadugula, R.; Krishnan, N.G. Gas sensing performance of GaOOH and β -Ga₂O₃ synthesized by hydrothermal method: A comparison. *Mater. Res. Express* **2019**, *6*, 025027. [[CrossRef](#)]
217. Pilliadugula, R.; Krishnan, N.G. Effect of pH dependent morphology on room temperature nh₃ sensing performances of β -Ga₂O₃. *Mater. Sci. Semicond. Process.* **2020**, *112*, 105007. [[CrossRef](#)]
218. Shi, F.; Qiao, H. Effects of hydrothermal temperatures on crystalline quality and photoluminescence properties of β -Ga₂O₃ microspheres using ammonia as a precipitator. *CrystEngComm* **2021**, *23*, 492–498. [[CrossRef](#)]
219. Lin, H.J.; Baltrus, J.P.; Gao, H.; Ding, Y.; Nam, C.Y.; Ohodnicki, P.; Gao, P.X. Perovskite Nanoparticle-Sensitized Ga₂O₃ Nanorod Arrays for CO Detection at High Temperature. *ACS Appl. Mater. Interfaces* **2016**, *8*, 8880–8887. [[CrossRef](#)]
220. Zhang, B.; Lin, H.J.; Gao, H.; Lu, X.; Nam, C.Y.; Gao, P.X. Perovskite-sensitized β -Ga₂O₃ nanorod arrays for highly selective and sensitive NO₂ detection at high temperature. *J. Mater. Chem. A* **2020**, *8*, 10845–10854. [[CrossRef](#)]

221. Zhang, J.; Jiao, S.; Wan, Y.; Gao, S.; Wang, D.; Wang, J.Z. A well-grown β -Ga₂O₃ microrod array formed from GaOOH on a Si (100) substrate and growth mechanism study. *CrystEngComm* **2018**, *20*, 4329–4335. [[CrossRef](#)]
222. Atilgan, A.; Yildiz, A.; Harmanci, U.; Gulluoglu, M.T.; Salimi, K. β -Ga₂O₃ nanoflakes/p-Si heterojunction self-powered photodiodes. *Mater. Today Commun.* **2020**, *24*, 101105. [[CrossRef](#)]
223. Guo, D.Y.; Chen, K.; Wang, S.L.; Wu, F.M.; Liu, A.P.; Li, C.R.; Li, P.G.; Tan, C.K.; Tang, W.H. Self-Powered Solar-Blind Photodetectors Based on α/β Phase Junction of Ga₂O₃. *Phys. Rev. Appl.* **2020**, *13*, 024051. [[CrossRef](#)]
224. Wu, C.; He, C.; Guo, D.; Zhang, F.; Li, P.; Wang, S.; Liu, A.; Wu, F.; Tang, W. Vertical α/β -Ga₂O₃ phase junction nanorods array with graphene-silver nanowire hybrid conductive electrode for high-performance self-powered solar-blind photodetectors. *Mater. Today Phys.* **2020**, *12*, 100193. [[CrossRef](#)]
225. He, C.; Guo, D.; Chen, K.; Wang, S.; Shen, J.; Zhao, N.; Liu, A.; Zheng, Y.; Li, P.; Wu, Z.; et al. α -Ga₂O₃ Nanorod Array-Cu₂O Microsphere p-n Junctions for Self-Powered Spectrum-Distinguishable Photodetectors. *ACS Appl. Nano Mater.* **2019**, *2*, 4095–4103. [[CrossRef](#)]
226. Wang, S.; Chen, K.; Zhao, H.; He, C.; Wu, C.; Guo, D.; Zhao, N.; Ungar, G.; Shen, J.; Chu, X.; et al. β -Ga₂O₃ nanorod arrays with high light-to-electron conversion for solar-blind deep ultraviolet photodetection. *RSC Adv.* **2019**, *9*, 6064–6069. [[CrossRef](#)]
227. Zhang, J.; Jiao, S.; Wang, D.; Gao, S.; Wang, J.; Zhao, L. Nano tree-like branched structure with α -Ga₂O₃ covered by γ -Al₂O₃ for highly efficient detection of solar-blind ultraviolet light using self-powered photoelectrochemical method. *Appl. Surf. Sci.* **2021**, *541*, 148380. [[CrossRef](#)]
228. Ryou, H.; Yoo, T.H.; Yoon, Y.; Lee, I.G.; Shin, M.; Cho, J.; Cho, B.J.; Hwang, W.S. Hydrothermal Synthesis and Photocatalytic Property of Sn-Doped β -Ga₂O₃ Nanostructure. *ECS J. Solid State Sci. Technol.* **2020**, *9*, 045009. [[CrossRef](#)]
229. Pilliadugula, R.; Gopalakrishnan, N. Room temperature ammonia sensing performances of pure and sn doped β -Ga₂O₃. *Mater. Sci. Semicond. Process.* **2021**, *135*, 106086. [[CrossRef](#)]
230. Wang, J.; Jiang, S.; Liu, H.; Wang, S.; Pan, Q.; Yin, Y.; Zhang, G. P- type gas-sensing behavior of Ga₂O₃/Al₂O₃ nanocomposite with high sensitivity to NO_x at room temperature. *J. Alloys Compd.* **2020**, *814*, 152284. [[CrossRef](#)]
231. Kim, S.; Ryou, H.; Lee, I.G.; Shin, M.; Cho, B.J.; Hwang, W.S. Impact of Al doping on a hydrothermally synthesized β -Ga₂O₃ nanostructure for photocatalysis applications. *RSC Adv.* **2021**, *11*, 7338–7346. [[CrossRef](#)]
232. Shi, Y.; Li, H.; Chen, L.; Huang, X. Obtaining ultra-long copper nanowires via a hydrothermal process. *Sci. Technol. Adv. Mater.* **2005**, *6*, 761–765. [[CrossRef](#)]
233. Liu, Z.; Li, S.; Yang, Y.; Peng, S.; Hu, Z.; Qian, Y. Complex-Surfactant-Assisted Hydrothermal Route to Ferromagnetic Nickel Nanobelts. *Adv. Mater.* **2003**, *15*, 1946–1948. [[CrossRef](#)]
234. Sun, Y.; Xia, Y. Large-Scale Synthesis of Uniform Silver Nanowires Through a Soft, Self-Seeding, Polyol Process. *Adv. Mater.* **2002**, *14*, 833–837. [[CrossRef](#)]
235. Harwig, T.; Kellendonk, F. Some Observations on the Photoluminescence of Doped β -Galliumsesquioxide. *J. Solid State Chem.* **1978**, *24*, 255–263. [[CrossRef](#)]
236. Xu, H.; Wang, W. Template Synthesis of Multishelled Cu₂O Hollow Spheres with a Single-Crystalline Shell Wall. *Angew. Chem.-Int. Ed.* **2007**, *46*, 1489–1492. [[CrossRef](#)]
237. Firouzabadi, H.; Iranpoor, N.; Gholinejad, M. One-Pot Thioetherification of Aryl Halides Using Thiourea and Alkyl Bromides Catalyzed by Copper(I) Iodide Free from Foul-Smelling Thiols in Wet Polyethylene Glycol (PEG 200). *Adv. Synth. Catal.* **2010**, *352*, 119–124. [[CrossRef](#)]
238. Hou, Y.; Wang, X.; Wu, L.; Ding, Z.; Fu, X. Efficient Decomposition of Benzene over a β -Ga₂O₃ Photocatalyst under Ambient Conditions. *Environ. Sci. Technol.* **2006**, *40*, 5799–5803. [[CrossRef](#)] [[PubMed](#)]
239. Cüneyt Taş, A.; Majewski, P.J.; Aldinger, F. Synthesis of Gallium Oxide Hydroxide Crystals in Aqueous Solutions with or without Urea and Their Calcination Behavior. *J. Am. Ceram. Soc.* **2002**, *85*, 1421–1429. [[CrossRef](#)]
240. Jolivet, J.; Henry, M.; Livage, J. *Metal Oxide Chemistry and Synthesis: From Solution to Solid State*; John Wiley: Hoboken, NJ, USA, 2000; p. 344. ISBN 978-0-471-97056-9.
241. Hassan, M.A.; Waseem, A.; Johar, M.A.; Bagal, I.V.; Ha, J.S.; Ryu, S.W. Single-Step fabrication of 3d hierarchical ZnO/ZnS heterojunction branched nanowires by MOCVD for enhanced photoelectrochemical water splitting. *J. Mater. Chem. A* **2020**, *8*, 8300–8312. [[CrossRef](#)]
242. Oshima, T.; Kato, Y.; Magome, E.; Kobayashi, E.; Takahashi, K. Characterization of pseudomorphic γ -Ga₂O₃ and γ -Al₂O₃ films on MgAl₂O₄ substrates and the band-alignment at the coherent γ -Ga₂O₃/Al₂O₃ heterojunction interface. *Jpn. J. Appl. Phys.* **2019**, *58*, 060910. [[CrossRef](#)]
243. Edwards, D.D.; Mason, T.O. Subsolidus Phase Relations in the Ga₂O₃-In₂O₃-SnO₂ System. *J. Am. Ceram. Soc.* **1998**, *81*, 3285–3292. [[CrossRef](#)]
244. Pedley, J.B.; Marshall, E.M. Thermochemical Data for Gaseous Monoxides. *J. Phys. Chem. Ref. Data* **1983**, *12*, 967–1031. [[CrossRef](#)]
245. Zhao, Q.; Ju, D.; Deng, X.; Huang, J.; Cao, B.; Xu, X. Morphology-Modulation of SnO₂ Hierarchical Architectures by Zn Doping for Glycol Gas Sensing and Photocatalytic Applications. *Sci. Rep.* **2015**, *5*, 2–10. [[CrossRef](#)]
246. Li, X.; Mu, Z.; Hu, J.; Cui, Z. Chemical gas sensing characteristics of composite NiO/Al₂O₃ for 2-chloroethanol at low temperature. *Sens. Actuators B. Chem.* **2016**, *232*, 143–149. [[CrossRef](#)]
247. Peelaers, H.; Varley, J.B.; Speck, J.S.; Van DeWalle, C.G. Structural and electronic properties of Ga₂O₃-Al₂O₃ alloys. *Appl. Phys. Lett.* **2018**, *112*, 242101. [[CrossRef](#)]

248. Li, G.; Peng, C.; Li, C.; Yang, P.; Hou, Z.; Fan, Y.; Cheng, Z.; Lin, J. Shape-Controllable Synthesis and Morphology-Dependent Luminescence Properties of GaOOH:Dy³⁺ and β -Ga₂O₃:Dy³⁺. *Inorg. Chem.* **2010**, *49*, 1449–1457. [[CrossRef](#)]
249. Mizunashi, T.; Fujihara, S. Elaboration and Tunable Photoluminescence of β -Ga₂O₃: Eu³⁺ Films by Urea-Assisted Aqueous Chemical Bath Deposition. *Electrochem. Solid-State Lett.* **2008**, *11*, 43–46. [[CrossRef](#)]
250. Yeh, C.Y.; Zhao, Y.M.; Li, H.; Yu, F.P.; Zhang, S.; Wu, D.S. Growth and Photocatalytic Properties of Gallium Oxide Films Using Chemical Bath Deposition. *Crystals* **2019**, *9*, 564. [[CrossRef](#)]
251. Hector, G.; Appert, E.; Sarigiannidou, E.; Matheret, E.; Roussel, H.; Chaix-Pluchery, O.; Consonni, V. Chemical Synthesis of β -Ga₂O₃ microrods on Silicon and Its Dependence on the Gallium Nitrate Concentration. *Inorg. Chem.* **2020**, *59*, 15696–15706. [[CrossRef](#)]
252. Chiang, J.L.; Shang, Y.G.; Yadlapalli, B.K.; Yu, F.P.; Wu, D.S. Ga₂O₃ nanorod-based extended-gate field-effect transistors for pH sensing. *Mater. Sci. Eng. B Solid-State Mater. Adv. Technol.* **2022**, *276*, 115542. [[CrossRef](#)]
253. Sinha, G.; Patra, A. Generation of green, red and white light from rare-earth doped Ga₂O₃ nanoparticles. *Chem. Phys. Lett.* **2009**, *473*, 151–154. [[CrossRef](#)]
254. Sinha, G.; Chaudhuri, S. Controlled solvothermal synthesis of β -Ga₂O₃ 3D microstructures and their optical properties. *Mater. Chem. Phys.* **2009**, *114*, 644–649. [[CrossRef](#)]
255. Muruganandham, M.; Suri, R.; Abdel, M.S.M.; Sillanpää, M.; Ahmmad, B.; Lee, G.; Wu, J.J. Solvothermal synthesis of mesoporous α -GaOOH semi-nanospheres. *Mater. Lett.* **2013**, *111*, 137–139. [[CrossRef](#)]
256. Zhang, W.; Naidu, B.S.; Ou, J.Z.; O'Mullane, A.P.; Chrimes, A.F.; Carey, B.J.; Wang, Y.; Tang, S.; Sivan, V.; Mitchell, A.; et al. Liquid Metal/Metal Oxide Frameworks with Incorporated Ga₂O₃ for Photocatalysis. *ACS Appl. Mater. Interfaces* **2015**, *7*, 1943–1948. [[CrossRef](#)]
257. Kang, B.K.; Lim, H.D.; Mang, S.R.; Song, K.M.; Jung, M.K.; Kim, S.; Yoon, D.H. Synthesis and Characterization of Monodispersed β -Ga₂O₃ Nanospheres via Morphology Controlled Ga₄(OH)₁₀SO₄ Precursors. *Langmuir* **2015**, *31*, 833–838. [[CrossRef](#)]
258. Kang, B.K.; Lim, G.H.; Lim, B.; Yoon, D.H. Morphology controllable synthesis and characterization of gallium compound hierarchical structures via forced-hydrolysis method. *J. Alloys Compd.* **2016**, *675*, 57–63. [[CrossRef](#)]
259. Huang, E.; Li, J.; Wu, G.; Dai, W.; Guan, N.; Li, L. A simple synthesis of Ga₂O₃ and GaN nanocrystals. *RSC Adv.* **2017**, *7*, 47898–47903. [[CrossRef](#)]
260. Girija, K.; Thirumalairajan, S.; Patra, A.K.; Mangalaraj, D.; Ponpandian, N.; Viswanathan, C. Enhanced photocatalytic performance of novel self-assembled floral β -Ga₂O₃ nanorods. *Curr. Appl. Phys.* **2013**, *13*, 652–658. [[CrossRef](#)]
261. Girija, K.; Thirumalairajan, S.; Mangalaraj, D. Morphology controllable synthesis of parallelly arranged single-crystalline β -Ga₂O₃ nanorods for photocatalytic and antimicrobial activities. *Chem. Eng. J.* **2014**, *236*, 181–190. [[CrossRef](#)]
262. Vequizo, J.J.M.; Ichimura, M. Electrodeposition of Ga-O Thin Films from Aqueous Gallium Sulfate Solutions. *Jpn. J. Appl. Phys.* **2013**, *52*, 075503. [[CrossRef](#)]
263. Ghazali, N.M.; Mahmood, M.R.; Yasui, K.; Hashim, A.M. Electrochemically deposited gallium oxide nanostructures on silicon substrates. *Nanoscale Res. Lett.* **2014**, *9*, 120. [[CrossRef](#)] [[PubMed](#)]
264. ISO 21348; Space Environment (Natural and Artificial)—Process for Determining Solar Irradiances, 1st ed.; ISO: Geneva, Switzerland, 2007.
265. Chen, X.; Ren, F.; Gu, S.; Ye, J. Review of Gallium-Oxide-Based Solar-Blind Ultraviolet Photodetectors. *Photonics Res.* **2019**, *7*, 381. [[CrossRef](#)]
266. Osamura, K.; Nakajima, K.; Murakami, Y.; Shingu, P.H.; Ohtsuki, A. Fundamental absorption edge in GaN, InN and their alloys. *Solid State Commun.* **1972**, *11*, 617–621. [[CrossRef](#)]
267. Ye, J.D.; Gu, S.L.; Zhu, S.M.; Liu, S.M.; Zheng, Y.D.; Zhang, R.; Shi, Y.; Yu, H.Q.; Ye, Y.D. Gallium doping dependence of single-crystal n-type ZnO grown by metal organic chemical vapor deposition. *J. Cryst. Growth* **2005**, *283*, 279–285. [[CrossRef](#)]
268. Persson, C.; Platzer-Björkman, C.; Malmström, J.; Törndahl, T.; Edoff, M. Strong Valence-Band Offset Bowing of ZnO_{1-x}S_x Enhances p-Type Nitrogen Doping of ZnO-like Alloys. *Phys. Rev. Lett.* **2006**, *97*, 1–4. [[CrossRef](#)]
269. Vigué, F.; Tournié, E.; Faurie, J.P. Evaluation of the potential of ZnSe and Zn(Mg)BeSe compounds for ultraviolet photodetection. *IEEE J. Quantum Electron.* **2001**, *37*, 1146–1152. [[CrossRef](#)]
270. Morkoç, H.; Strite, S.; Gao, G.B.; Lin, M.E.; Sverdlov, B.; Burns, M. Large-band-gap SiC, III-V nitride, and II-VI ZnSe-based semiconductor device technologies. *J. Appl. Phys.* **1994**, *76*, 1363–1398. [[CrossRef](#)]
271. Chen, X.; Zhu, H.; Cai, J.; Wu, Z. High-performance 4H-SiC-based ultraviolet p-i-n photodetector. *J. Appl. Phys.* **2007**, *102*, 024505. [[CrossRef](#)]
272. Yim, W.M.; Stofko, E.J.; Zanzucchi, P.J.; Pankove, J.I.; Ettenberg, M.; Gilbert, S.L. Epitaxially grown AlN and its optical band gap. *J. Appl. Phys.* **1973**, *44*, 292–296. [[CrossRef](#)]
273. Salvatori, S.; Rossi, M.C.; Galluzzi, F.; Pace, E. Solar-blind UV-photodetector based on polycrystalline diamond films: Basic design principle and comparison with experimental results. *Mater. Sci. Eng. B* **1997**, *46*, 105–111. [[CrossRef](#)]
274. Chen, Y.C.; Lu, Y.J.; Lin, C.N.; Tian, Y.Z.; Gao, C.J.; Dong, L.; Shan, C.X. Self-powered diamond/ β -Ga₂O₃ photodetectors for solar-blind imaging. *J. Mater. Chem. C* **2018**, *6*, 5727–5732. [[CrossRef](#)]
275. Zheng, W.; Lin, R.; Zhang, Z.; Huang, F. Vacuum-Ultraviolet Photodetection in Few-Layered h-BN. *ACS Appl. Mater. Interfaces* **2018**, *10*, 27116–27123. [[CrossRef](#)]

276. Onuma, T.; Saito, S.; Sasaki, K.; Masui, T.; Yamaguchi, T.; Honda, T.; Higashiwaki, M. Valence Band Ordering in β -Ga₂O₃ Studied by Polarized Transmittance and Reflec. *Jpn. J. Appl. Phys.* **2015**, *54*, 112601. [[CrossRef](#)]
277. Akaiwa, K.; Fujita, S. Electrical Conductive Corundum-Structured α -Ga₂O₃ Thin Films on Sapphire with Tin-Doping Grown by Sprayassisted Mist Chemical Vapor Deposition. *Jpn. J. Appl. Phys.* **2012**, *51*, 070203. [[CrossRef](#)]
278. Li, D.; Jiang, K.; Sun, X.; Guo, C. AlGa_N photonics: Recent advances in materials and ultraviolet devices. *Adv. Opt. Photonics* **2018**, *10*, 43. [[CrossRef](#)]
279. Fujita, S.; Oda, M.; Kaneko, K.; Hitora, T. Evolution of corundum-structured iii-oxide semiconductors: Growth, properties, and devices. *Jpn. J. Appl. Phys.* **2016**, *55*, 1202A3. [[CrossRef](#)]
280. Kim, M.; Seo, J.H.; Singiseti, U.; Ma, Z. Recent advances in free-standing single crystalline wide band-gap semiconductors and their applications: GaN, SiC, ZnO, β -Ga₂O₃, and diamond. *J. Mater. Chem. C* **2017**, *5*, 8338–8354. [[CrossRef](#)]
281. Tsao, J.Y.; Chowdhury, S.; Hollis, M.A.; Jena, D.; Johnson, N.M.; Jones, K.A.; Kaplar, R.J.; Rajan, S.; Van deWalle, C.G.; Bellotti, E.; et al. Ultrawide-Bandgap Semiconductors: Research Opportunities and Challenges. *Adv. Electron. Mater.* **2018**, *4*, 1600501. [[CrossRef](#)]
282. Trinchì, A.; Włodarski, W.; Li, Y.X. Hydrogen sensitive Ga₂O₃ schottky diode sensor based on SiC. *Sens. Actuators B Chem.* **2004**, *100*, 94–98. [[CrossRef](#)]
283. Wu, Y.-L.; Chang, S.-P.; Chang, S.-J.; Weng, W.Y.; Lin, Y.H.A. Novel PH Sensor Using Extended-Gate Field-Effect Transistors with Ga₂O₃ Nanowires Fabricated on SiO₂/Si Template. *Sci. Adv. Mater.* **2015**, *7*, 475–478. [[CrossRef](#)]
284. Manjakkal, L.; Szwagierczak, D.; Dahiya, R. Metal oxides based electrochemical pH sensors: Current progress and future perspectives. *Prog. Mater. Sci.* **2020**, *109*, 100635. [[CrossRef](#)]
285. Tan, L.L.; Ong, W.J.; Chai, S.P.; Goh, B.T.; Mohamed, A.R. Visible-light-active oxygen-rich TiO₂ decorated 2D graphene oxide with enhanced photocatalytic activity toward carbon dioxide reduction. *Appl. Catal. B Environ.* **2015**, *179*, 160–170. [[CrossRef](#)]
286. Liu, L.; Gao, F.; Zhao, H.; Li, Y. Tailoring Cu valence and oxygen vacancy in Cu/TiO₂ catalysts for enhanced CO₂ photoreduction efficiency. *Appl. Catal. B Environ.* **2013**, *134–135*, 349–358. [[CrossRef](#)]
287. Núñez, J.; De La Peña O’Shea, V.A.; Jana, P.; Coronado, J.M.; Serrano, D.P. Effect of copper on the performance of ZnO and ZnO_{1-x}N_x oxides as CO₂ photoreduction catalysts. *Catal. Today* **2013**, *209*, 21–27. [[CrossRef](#)]
288. Pan, Y.X.; Sun, Z.Q.; Cong, H.P.; Men, Y.L.; Xin, S.; Song, J.; Yu, S.H. Photocatalytic CO₂ reduction highly enhanced by oxygen vacancies on Pt-nanoparticle-dispersed gallium oxide. *Nano Res.* **2016**, *9*, 1689–1700. [[CrossRef](#)]
289. Maeda, K.; Domen, K. Chapter 12 Nano-particulate photocatalysts for overall water splitting under visible light. In *Theoretical and Computational Chemistry*; Elsevier: Amsterdam, The Netherlands, 2007; Volume 18, pp. 301–315.
290. Nosaka, Y.; Komori, S.; Yawata, K.; Hirakawa, T.; Nosaka, A.Y. Photocatalytic •OH radical formation in TiO₂ aqueous suspension studied by several detection methods. *Phys. Chem. Chem. Phys.* **2003**, *5*, 4731–4735. [[CrossRef](#)]
291. Zhou, W.; Fu, H. Defect-mediated electron-hole separation in semiconductor photocatalysis. *Inorg. Chem. Front.* **2018**, *5*, 1240–1254. [[CrossRef](#)]
292. Yan, Y.; Yin, W.J.; Wu, Y.; Shi, T.; Paudel, N.R.; Li, C.; Poplawsky, J.; Wang, Z.; Moseley, J.; Guthrey, H.; et al. Physics of grain boundaries in polycrystalline photovoltaic semiconductors. *J. Appl. Phys.* **2015**, *117*, 112807. [[CrossRef](#)]
293. Liang, H.; Cui, S.; Su, R.; Guan, P.; He, Y.; Yang, L.; Chen, L.; Zhang, Y.; Mei, Z.; Du, X. Flexible X-Ray Detectors Based on Amorphous Ga₂O₃ Thin Films. *ACS Photonics* **2019**, *6*, 351–359. [[CrossRef](#)]
294. Sasaki, K.; Higashiwaki, M.; Kuramata, A.; Masui, T.; Yamakoshi, S. Si-Ion Implantation Doping in β -Ga₂O₃ and Its Application to Fabrication of Low-Resistance Ohmic Contacts. *Appl. Phys. Express* **2013**, *6*, 2–6. [[CrossRef](#)]
295. Fleischer, M.; Meixner, H. Oxygen Sensing with Long-Term Stable Ga₂O₃ Thin Films. *Sens. Actuators B Chem.* **1991**, *5*, 115–119. [[CrossRef](#)]